Intrinsic transverse momentum and parton correlations from dynamical chiral symmetry breaking

P. Schweitzer, M. Strikman, and C. Weiss³

¹Department of Physics, University of Connecticut, Storrs, CT 06269, USA
²Department of Physics, Pennsylvania State University, University Park, PA 16802, USA
³Theory Center, Jefferson Lab, Newport News, VA 23606, USA

The dynamical breaking of chiral symmetry in QCD is caused by nonperturbative interactions on a distance scale $\rho \sim 0.3\,\mathrm{fm}$, much smaller than the typical hadronic size $R \sim 1\,\mathrm{fm}$. These shortdistance interactions influence the intrinsic transverse momentum distributions of partons and their correlations at a low normalization point. We study this phenomenon in an effective description of the low-energy dynamics in terms of chiral constituent quark degrees of freedom, which refers to the large- N_c limit of QCD. The nucleon is obtained as a system of constituent quarks and antiquarks moving in a self-consistent classical chiral field (relativistic mean-field approximation, or chiral quark-soliton model). The calculated transverse momentum distributions of constituent quarks and antiquarks are matched with QCD quarks, antiquarks and gluons at the chiral symmetry-breaking scale ρ^{-2} . We find that the transverse momentum distribution of valence quarks is localized at $p_T^2 \sim$ R^{-2} and roughly of Gaussian shape. The distribution of unpolarized sea quarks exhibits a wouldbe power-like tail $\sim 1/p_T^2$ extending up to the chiral symmetry-breaking scale. Similar behavior is observed in the flavor-nonsinglet polarized sea. The high-momentum tails are the result of shortrange correlations between sea quarks in the nucleon's light-cone wave function, which are analogous to short-range NN correlations in nuclei. We show that the nucleon's light-cone wave function contains correlated pairs of transverse size $\rho \ll R$ with scalar-isoscalar (Σ) and pseudoscalarisovector (Π) quantum numbers, whose internal wave functions have a distinctive spin structure and become identical at $p_T^2 \sim \rho^{-2}$ (restoration of chiral symmetry). These features are model independent and represent an effect of dynamical chiral symmetry breaking on the nucleon's partonic structure. Our results have numerous implications for the transverse momentum distributions of particles produced in hard scattering processes. Under certain conditions the nonperturbative parton correlations predicted here could be observed in particle correlations between the current and target fragmentation regions of deep-inelastic scattering.

PACS numbers: 11.15.Pg 12.38.Lg 12.39.Fe 13.60.Hb 13.87.-a 13.88.+e Keywords: Parton distributions, transverse momentum, chiral symmetry breaking, QCD vacuum structure, short–range correlations, semi–inclusive scattering, multiparton processes

CONTENTS D. Structure of quark-antiquark pair 20 E. Power-like tail at large momenta 21 F. Implementation of ultraviolet cutoff 22 2 I. Introduction G. Quark field correlator in coordinate space 24 H. Numerical evaluation 26 II. Effective dynamics and nucleon structure 6 27 I. Sea vs. valence quark distribution A. Chiral constituent quarks 6 27 J. Polarized sea quark distribution B. Nucleon as chiral soliton 7 29 VI. Short–range correlations of partons III. Intrinsic transverse momentum distributions 8 A. Nucleon wave function at large momenta 29 8 A. Definition and parametric domain B. Spin structure of pair correlations 32 9 B. Evaluation in single-particle states C. Restoration of chiral symmetry 32 12 C. Rest frame interpretation 32 D. Momentum distribution from pairs D. Positivity and inequalities 13 E. Coordinate-space correlation function 13 VII. Summary and discussion 34 A. Summary of model results 34 IV. Valence quark transverse momentum 14 B. Matching with QCD 36 14 A. Transverse momentum distribution C. Toward parton correlations in QCD 37 15 B. Average transverse momentum C. Polarized distribution 16 VIII. Applications to deep-inelastic processes 39 A. Perturbative QCD radiation 39 V. Sea quark transverse momentum 16 B. Semi-inclusive measurements 39 A. Gradient expansion 16 C. Correlation measurements 41 B. Representation in light-cone variables 18 D. Multiparton processes 42 C. Momentum distribution of classical field 20 E. Exclusive meson production 42

Acknowledgments
A. Parametrization of soliton profile
B. Bound–state level wave function

C. Fourier transform of soliton field

References 44

42

42

43

44

I. INTRODUCTION

The parton model provides the basic script for expressing hadron structure as seen by short–distance probes such as local current operators or high–momentum transfer processes. Its fundamental assumption is that the fast–moving hadron can be regarded as a collection of pointlike constituents that behave like free particles on the timescale of their interaction with the external probe. The basic quantities are the number densities of partons as functions of their longitudinal momentum fraction x. Matrix elements of local current operators measure integrals of the parton densities ("sum rules"), while processes such as deep–inelastic eN scattering (or DIS) or production of high–mass systems in NN scattering probe them differentially in x.

The parton model can be thought of as the limiting case of a large class of dynamical models of hadron structure, in which the typical transverse momenta do not grow (or at most logarithmically) as the longitudinal momentum of the hadron is increased. In this approach the parton densities appear as integrals over the transverse momenta of the constituents [1],

$$f_1(x|\mu^2) = \int_{\mu^2} d^2p_T f_1(x, p_T),$$
 (1.1)

where μ^2 signifies a cutoff (e.g. in the parton virtuality, or in the invariant mass of configurations in the lightfront wave functions), which restricts the integral over p_T and defines the resolution scale at which the picture of pointlike partons is supposed to apply. The integrand in Eq. (1.1) is referred to as the "intrinsic" transverse momentum distribution of the partons. It is tempting to interpret this function as a density of particles and use it to study the internal motion of the constituents in the system. While this is principally possible, studies of field-theoretical models show that the transverse motion can generally not be separated from the interactions in the system. In gauge theories such as QED and QCD the parton picture requires the light-cone gauge, where the transverse components of the gauge potential, A_T , represent dynamical degrees of freedom. Gauge invariance implies that the transverse derivatives of the fermion fields appear in the combination $\nabla_T \equiv \partial_T - i \mathbf{A}_T$, linking the kinetic transverse momentum of the fermions to dynamical gauge fields in the hadron [2]. The interpretation of the intrinsic transverse momentum distributions is thus

generally much more subtle than that of the parton number densities.

A partonic picture of hadron structure is expected to emerge from QCD as the result of long-range nonperturbative interactions, and is commonly used to describe the boundary conditions for perturbative QCD calculations of hard processes. In this approach the parton densities can be expressed as matrix elements of certain quark and gluon light-ray operators of twist 2, i.e., correlation functions of the fields at light-like separation, normalized at the scale μ^2 (normalization point) [3]. The dependence on the scale can be calculated perturbatively for sufficiently large values; it is governed by the renormalization group equations for the composite operators, which coincide with the Dokshitzer-Gribov-Lipatov-Altarelli-Parisi (or DGLAP) evolution equations describing parton decay in the leading logarithmic approximation. In the region where perturbative evolution is applicable the intrinsic p_T distribution of partons is well-defined and of the form

$$f_1(x, p_T) \sim \frac{C_{f_1}(x)}{p_T^2},$$
 (1.2)

which reflects the ultraviolet (or UV) divergences of QCD and implies a logarithmic dependence of the parton density Eq. (1.1) on the scale μ^2 . Conversely, the coefficient $C_{f_1}(x)$ can be recovered as the logarithmic derivative of the parton density with respect to the scale,

$$C_{f_1}(x) = \pi^{-1} \mu^2 \frac{d}{d\mu^2} f_1(x|\mu^2).$$
 (1.3)

"Unintegrated" parton densities defined according to Eqs. (1.2) and (1.3) have been employed in phenomenological studies of DIS at small $x (\lesssim 10^{-2})$ [4]. A more careful treatment accounts also for the loss of partons in the course of DGLAP evolution as described by the Sudakov survival factor, which becomes more important at larger values of x [5, 6].

The extension of the concept of parton transverse momentum in QCD into the nonperturbative domain is inherently not unique, and different prescriptions have been proposed in the context of studies of various classes of high-momentum transfer processes. The calculation of power corrections to unpolarized DIS structure functions in the collinear expansion leads to twist-4 light-ray operators of the form $\bar{\psi}\nabla_{T,i}\dots\nabla_{T,j}\psi$, which can be interpreted as measuring the "average transverse momentum" of the quarks (keeping in mind that it cannot be separated from the transverse gauge fields) [2, 7]. Similar operators of twist 3 appear in the study of singlespin asymmetries in high- p_T particle production [8]. An alternative prescription are the transverse-momentumdependent distributions (or TMDs) introduced in the context of a QCD description of semi-inclusive DIS at low transverse momenta [9–11]. They are defined as correlation functions of fields off the light-cone, at finite transverse separations, and involve gauge links (or phase

factors) describing the effect of QCD initial/final–state interactions of the quark participating in the hard process. The renormalization properties of these operators and the proper choice of gauge links are presently the subject of intense theoretical study [12–14]. The formal correspondence between the "collinear" and "TMD" definitions of parton transverse momentum in the perturbative region of high p_T was studied in Ref. [15]. A natural concept of "intrinsic" transverse momentum also appears in approaches which describe hadron structure in terms of light–cone wave functions at a low scale [16, 17].

The effective dynamics of strong interactions at the hadronic scale is in large measure governed by the spontaneous breaking of chiral symmetry in the QCD vacuum. It leads to the appearance of a chiral condensate $\langle \bar{\psi}\psi \rangle \neq 0$ (order parameter), whose phase fluctuations give rise to almost massless excitations (Goldstone bosons), the pions. Their interactions are summarized by the universal chiral Lagrangian and determine the behavior of strong interactions over distances of the order $\sim 1/m_{\pi}$, which can be studied using methods of effective field theory. However, the influence of chiral symmetry breaking extends down to much shorter distances, defined by the range of the nonperturbative QCD interactions that lead to the appearance of the chiral condensate. Lattice QCD calculations and numerous phenomenological observations suggest that the size of the nonperturbative field configurations causing the spontaneous breaking of chiral symmetry in QCD is much smaller than the typical hadronic radius $R \sim 1 \, \text{fm}$. An objective gauge-invariant measure of this scale is the average quark virtuality in the chiral condensate [18]

$$\frac{m_0^2}{2} \equiv \frac{\langle \bar{\psi} \nabla^2 \psi \rangle}{\langle \bar{\psi} \psi \rangle}. \tag{1.4}$$

Lattice simulations give $m_0^2/2 \gtrsim 0.5\,\mathrm{GeV}^2$ at a normalization point of $\mu \sim 1\,\mathrm{GeV}$ [19, 20]; even larger values were obtained in Ref. [21]. This is supported by the results of direct studies of chirality–flipping topologically charged vacuum fluctuations in lattice simulations [22]; see Refs. [23, 24] for a review. The same conclusion is obtained from the instanton model of the QCD vacuum [25, 26] (see Refs. [24, 27] for a review), where the typical size of the instantons is $\rho \sim 0.3\,\mathrm{fm}$ and the average quark virtuality in the chiral condensate is found to be $m_0^2/2 = 2\,\rho^{-2} \approx 0.7\,\mathrm{GeV}^2$ [28]. Abstracting from these findings, one may state that the spontaneous breaking of chiral symmetry in QCD is characterized by a dynamical scale much shorter than the typical hadronic radius,

$$\rho \sim 0.3 \,\text{fm} \ll R \sim 1 \,\text{fm}.$$
 (1.5)

The existence of this nonperturbative short-distance scale has far-reaching consequences for the structure of hadrons and their low-energy interactions [24, 27].

Here we want to ask what dynamical chiral symmetry breaking and the existence of the short–distance scale ρ imply for the transverse momentum distribution of

partons in the nucleon at a low normalization point. This question is clearly of great importance for both the general theoretical understanding of partonic structure and the phenomenology of hard processes with identified particles, such as semi-inclusive ep scattering, jets and Drell-Yan pair production in pp scattering, and multiparton interactions in pp collisions. In view of the ambiguities in the very definition of intrinsic transverse momentum in QCD we shall not attempt to approach this problem in a model-independent manner, as the evaluation of certain a priori defined QCD operators in the nucleon state. Instead, we shall study the transverse momentum distributions of partons in a model of the effective lowenergy dynamics resulting from the spontaneous breaking of chiral symmetry, which implements the two dynamical scales of Eq. (1.5). The dynamical model will suggest a natural definition of the intrinsic transverse momentum distribution in terms of effective degrees of freedom, including the pertinent resolution scale. The matching of the model p_T distributions with QCD will then be considered on the basis of their specific form, and with the help of empirical information on the p_T -integrated parton densities, at a normalization point determined by the chiral symmetry-breaking scale, $\mu^2 \sim \rho^{-2}$. In the present state of development such an approach is fully justified and provides a useful complement to more abstract studies of transverse momentum distributions based on specific QCD operator definitions.

Numerous observations point to the importance of constituent quarks and pions as effective degrees of freedom below the chiral symmetry-breaking scale. Theoretical arguments suggest that in the large- N_c limit of QCD the effective dynamics resulting from the spontaneous breaking of chiral symmetry can be approximated by a field-theoretical model based on chiral constituent quarks [24, 29]. It expresses the fact that the modes of the QCD quark fields with virtualities below the chiralsymmetry breaking scale ρ^{-2} acquire a dynamical mass. Because of chiral invariance, this is necessarily accompanied by a coupling to the Goldstone pion field, which in the large- N_c limit is itself a composite of constituent quarks and antiquarks. This effective dynamics is relevant up to the chiral symmetry-breaking scale, which appears as the UV cutoff of the model. A crucial point is that the chiral symmetry-breaking scale is assumed to be parametrically large compared to the dynamical quark mass, such that the massive constituent quarks can be regarded as pointlike over a wide range of virtualities. This two-scale picture gives a precise meaning to the notion of constituent quarks as effective degrees of freedom and provides an ordering principle for the calculation of hadron structure.

In the effective chiral model the nucleon is obtained as an extended solution in which massive quarks and antiquarks move in the background of a self-consistent pion field (relativistic mean-field approximation, or chiral quark-soliton model) [30]. Matrix elements of operators between nucleon states can be computed in a sys-

tematic $1/N_c$ expansion. This picture results in an essentially parameter-free description of the static nucleon observables and form factors [31]. Because the description is fully field-theoretical, the model has a partonic limit and can be used to calculate the nucleon's parton densities at a low normalization point [32, 33]. It provides for a nontrivial antiquark content of the nucleon at the starting scale of DGLAP evolution, in agreement with the results of global QCD fits of DIS data; see Ref. [34] for a recent update. In particular, it quantitatively reproduces the flavor asymmetry of the unpolarized sea quarks, $f_1^{\bar{u}}(x) - f_1^{\bar{d}}(x) < 0$, observed in DIS [35] and Drell-Yan pair production [36]. It predicts a large flavor asymmetry also in the polarized sea, $g_1^{\bar{u}}(x) - g_1^d(x) > 0$; there are hints of an asymmetry of this sign in a recent global QCD fit including semi-inclusive data [37]; further clarification is expected from W^{\pm} production in polarized pp collisions [38, 39]. These nonsinglet sea quark distributions do not mix with gluons under DGLAP evolution and represent clear signals of the nonperturbative QCD vacuum structure encoded in the model.

The matching of the model parton distributions with QCD quark and gluon densities is performed at the chiral symmetry-breaking scale, $\mu^2 \sim \rho^{-2}$, which represents the UV cutoff of the effective dynamics of constituent quarks. Thanks to the field-theoretical formulation of the dynamics (completeness of states, local interactions) and the relativistic covariance of the mean-field approximation the chiral quark-soliton model conserves the overall light-cone momentum, so that the constituent quarks and antiquarks carry the entire light-cone momentum of the nucleon. This provides a solid basis for matching the effective degrees of freedom with the quarks and gluons of QCD. Physically, the effective degrees of freedom are composites of the QCD quark and gluon fields, and the model parton distributions should be "resolved" into their QCD content at the scale $\mu^2 \sim \rho^{-2}$. This process is not governed by intrinsic properties of the effective chiral dynamics but requires detailed knowledge of its embedding in QCD, which is poorly understood at present. In the simplest approximation one assumes that the constituent quarks and antiquarks remain pointlike up to the chiral symmetry-breaking scale and matches them with the quarks and antiquarks of QCD; the gluon density is zero in this approximation [32]. This approximation was adopted in most calculations of partonic structure in the chiral quark-soliton model so far. Its accuracy may be judged from the fact that in leading–order fits to the DIS data [34] at $\mu_{\rm LO}^2 \approx 0.3\,{\rm GeV}^2$ about 30% of the nucleon's momentum is carried by gluons. This shows that the resolution effect is moderately strong in the singlet sector; a substantially weaker effect is expected for nonsinglets. More accurate matching would be possible either with a microscopic derivation of the effective chiral dynamics from QCD (such as the instanton vacuum model [24]) or with detailed phenomenological modeling based on empirical parton densities.

In this article we explore the role of dynamical chi-

ral symmetry breaking in the intrinsic transverse momentum distribution of partons, using the chiral quarksoliton model as an effective description of the dynamics below the chiral symmetry-breaking scale. Our study is comprehensive and aims to address all relevant aspects of the problem: the definition of the p_T distributions within the effective model, their practical evaluation and numerical study, the implementation of the UV cutoff and the matching with QCD, and the implications for DIS experiments. We show that the effective dynamics suggests a natural definition of the intrinsic transverse momentum distributions, as the momentum densities of massive quarks and antiquarks in the fast-moving nucleon. We calculate the transverse momentum distribution of valence and sea quarks in the model in leading order of the $1/N_c$ expansion and study their properties. Our investigation leads to several interesting new insights.

First, we find that valence and sea quarks have very different intrinsic transverse momentum distributions. The distribution of valence quarks (quarks minus antiquarks) has a range of the order of the inverse nucleon size, $p_T^2 \sim R^{-2}$ and an approximately Gaussian shape. The distribution of sea quarks (antiquarks), in contrast, exhibits a power-like tail $\propto p_T^{-2}$ that extends up to the chiral-symmetry breaking scale. Its coefficient is determined by low-energy chiral dynamics and quasi modelindependent. Such behavior is found in the flavor-singlet unpolarized sea quark distribution, where it was first observed in the numerical study of Ref. [40], and the flavornonsinglet polarized sea quark distribution, which are the leading combinations in the $1/N_c$ expansion. The qualitative difference between valence and sea quark transverse momenta represents the imprint of dynamical chiral symmetry breaking on the nucleon's partonic structure and has numerous potential implications for hard scattering processes.

Second, we show that, under rather general conditions, the sea quark transverse momentum distributions do not depend on the details of the UV cutoff of the effective chiral model. While the chiral symmetry-breaking scale represents the generic UV cutoff of the effective chiral dynamics, the manner in which it is implemented in the model is not dictated by chiral symmetry but must be constrained by other physical considerations. Imposing minimal physical conditions on the regularization scheme (charge conservation, longitudinal momentum conservation, analyticity) we find that the sea quark transverse momentum distributions are independent of the regularization scheme up to momenta $p_T^2\sim 1\,{\rm GeV}^2$ and represent stable predictions of the model. Since the regularization conserves the overall light-cone momentum. the constituent quark and antiquark distributions in the model carry the entire light-cone momentum of the nucleon and can consistently be matched with QCD quarks and gluons at the scale $\mu^2 \sim \rho^{-2}$.

Third, we explore the role of dynamical chiral symmetry breaking at a more microscopic level, in terms of the light—cone wave function of the nucleon in the chiral

quark-soliton model [41-43]. The large- N_c limit allows us to discuss the nucleon's partonic structure in terms of the traditional nuclear physics concepts of the mean field and short-range correlations. We show that the sea quarks in the nucleon's light-cone wave functions can exist in correlated pairs with a transverse size of the order of the chiral-symmetry-breaking scale ρ , much smaller than the nucleon size R, which reflects their origin from dynamical chiral symmetry breaking. The pairs come in scalar–isoscalar (Σ) and pseudoscalar–isovector (Π) quantum numbers and have a distinctive spin structure; at large transverse momenta $p_T^2 \sim \rho^{-2}$ their internal wave functions become identical, reflecting the "restoration of chiral symmetry" at the cutoff scale. These short-range correlations represent another imprint of chiral symmetry breaking on the nucleon's partonic structure. They provide a natural microscopic explanation of the high p_T tails found in the sea quark transverse momentum distributions and point to an interesting analogy with short-range NN correlations in nuclei; see Refs. [44–46] for a review. Most importantly, it may be possible to observe these nonperturbative parton correlations directly in measurements of particle correlations between the current and target fragmentation regions in deep-inelastic ep scattering or multiparton processes in pp scattering.

Quantifying the experimental implications of our results is a complex task, which for the most part we leave to a separate study. Additional information on QCD final-state interactions and the fragmentation process is needed to relate the intrinsic p_T distribution of partons to the observed transverse momentum distributions of hadrons emerging from hard scattering processes. Nevertheless, some simple conclusions can be drawn already at the present stage, without detailed modeling. Semiinclusive DIS with single identified hadrons is widely used to measure the flavor decomposition of the nucleon parton densities. We show that the usual procedure of combining π^+ and π^- multiplicities to isolate the valence quark density has to be modified if the intrinsic p_T distributions of quarks and antiquarks in the nucleon are not the same and the experiment does not cover the full transverse momentum range of the produced hadrons. A direct test of the nonperturbative parton short-range correlations predicted here could be performed through measurements of particle correlations between the current and target fragmentation regions in deep-inelastic ep scattering. We show that there is a kinematic window at moderate γ^*N center-of-mass energies $W^2 \sim \text{few} \times 10 \, \text{GeV}^2$ in which the two fragmenting partons could be cleanly separated while perturbative QCD radiation does not yet destroy the nonperturbative correlations. We also comment on the role of nonperturbative correlations in multiparton processes in highenergy pp scattering. Finally, the nonperturbative parton correlations predicted here may play an important role in exclusive meson production at energies of $W \sim \text{few GeV}$.

The plan of this paper is as follows. In Sec. II we summarize the model of the effective dynamics below the

chiral symmetry-breaking scale and the resulting meanfield description of the nucleon in the large- N_c limit. In Sec. III we present the definition of the transverse momentum distributions in the model as momentum densities of constituent quarks and antiquarks in the fastmoving nucleon and discuss their basic properties. We evaluate the expressions in terms of quark single-particle wave functions and develop their interpretation in the nucleon rest frame. We also discuss the coordinatespace correlation function associated with the transverse momentum distribution in our model, and the positivity conditions and inequalities for the polarized distributions. In Sec. IV we study the transverse momentum distributions of valence quarks (quarks minus antiquarks). We calculate the flavor-singlet unpolarized and flavor–nonsinglet polarized valence quark distributions, $f_1^{u+d-\bar{u}-\bar{d}}(x,p_T)$ and $g_1^{u-d-\bar{u}+\bar{d}}(x,p_T)$, which appear in leading order of the $1/N_c$ expansion, and study the average transverse momentum $\langle p_T^2 \rangle$.

In Sec. V we give an in-depth treatment of the sea quark transverse momentum distributions in our approach. We evaluate them using the gradient expansion of the quark Green function, an approximation which allows us to analytically study the behavior of the distributions at large transverse momenta. The gradient expansion is formulated in terms of light-cone variables, which allows for a simple physical interpretation in terms of quark-antiquark pair production by the classical chiral field of the nucleon. We analytically exhibit the power-like $1/p_T^2$ tail of the flavor-singlet sea quark distribution $f_1^{\bar{u}+\bar{d}}(x,p_T)$ and discuss its significance. We then describe the physical conditions on the UV cutoff and present two regularization schemes that meet them (Pauli-Villars subtraction, and an invariant-mass cutoff). We evaluate the distributions numerically and verify that they are independent of the form of the UV cutoff. We also compute the coordinate-space correlation function in the model; we show that at large distances it decays exponentially and is completely governed by low-energy dynamics. Finally, we also compare the sea quark with the valence quark distributions at the numerical level and confirm their qualitative difference. We also compute the flavor–nonsinglet polarized distribution $g_1^{\bar{u}-\bar{d}}(x,p_T)$ and show that it exhibits a similar power-like tail at large p_T as the flavor–singlet unpolarized one.

In Sec. VI we discuss the nucleon's light—cone wave function at large transverse momenta. We show that it is dominated by configurations in which a single quark—antiquark pair has momenta of the order of the chiral symmetry—breaking scale. We compute the internal wave functions of Σ — and Π —type pairs, study their spin structure, and demonstrate that chiral symmetry is effectively restored at large p_T . We then prove that the high— p_T tails in the distribution of sea quarks, found previously by gradient expansion of the one—body densities, is exactly reproduced by the momentum density (wave function overlap) of such correlated pairs. In Sec. VII we summarize the model results for transverse momentum

distributions and correlations and list problems meriting further study. We discuss the matching of the model distributions with QCD using information about empirical p_T -integrated parton densities at a low scale, and discuss pertinent open questions. Lastly, we develop a qualitative physical picture how nonperturbative parton correlations emerge from QCD and discuss its implications. In Sec. VIII we outline the implications of our results for hard scattering processes. We discuss the consequences of different p_T distributions of valence and sea quarks for quark flavor separation in semi-inclusive DIS. We also investigate the possibility of probing parton correlations by measurements of particle correlations between the current and target fragmentation region. Lastly, we comment on the potential role of nonperturbative parton correlations in multiparton processes in pp collisions and exclusive meson production in ep scattering.

A numerical study of transverse momentum–dependent quark distributions in the chiral quark–soliton model was reported in Ref. [40] and found a larger average p_T of sea compared to valence quarks. Here we reproduce and explain this surprising result using analytic approximations, and show that the presence of a power–like tail of the p_T distribution follows directly from the short–range nature of dynamical chiral symmetry breaking in QCD as encoded in the effective model. We also extend our study to the quark helicity distribution, where the tail appears in the flavor nonsinglet sector and is less affected by perturbative QCD radiation in hard processes.

Transverse momentum distributions of quarks were extensively studied in diquark spectator models of the nucleon [47], the bag model [48, 49], light-front quark models [50], and a covariant parton model [51]. While incorporating some aspects of relativistic kinematics, all of these models describe the nucleon as system with a fixed number of particles, ignoring the essential manybody nature of the parton picture. Our approach here is field-theoretical and describes the nucleon as a superposition of configurations with different numbers of particles, which allows us to uncover the effect of the QCD vacuum on the nucleon's partonic structure. Also, with the underlying two dynamical scales, cf. Eq. (1.5), our approach provides a parametric framework for defining the transverse momentum distributions at a low scale in terms of effective degrees of freedom, which effectively include also the original gauge fields of QCD.

II. EFFECTIVE DYNAMICS AND NUCLEON STRUCTURE

A. Chiral constituent quarks

We begin by summarizing the essential elements of the two–scale model of low–energy dynamics and the resulting description of the nucleon as a chiral soliton, following the lines of Refs. [30, 32, 33]. The effective dynamics resulting from the spontaneous breaking of chiral sym-

metry can be approximated as a field theory of massive quarks coupled to a Goldstone boson (pion) field in a chirally invariant manner. It is described by the Lagrangian density

$$L_{\text{eff}} \equiv \bar{\psi}(x)[i\hat{\partial} - M U^{\gamma_5}(x)]\psi(x), \qquad (2.1)$$

where $\psi(x)$ is the quark field (the sum over light quark flavors u and d is implied),

$$\hat{\partial} \equiv \gamma^{\alpha} \partial_{\alpha}, \tag{2.2}$$

and M is the dynamical quark mass. The pion field is contained in the variable

$$U^{\gamma_5}(x) \equiv \exp[i\gamma_5 \tau^a \pi^a(x)/F_{\pi}]$$

= $\frac{1}{2}(1+\gamma_5)U(x) + \frac{1}{2}(1-\gamma_5)U^{\dagger}(x)$, (2.3)

where

$$U(x) \equiv \exp[i\tau^a \pi^a(x)/F_{\pi}] \tag{2.4}$$

is the usual unitary matrix field. Here $\tau^a(a=1,2,3)$ denote the isospin Pauli matrices, and $F_\pi=93\,\mathrm{MeV}$ is the pion decay constant. Typical values of the dynamical quark mass obtained from phenomenological considerations are $M\sim0.35$ –0.4 GeV. In conventional terms, the strength of the pion–quark coupling is given by $M/F_\pi\approx4$, as can be seen be expanding the exponential in Eq. (2.4) in powers of the pion field. The effective theory defined by Eq. (2.1) is thus strongly coupled and has to be solved using nonperturbative methods based on the $1/N_c$ expansion (semiclassical or saddle–point approximation) [52].

The effective dynamics described by Eq. (2.1) applies to quarks with virtualities below the chiral–symmetry–breaking scale, which acts as an UV cutoff for the model. In practical calculations the cutoff is implemented by applying a regularization scheme, and the actual value of the cutoff parameter depends on the scheme. In the following we denote the generic cutoff parameter by Λ^2 (not to be confused with the QCD scale parameter $\Lambda^2_{\rm QCD}$). A crucial point is that the dynamical quark mass is assumed to be parametrically small compared to the cutoff,

$$M^2 \ll \Lambda^2, \tag{2.5}$$

implying that the effective model is applicable in a parametrically wide range of quark momenta where the massive quarks behave approximately as pointlike particles. While the numerical accuracy of this approximation is limited $(M^2/\Lambda^2 \sim 0.3)$ with a typical virtuality cutoff; see below), it serves as an ordering principle for the calculation of physical quantities and provides a clear mathematical justification for the constituent quark picture. The choice of regularization scheme for implementing the UV cutoff involves physical judgment and is usually motivated by the desire to preserve fundamental properties such as analyticity or current conservation. For the p_T -integrated parton densities this question was studied in

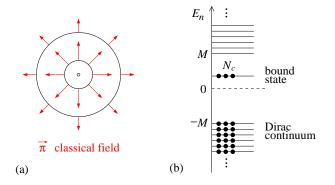


FIG. 1. (Color online) Chiral quark—soliton model of the nucleon. (a) Classical chiral field in the nucleon rest frame. The isospin direction at a given point is defined by the radius vector ("hedgehog"). (b) Spectrum of quark single—particle levels in the classical chiral field, Eq. (2.7). It includes a discrete bound—state level and the distorted negative and positive—energy Dirac continua. In the nucleon state (baryon number +1) the bound—state and negative—energy continuum levels are occupied by N_c quarks each.

Refs. [32, 33]; for the transverse momentum distributions of interest here it will be discussed in detail in Sec. VF below.

The effective model Eq. (2.1) can be motivated by general considerations about constituent quarks as effective degrees of freedom, see Ref. [24] for a review. In particular, when integrating over the quark fields and expanding the fermion determinant in gradients of the pion field, one obtains the chiral Lagrangian of the pion field, with definite predictions for the coupling constants in terms of the two parameters, M and Λ . In this sense, the effective theory "interpolates" between the chiral Lagrangian and a theory of free quarks at large virtualities. Eq. (2.1) has also been derived from the instanton model of the QCD vacuum, by large- N_c bosonization of the instanton-induced 'tHooft interaction between quarks in the chirally broken phase [53, 54]. In this context the UV cutoff is given by the inverse average instanton size in the vacuum, $\rho^{-2} \approx 0.4 \,\mathrm{GeV^2}$, and restricts the quarks' Euclidean momenta (or virtualities); the dynamical quark mass is obtained at $M \approx 0.35 \,\text{GeV}$. The parametric smallness of the quark mass compared to the cutoff, Eq. (2.5), follows directly from the "diluteness" of the instanton medium describing the QCD vacuum.

B. Nucleon as chiral soliton

The effective dynamics described by Eq. (2.1) refers to the large- N_c limit of QCD, and information on hadron structure is extracted by calculating hadronic correlation functions in a systematic $1/N_c$ expansion. The nucleon is obtained as an extended system in which quarks move in the background of a self-consistent classical chiral field (relativistic mean-field approximation, or chiral quark-

soliton model) [30]. In the nucleon rest frame the chiral field is of "hedgehog" form (see Fig. 1a),

$$U_{\rm cl}(\boldsymbol{x}) = \exp\left[\frac{i\tau^a x^a}{r}P(r)\right], \qquad (r \equiv |\boldsymbol{x}|), \qquad (2.6)$$

and the profile function P(r) satisfies $P(0) = -\pi$ and $P(r) \to 0$ for $r \to \infty$ [55]. The quarks move in single-particle orbits, whose wave functions are the eigenfunctions of the Dirac Hamiltonian in the background chiral field, i.e., the solutions of the Dirac equation

$$\left(-i\gamma^{0}\gamma^{i}\partial_{i} + M\gamma^{0}U_{\text{cl}}^{\gamma_{5}}\right)\Phi_{n}(\boldsymbol{x}) = E_{n}\Phi_{n}(\boldsymbol{x}). \quad (2.7)$$

The energy spectrum includes a discrete bound–state level and the positive and negative Dirac continua, distorted by the chiral field (see Fig. 1b). Each level is occupied with N_c quarks. The static energy of the system is the sum of energies of the discrete level and the energy stored in the negative–energy continuum,

$$E[U_{\rm cl}] = N_c E_{\rm lev} + N_c \sum_{E_n < 0} (E_n - E_n^{(0)}),$$
 (2.8)

where $E_n^{(0)}$ denote the energy levels of the vacuum Hamiltonian with $U_{\rm cl}=1$. The profile function P(r) is determined by minimizing the static energy Eq. (2.8). In Appendix A we show the profile obtained by numerical minimization [56] with a Pauli–Villars cutoff of the Dirac sea contribution to the energy (described in Sec. V) and give a simple analytic parametrization for use in our numerical estimates below. The nucleon mass, which is $O(N_c)$ within the $1/N_c$ expansion, is in leading order given by the minimum value of the classical energy,

$$M_N = E[U_{\rm cl}]_{\rm min} + O(N_C^0).$$
 (2.9)

Finally, nucleon states of definite spin/isospin and linear momentum are constructed by quantizing the (iso–) rotational and translational zero modes of the soliton, see Ref. [30] for details. This leads to the appearance of the N and Δ as rotational states of the soliton and explains their mass splitting, $M_{\Delta}-M_{N}=O(1/N_{c})$, as the difference of the rotational energies.

The description of the nucleon obtained in this approach is fully field—theoretical and does not involve any ingredients "extraneous" to the dynamics encoded in Eq. (2.1). No further approximations besides the $1/N_c$ expansion are made in solving the dynamical problem. The description is also fully relativistic; it appears noncovariant only because the nucleon in the large— N_c limit is heavy, but relativistic corrections appear systematically as part of the $1/N_c$ expansion.

Matrix elements of quark one—body operators between nucleon states can be calculated in a systematic $1/N_c$ expansion and are generally expressed as sums of matrix elements between quark single—particle states in the classical chiral field; see Ref. [31] for a review. The projection on nucleon spin/isospin and momentum states is done by

integrating over the rotational/isorotational and translational zero modes of the classical field with appropriate collective wave functions. The sums over single—particle states can then be evaluated numerically by constructing the eigenfunctions and eigenvalues (both of the discrete bound—state level and the continuous spectrum) through numerical diagonalization of the Hamiltonian of Eq. (2.7) in a spherical box of finite size [57].

Alternatively, one may express matrix elements of quark one—body operators through the quark Green function in the chiral background field, using the formalism of second quantization. In an arbitrary (generally time—dependent) classical chiral field, the Feynman Green function is defined as the solution of the inhomogeneous Dirac equation with a delta function source.

$$[i\hat{\partial} - M U^{\gamma_5}(x)]G_F(x,y) = \delta^{(4)}(x-y),$$
 (2.10)

with causal boundary conditions, corresponding to the advanced solution for $x^0 < y^0$ and the retarded one for $x^0 > y^0$. In second quantization this function coincides with the expectation value of the time–ordered product of quantized field operators,

$$iG_F(x,y) = \langle N | T \psi(x) \bar{\psi}(y) | N \rangle,$$
 (2.11)

where $|N\rangle$ denotes the ground state of the fermionic system in the background of the (generally time–dependent) classical chiral field, with the occupation of the single–particle levels as indicated in Fig. 1b. In the static chiral field in the nucleon rest frame, Eq. (2.6), the time–ordered product becomes

$$iG_F(x,y)$$

$$= \Theta(x^0 - y^0) \sum_{n \text{ non-occ}} e^{-iE_n(x^0 - y^0)} \Phi_n(\boldsymbol{x}) \Phi_n^{\dagger}(\boldsymbol{y}) \gamma^0$$

$$- \Theta(y^0 - x^0) \sum_{n \text{ occ}} e^{-iE_n(x^0 - y^0)} \Phi_n(\boldsymbol{x}) \Phi_n^{\dagger}(\boldsymbol{y}) \gamma^0 \quad (2.12)$$

$$= \int_{-\infty}^{\infty} \frac{d\omega}{2\pi} e^{-i\omega(x^0 - y^0)} \sum_{n} \frac{\Phi_n(\boldsymbol{x})\Phi_n^{\dagger}(\boldsymbol{y})\gamma^0}{\omega - E_n + i0\sigma_n}, \qquad (2.13)$$

$$\sigma_n \equiv \begin{cases} -1 & \text{occupied levels,} \\ +1 & \text{non-occupied levels.} \end{cases}$$
 (2.14)

Equations (2.13) and (2.13) can be used to convert traces of the Green function into sums over single–particle levels and vice versa. There are many practical advantages of working with the Green function [32, 33]. It has simple transformation properties under Lorentz boosts, which follow directly from Eq. (2.10) (see Sec. III). Its analytic properties in energy allow one to derive sum rules and interchange sums over occupied and non–occupied states. Finally, the Green function can be evaluated approximately by expanding it in derivatives of the classical chiral field (gradient expansion). In this way one can obtain analytic expressions for the leading dependence of nucleon matrix elements in the limit of large UV cutoff, $\Lambda \to \infty$, or other limiting cases, such as the parton distributions at large transverse momenta (see Sec. V).

III. INTRINSIC TRANSVERSE MOMENTUM DISTRIBUTIONS

A. Definition and parametric domain

The basic framework for calculating parton densities in the chiral quark–soliton model of the nucleon was developed in Refs. [32, 33]. Generally, in the large– N_c limit one is interested in the parton densities at momentum fractions of the order

$$x = O(N_c^{-1}), (3.1)$$

corresponding to average (non–exceptional) configurations in the wave function of the fast–moving system [32]. The parton densities can be calculated starting from their parton model definition as number densities of particles in a nucleon moving with momentum $P \to \infty$ [33], or from their representation as matrix elements of quark light–ray operators in the nucleon rest frame [32]. The equivalence of the two formulations was demonstrated in Ref. [33] and is due to the relativistic and field–theoretical character of this description of the nucleon.

The relativistic mean—field picture of the nucleon implies a natural definition of the intrinsic transverse momentum distribution of partons at a low scale. Extending the approach of Ref. [33], we define the intrinsic transverse momentum distribution of partons in this model as the p_T —dependent number densities of quarks and antiquarks in the fast—moving nucleon state:

$$f_1^a(x, p_T) \equiv \frac{P}{(2\pi)^3} \langle N_v | \sum_{\sigma} a_{a\sigma}^{\dagger}(\boldsymbol{p}) a_{a\sigma}(\boldsymbol{p}) | N_v \rangle, \quad (3.2)$$

$$f_1^{\bar{a}}(x, p_T) \equiv \frac{P}{(2\pi)^3} \langle N_v | \sum_{\sigma} b_{a\sigma}^{\dagger}(\mathbf{p}) b_{a\sigma}(\mathbf{p}) | N_v \rangle, \quad (3.3)$$

where $p_T \equiv |\boldsymbol{p}_T|$,

$$p \equiv (p_T, xP), \tag{3.4}$$

$$P = \frac{vM_N}{\sqrt{1 - v^2}},\tag{3.5}$$

and the limit

$$v \rightarrow 1 \tag{3.6}$$

is understood here and in the following. Here $a_{a\sigma}, a^{\dagger}_{a\sigma}$ and $b_{a\sigma}, b^{\dagger}_{a\sigma}$ are the quark and antiquark annihilation and creation operators corresponding to the massive quark fields of the effective model Eq. (2.1). They annihilate/create quarks in plane—wave states with three—momentum \boldsymbol{p} and energy $p^0 = \sqrt{|\boldsymbol{p}|^2 + M^2}$, with a = u,d denoting the quark flavor and σ the spin projection on the 3–axis. The notation $\langle N_v|\dots|N_v\rangle$ indicates the average in the ground state of the fast–moving many–body system, with $\langle N_v|N_v\rangle=1$. Equations (3.2) and (3.3) define the unpolarized distributions (summed over

quark/antiquark spin); the corresponding expressions for the longitudinally polarized distributions are

$$g_1^a(x, p_T) \equiv \frac{P}{(2\pi)^3} \langle N_v | \Delta_\sigma a_{a\sigma}^\dagger(\mathbf{p}) a_{a\sigma}(\mathbf{p}) | N_v \rangle, \quad (3.7)$$

$$g_1^{\bar{a}}(x, p_T) \equiv \frac{P}{(2\pi)^3} \langle N_v | \Delta_{\sigma} b_{a\sigma}^{\dagger}(\boldsymbol{p}) b_{a\sigma}(\boldsymbol{p}) | N_v \rangle, \quad (3.8)$$

where

$$\Delta_{\sigma} \equiv (\sigma = +1/2) - (\sigma = -1/2) \tag{3.9}$$

denotes the spin difference.

An obvious property of the transverse momentum distributions defined by Eqs. (3.2) and (3.3) is that their integral over p_T reproduce the quark/antiquark densities in the model,

$$\int d^2 p_T f_1^{a,\bar{a}}(x, p_T)_{\text{reg}} = f_1^{a,\bar{a}}(x), \qquad (3.10)$$

$$\int d^2 p_T \ g_1^{a,\bar{a}}(x,p_T)_{\text{reg}} = g_1^{a,\bar{a}}(x). \tag{3.11}$$

The integral over transverse momenta would be logarithmically divergent at large values and is rendered finite by the UV cutoff of the model. In our interpretation the cutoff is part of the definition of the transverse momentum distribution in the model, as indicated by the label "reg" in Eqs. (3.10) and (3.11), not as an operation applied only at the level of the p_T integral. This interpretation is more restrictive than the one developed in Ref. [32, 33], where only the integrated parton densities were regularized, and places stronger demands on the regularization scheme. A detailed discussion of the implementation of the UV cutoff is given in Sec. V F below.

In the sense of the $1/N_c$ expansion the transverse momentum we consider are of the order

$$p_T = O(N_c^0).$$
 (3.12)

The $1/N_c$ expansion of the transverse momentum distributions is completely analogous to that of the p_T -integrated distributions [32]. In the following we consider the p_T distributions of those spin–flavor combinations of parton densities which appear in leading order of the $1/N_c$ expansion, namely the flavor–singlet unpolarized distributions,

$$f_1^{u+d}(x, p_T), \quad f_1^{\bar{u}+\bar{d}}(x, p_T),$$
 (3.13)

and the flavor-nonsinglet polarized distributions,

$$g_1^{u-d}(x, p_T), \quad g_1^{\bar{u}-\bar{d}}(x, p_T).$$
 (3.14)

Equations (3.2)–(3.9) define the transverse momentum distributions of massive constituent quarks and antiquarks — effective degrees of freedom which are to be matched with QCD quarks, antiquarks and gluons at the chiral symmetry–breaking scale. The formulas should be

regarded as preliminary definitions, whose physical significance and UV regularization will be elaborated in the following. The UV cutoff affects the distribution of valence and sea quarks very differently and will be discussed separately for the two cases (Secs. IV and V). We shall see that under rather general conditions on the regularization scheme (charge conservation, longitudinal momentum conservation, analyticity) the transverse momentum distributions in the model are not sensitive to the details of the regularization scheme up to momenta $p_T^2 \sim 10 M^2$ and represent robust predictions of the model. This provides a firm basis for the matching of the model p_T distributions with QCD (Sec. VII). In the remainder of this section we discuss the formal properties of the distributions defined by Eqs. (3.2)–(3.9) without reference to the UV cutoff.

B. Evaluation in single-particle states

The evaluation of the model transverse momentum distributions defined by Eqs. (3.2) and (3.3) proceeds along the same lines as those of the p_T -integrated parton densities [33]. In the following we summarize the main steps, emphasizing those aspects that require attention in the case of transverse momentum dependence.

The one–body momentum density can conveniently be calculated in terms of the Feynman Green function of the system, using the formalism of second quantization. The quark field operator is defined as

$$\psi(x) = \int \frac{d^3p}{(2\pi)^3 \sqrt{2p^0}} \sum_{\sigma} \left[a_{\sigma}(\mathbf{p}) \ u(\mathbf{p}, \sigma) \ e^{-ipx} + b_{\sigma}^+(\mathbf{p}) \ v(\mathbf{p}, \sigma) \ e^{ipx} \right], \tag{3.15}$$

where $u(\boldsymbol{p},\sigma)$ and $v(\boldsymbol{p},\sigma)$ are the spinor wave function of the free quarks and antiquarks, normalized as $\bar{u}u=-\bar{v}v=2M$, with $\bar{u}\equiv u^\dagger\gamma^0$ and $\bar{v}\equiv v^\dagger\gamma^0$. The quark and antiquark number operators can be expressed as equaltime products of the field operators,

$$\int d^3x_1 \int d^3x_2 \ e^{-i\boldsymbol{p}(\boldsymbol{x}_1 - \boldsymbol{x}_2)} \ \bar{\psi}_j(\boldsymbol{x}_2, t) \ \psi_i(\boldsymbol{x}_1, t)$$

$$= \sum_{\sigma_1 \sigma_2} a_{\sigma_2}^+(\boldsymbol{p}) a_{\sigma_1}(\boldsymbol{p}) \frac{\bar{u}_j(\boldsymbol{p}, \sigma_1) u_i(\boldsymbol{p}, \sigma_2)}{2p_0} + \dots, \quad (3.16)$$

$$\int d^3x_1 \int d^3x_2 \ e^{-i\boldsymbol{p}(\boldsymbol{x}_1 - \boldsymbol{x}_2)} \ \psi_j(\boldsymbol{x}_2, t) \ \bar{\psi}_i(\boldsymbol{x}_1, t)$$

$$= \sum_{\sigma_1 \sigma_2} b_{\sigma_2}^+(\boldsymbol{p}) b_{\sigma_1}(\boldsymbol{p}) \frac{v_j(\boldsymbol{p}, \sigma_1) \bar{v}_i(\boldsymbol{p}, \sigma_2)}{2p_0} + \dots, \quad (3.17)$$

where we exhibit the bispinor indices for clarity. The ellipsis here represent terms corresponding to the creation or annihilation of particles moving in the "opposite" direction (negative momentum in the 3-direction), which disappear when evaluated in the many-body state with momentum $P \to \infty$. It is important to note that this happens irrespectively of whether one integrates over the

transverse momentum p_T or keeps it fixed, and that the transverse momentum dependence of the structures in Eqs. (3.16) and (3.17) surviving in the $P \to \infty$ limit is unambiguously defined in our model (in conventional terminology these are the leading—twist distribution functions).

The density operators required in Eqs. (3.2) and (3.3) can be obtained by applying appropriate spin projectors to Eqs. (3.16) and (3.17). Using the standard expressions for the spin density matrix of a pure state ($\sigma_1 = \sigma_2 \equiv \sigma$) one finds that in the limit $p^3 \to \infty$ and for fixed p_T

$$\frac{u(\boldsymbol{p},\sigma)\bar{u}(\boldsymbol{p},\sigma)}{2p_0} \to \gamma^0 \frac{1\pm\gamma_5}{2} \quad (\sigma = \pm 1/2). \quad (3.18)$$

Here σ is defined as the quark/antiquark spin projection along the 3–axis. Thus the unpolarized density is obtained by contracting both sides of Eqs. (3.16) and (3.17) with γ^0 ,

$$\operatorname{tr}[\gamma^0 \bar{\psi}\psi] \to \sum_{\sigma} a_{a\sigma}^{\dagger}(\boldsymbol{p}) a_{a\sigma}(\boldsymbol{p}),$$
 (3.19)

$$\operatorname{tr}[\gamma^0 \psi \bar{\psi}] \to \sum_{\sigma} b_{a\sigma}^{\dagger}(\boldsymbol{p}) b_{a\sigma}(\boldsymbol{p});$$
 (3.20)

the longitudinally polarized density is obtained by contracting with $\gamma^0 \gamma_5$.

The equal-time products in Eqs. (3.16) and (3.17) can be represented as appropriate limits of the time-ordered product of field operators, which is described by the Feynman Green function in the fast-moving nucleon,

$$\langle N_v | T \psi(\mathbf{x}_1, t_1) \bar{\psi}(\mathbf{x}_2, t_2) | N_v \rangle = i G_F^v(x_1, x_2).$$
 (3.21)

Without loss of generality we choose the equal time moment at t=0 and obtain

$$\frac{f_1^{u+d}(x, p_T)}{f_1^{\bar{u}+\bar{d}}(x, p_T)} = \frac{N_c P}{(2\pi)^3} \int d^3x_1 \int d^3x_2 \ e^{-i\boldsymbol{p}(\boldsymbol{x}_1 - \boldsymbol{x}_2)} \times (\mp i) \operatorname{tr}[G_F^v(0, \boldsymbol{x}_1; \pm 0, \boldsymbol{x}_2) \gamma^0]. \quad (3.22)$$

The Feynman Green function is given by the solution of the inhomogeneous Dirac equation Eq. (2.10) in the classical chiral field corresponding to the fast—moving nucleon, which is the static field of the rest frame boosted along the 3–direction with velocity v,

$$U_{\mathrm{cl}}^{\gamma_5,v}(\boldsymbol{x},t) \equiv U_{\mathrm{cl}}^{\gamma_5}(\boldsymbol{x}')$$

$$\left[\mathbf{x}' \equiv \left(\mathbf{x}_T, \frac{x^3 - vt}{\sqrt{1 - v^2}} \right) \right]. \tag{3.23}$$

Here and in the following we use primed variables to denote coordinates in the rest frame. Thanks to the Lorentz covariance of the Dirac equation Eq. (2.10) and the source term on its right—hand side it is possible to express this Green function in terms of the solutions of the rest—frame equation. Indeed, the Feynman Green function in the fast—moving nucleon in the limits of Eq. (3.22) can be

obtained as the Lorentz boost of the occupied and nonoccupied level parts of the rest-frame Green function,

$$G_F^v(0, \boldsymbol{x}_1; \pm 0, \boldsymbol{x}_2) = (\pm i) \left\{ \begin{array}{c} \sum \\ n \text{ occ} \\ \sum \\ n \text{ non-occ} \end{array} \right\}$$

$$\times S(v) \Phi_n(\mathbf{x}_1') \Phi_n^{\dagger}(\mathbf{x}_2') \gamma^0 S^{-1}(v) e^{-iE_n(t_1'-t_2')}.$$
 (3.24)

Here $(t'_{1,2}, x'_{1,2})$ denote the space–time coordinates that transform into $(0, x_{1,2})$ under a Lorentz boost in the 3–direction with velocity v,

$$(t'_{1,2}, \mathbf{x}'_{1,2}) \equiv \left(\frac{-vx_{1,2}^3}{\sqrt{1-v^2}}, \ \mathbf{x}_T, \ \frac{x_{1,2}^3}{\sqrt{1-v^2}}\right).$$
 (3.25)

The $\Phi_n(\mathbf{x}'_{1,2})$ are the time–independent single–particle wave functions in the nucleon rest frame, given by the solution of the Dirac equation Eq. (2.7), and S(v) is the transformation matrix corresponding to the Lorentz boost,

$$S(v) \equiv \exp\left(\frac{\eta}{2}\gamma^0\gamma^3\right) = \cosh\frac{\eta}{2} + \gamma^0\gamma^3 \sinh\frac{\eta}{2} \quad (3.26)$$
$$(v = \tanh\eta).$$

The formal proof that Eq. (3.24) represents the discontinuity of the Feynman Green function in the fast—moving mean field was given in Ref. [33] and relies essentially on the completeness of the set of single—particle wave functions. Substituting Eq. (3.24) into Eq. (3.22) one can straightforwardly evaluate the transverse momentum distributions in terms of the rest–frame single—particle wave functions. In the limit $v \to 1$ one has

$$S^{-1}(v) \gamma^0 S(v) = \frac{\gamma^0 + v\gamma^3}{\sqrt{1 - v^2}} \sim \frac{\gamma^+}{\sqrt{1 - v^2}},$$
 (3.27)

$$\gamma^+ \equiv \gamma^0 + \gamma^3. \tag{3.28}$$

Changing the integration variables in Eq. (3.22) from $x_{1,2}$ to the rest frame coordinates $x'_{1,2}$ and substituting the momentum representation of the rest–frame single–particle wave functions,

$$\Phi_n(\mathbf{x}'_{1,2}) = \int d^3 p'_{1,2} \ e^{i\mathbf{p}'_{1,2}\mathbf{x}'_{1,2}} \ \Phi_n(\mathbf{p}'_{1,2}), \quad (3.29)$$

one finds that they are effectively evaluated at rest–frame momenta $\,$

$$p_1' = p_2' = (p_T, \pm x M_N - E_n).$$
 (3.30)

This assignment is obtained here from the constraints inherent in the fast–moving nucleon expression Eq. (3.22) in the limit $v \to 1$; an alternative physical interpretation directly in the rest frame is provided in Sec. III C below. Finally, substituting the nucleon momentum P as defined

by Eq. (3.5), and taking the limit $v \to 1$, one obtains

$$\begin{cases}
f_1^{u+d}(x, p_T) \\
f_1^{\bar{u}+\bar{d}}(x, p_T)
\end{cases} = \frac{N_c M_N}{(2\pi)^3} \begin{cases} \sum_{n \text{ occ}} \\ \sum_{n \text{ non-occ}} \end{cases} \\
\times \Phi_n(\mathbf{p})^{\dagger} \gamma^0 \gamma^+ \Phi_n(\mathbf{p})$$

$$[\mathbf{p} \equiv (\mathbf{p}_T, \pm x M_N - E_n)]. \tag{3.31}$$

[For ease of notation we have dropped the prime on the rest frame momenta; all momenta in the following refer to the rest frame unless specified otherwise (in Sec. VI).] Formally one still needs to average Eq. (3.31) over the (iso-) rotational zero modes and project on states with definite spin-isposin quantum numbers [32]; however, in the case of the flavor-singlet unpolarized distributions here this operation is trivial and does not change the form of the expression.

In the quark distribution in Eq. (3.31) the summation extends over all occupied quark single–particle states, including the discrete level and the negative–energy Dirac continuum (see Fig. 1b). The antiquark distribution is given by the corresponding sum over non–occupied states in the spectrum, with the sign of the xM_N term reversed in the 3–component of the rest frame momentum Eq. (3.30). Equivalent representations of the quark distribution as a sum over non–occupied states, and of the antiquark distribution as a sum over occupied states, can be derived by making use of the completeness of the single–particle states (see below) [33],

$$\left. \begin{cases} f_1^{u+d}(x, p_T) \\ f_1^{\bar{u}+\bar{d}}(x, p_T) \end{cases} \right\} = -\frac{N_c M_N}{(2\pi)^3} \left\{ \sum_{\substack{n \text{ non-occ} \\ N_n \text{ occ}}} \sum_{\substack{n \text{ occ}}} \right\} \times \Phi_n(\mathbf{p})^{\dagger} \gamma^0 \gamma^+ \Phi_n(\mathbf{p}) \tag{3.32}$$

$$[\boldsymbol{p} \equiv (\boldsymbol{p_T}, \pm xM_N - E_n)].$$

In the case of the polarized distributions, the flavor–nonsinglet (isovector) combination appears in leading order of the $1/N_c$ expansion. An analogous calculation as in the case of the unpolarized distribution leads to the expressions (cf. Ref.[33])

$$\left. \begin{array}{l} g_1^{u-d}(x, p_T) \\ g_1^{\bar{u}-\bar{d}}(x, p_T) \end{array} \right\} = \mp \frac{N_c M_N}{3(2\pi)^3} \left\{ \begin{array}{l} \sum_{n \text{ occ}} \\ \sum_{n \text{ non-occ}} \end{array} \right\} \\
\times \Phi_n(\boldsymbol{p})^{\dagger} \tau^3 \gamma^0 \gamma^+ \gamma_5 \Phi_n(\boldsymbol{p}) \qquad (3.33)$$

$$[\mathbf{p} \equiv (\mathbf{p_T}, \pm xM_N - E_n)].$$

Here τ^3 denotes the Pauli matrix in quark flavor indices. The factor -1/3 arises from the integration over the (iso-) rotational zero modes and projection on the nucleon state with spin $S_3 = 1/2$ and isospin $T_3 = 1/2$ [32]. An alternative representation, analogous to Eq. (3.32), is

$$\left. \begin{array}{l} g_1^{u-d}(x, p_T) \\ g_1^{\bar{u}-\bar{d}}(x, p_T) \end{array} \right\} = \pm \frac{N_c M_N}{3(2\pi)^3} \left\{ \begin{array}{l} \sum_{n \text{ non-occ}} \\ \sum_{n \text{ occ}} \end{array} \right\} \\
\times \Phi_n(\mathbf{p})^{\dagger} \tau^3 \gamma^0 \gamma^+ \gamma_5 \Phi_n(\mathbf{p}) \qquad (3.34)$$

$$[\mathbf{p} \equiv (\mathbf{p_T}, \pm xM_N - E_n)].$$

The transverse momentum distributions can also be expressed in terms of the Feynman Green function of quarks in the nucleon rest frame. It is convenient to introduce the energy—momentum representation of the Feynman Green function as

$$G_F(x,y) = \int \frac{d^4 p_1}{(2\pi)^4} \int \frac{d^4 p_1}{(2\pi)^4} e^{-ip_1 x + ip_2 y} \times 2\pi \delta(p_1^0 - p_2^0) S_F(p_1^0; \mathbf{p}_1, \mathbf{p}_2), \quad (3.35)$$

whose spectral representation in the rest frame is

$$S_F(p_1^0; \boldsymbol{p}_1, \boldsymbol{p}_2) = \sum_n \frac{\Phi_n(\boldsymbol{p}_1)\Phi_n(\boldsymbol{p}_2)^{\dagger}\gamma^0}{p_1^0 - E_n + i0\sigma_n},$$
 (3.36)

where σ_n is defined in Eq. (2.14). The sums over occupied and non-occupied single-particle levels in Eq. (3.31) can be then expressed as contour integrals in the complex energy variable encircling the negative and positive-energy poles. These integrals can in turn be converted into integrals over the real energy axis by deforming the contours at infinity; see Ref. [32] for details. In this it is important that the UV cutoff respect the analytic properties of the unregularized theory and does not introduce spurious singularities. For the quark distribution one obtains

$$\begin{cases}
f_1^{u+d}(x, p_T) \\
f_1^{\bar{u}+\bar{d}}(x, p_T)
\end{cases} = \pm \operatorname{Im} \frac{N_c M_N}{(2\pi)^3} \int_{-\infty}^{\infty} \frac{dp^0}{2\pi} \times \operatorname{tr}[S_F(p^0; \boldsymbol{p}, \boldsymbol{p}) \gamma^+] \tag{3.37}$$

$$\left[\boldsymbol{p} \equiv (\boldsymbol{p}_T, \pm x M_N - p^0)\right].$$

The antiquark distribution is given by the negative of the expression for the quark distribution with x replaced by -x. The corresponding expressions for the flavornonsinglet polarized distribution are

$$\left. \begin{array}{l} g_{1}^{u-d}(x, p_{T}) \\ g_{1}^{\bar{u}-\bar{d}}(x, p_{T}) \end{array} \right\} = -\operatorname{Im} \frac{N_{c} M_{N}}{3(2\pi)^{3}} \int_{-\infty}^{\infty} \frac{dp^{0}}{2\pi} \\ \times \operatorname{tr}[S_{F}(p^{0}; \boldsymbol{p}, \boldsymbol{p}) \tau^{3} \gamma^{+} \gamma_{5}] \qquad (3.38)$$

$$\left[\boldsymbol{p} \equiv (\boldsymbol{p}_T, \pm x M_N - p^0)\right].$$

In the polarized case the antiquark distribution is given by the expression for the quark distribution with $x \to -x$ without change of the overall sign. Equations (3.37) and (3.38) are the starting point for calculating the p_T distribution by gradient expansion in the classical chiral field. They can also be used to derive equivalent representations of the quark distribution as a sum over nonoccupied states, or of the antiquark distribution as a sum over occupied states, by deforming the integration contour in the p^0 integral.

C. Rest frame interpretation

The expression Eq. (3.31) for the quark and antiquark distributions permit a simple interpretation directly in the nucleon rest frame, which explains the form of the rest–frame three–momentum Eq. (3.30) at which the single–particle wave functions are evaluated. It also reveals the role of the large– N_c limit in the derivation and emphasizes the analogy with the conventional mean–field approximation of nuclear physics.

The parton densities defined by Eqs. (3.2) and (3.3) can equivalently be regarded as the densities of quarks and antiquarks carrying a fraction x of the nucleon's light–cone "plus" momentum $P_N^+ \equiv P_N^0 + P_N^3$. As such they may be evaluated in any reference frame. In the rest frame $P_N^3 = 0$ and $P_N^0 = M_N$, and thus

$$P_N^+ = M_N \tag{3.39}$$

(see Fig. 2). In this frame the operator measuring the parton density counts quarks and antiquarks with plus momentum

$$p^+ = xM_N. (3.40)$$

In the mean-field approximation this operator removes a quark from an occupied single-particle state n with energy E_n and three-momentum p, which has both longitudinal and transverse components (in the case of the antiquark density, the operator puts a quark with the same momentum in an unoccupied state n). As the quark removed from the interacting system is not on mass-shell, the relation between its energy and three-momentum, and hence the relation between these variables and the external parameter x, are a priori not obvious and require discussion. The assignment of the quark three-momentum of Eq. (3.31) obtained from the derivation in Sec. III B [33] corresponds to

$$p^{+} = E_n + p^3. (3.41)$$

We now show that this assignment can be justified by inspection of the remnant system in the rest frame, i.e., the many–body state from which the quark or antiquark was removed. This system is on mass shell, and its kinematic variables can unambiguously be related to the external parameter x.

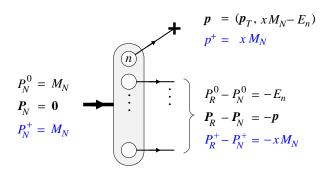


FIG. 2. (Color online) Interpretation of the rest frame expression of the transverse momentum—dependent quark density in the chiral quark—soliton model, Eq. (3.31). The operator removes a quark with 3-momentum p from the single-particle level n in the nucleon wave function (in the case of the antiquark density it would place a quark in an unoccupied level). The remnant system recoils with momentum -p and energy loss $-E_n$. The plus momentum loss calculated as the difference of the plus momenta of the remnant system and the initial nucleon state exactly compensates the plus momentum of the active quark, xM_N . This shows that the relativistic mean—field approximation conserves plus momentum at the order $O(N_c^0)$ (details see text).

Because three–momentum is conserved in equal–time quantization, the three–momentum imparted to the remnant system in the rest frame is

$$P_R - P_N = P_R = -p = O(N_c^0)$$
 (3.42)

(see Fig. 2). At the same time, in the mean-field approximation the energy difference between the remnant system and the initial nucleon state is determined by the energy of the removed quark,

$$P_R^0 - P_N^0 = -E_n = O(N_c^0).$$
 (3.43)

Note that the individual energies P_R^0 and P_N^0 are $O(N_c)$, but their difference is $O(N_c^0)$ and can be discussed quantitatively at this level. An important point is also that the kinetic energy associated with the recoil of the remnant system is of the order

$$E_{\text{recoil}} \sim \frac{p^2}{2M_N} = O(N_c^{-1})$$
 (3.44)

and can be neglected relative to Eq. (3.43). From Eqs. (3.42) and (3.43) we can calculate the plus momentum difference between the remnant system and the initial nucleon,

$$P_R^+ - P_N^+ = -E_n - p^3 = O(N_c^0).$$
 (3.45)

This is precisely the negative of the plus momentum of the removed quark, Eq. (3.41), obtained from the earlier derivation in Sec. III B. Thus we see that this assignment implies the conservation of plus momentum of the interacting system in leading order of the $1/N_c$ expansion, i.e., the individual changes in plus momenta of $O(N_c^0)$ add up

to zero at that order. The same applies of course to the transverse momenta. We emphasize that this argument does not neglect the interactions in the system but only relies on the mean–field approximation to the nucleon wave function. The conservation of plus momentum represents a nontrivial consequence of the consistency of the approximations made in this model.

D. Positivity and inequalities

The unpolarized transverse momentum distributions of quarks and antiquarks in the chiral quark–soliton model defined by Eqs. (3.2) and (3.3) are particle number densities in longitudinal and transverse momentum and should therefore be positive. It is easy to verify that their expressions in terms of single–particle wave functions, Eq. (3.31), are indeed manifestly positive. Noting that the hermitean matrix $\gamma^0 \gamma^+/2$ is a projector,

$$\left(\frac{\gamma^0 \gamma^+}{2}\right)^2 = \frac{\gamma^0 \gamma^+}{2} \tag{3.46}$$

we can rewrite Eq. (3.31) as

$$\left. \begin{cases} f_1^{u+d}(x, p_T) \\ f_1^{\bar{u}+\bar{d}}(x, p_T) \end{cases} \right\} = \frac{2N_c M_N}{(2\pi)^3} \left\{ \sum_{\substack{n \text{ occ} \\ n \text{ non-occ}}}^{\sum} \right\} \\
\times \left| \frac{\gamma^0 \gamma^+}{2} \Phi_n(\boldsymbol{p}) \right|^2 \tag{3.47}$$

$$[\mathbf{p} \equiv (\mathbf{p_T}, \pm xM_N - E_n)]. \tag{3.48}$$

Here the quark and antiquark distribution are expressed as a sum of explicitly positive terms. This property essentially relies on the completeness of quark single—particle states in the model. We note that the UV cutoff implicit in the effective chiral dynamics may in principle violate the positivity of the unregularized expression. We shall show in Sec. VF that the physical regularization schemes proposed there naturally preserve the positivity of the transverse momentum distributions.

The completeness of quark single–particle states also implies the existence of inequalities between the polarized and unpolarized transverse momentum distributions. An obvious consequence of the probabilistic nature of the densities defined by Eqs. (3.2) and (3.3), and Eqs. (3.7) and (3.8), is that

$$f_1^{a,\bar{a}}(x,p_T) \ge |g_1^{a,\bar{a}}(x,p_T)|$$
 (3.49)

for any given quark or antiquark flavor a [58]. Actually, in the large- N_c limit a stronger inequality was proved for the p_T -integrated densities [59], namely $f_1^a(x) \ge |3g_1^a(x)|$. The generalization of this proof to the case of the p_T distributions is straightforward, and one has

$$f_1^{a,\bar{a}}(x,p_T) \ge |3 g_1^{a,\bar{a}}(x,p_T)|.$$
 (3.50)

In particular, for the flavor combinations appearing in leading order of the $1/N_c$ expansion we obtain

$$f_1^{u+d}(x, p_T) \ge |3 g_1^{u-d}(x, p_T)|,$$
 (3.51)

$$f_1^{\bar{u}+\bar{d}}(x,p_T) \ge |3 g_1^{\bar{u}-\bar{d}}(x,p_T)|.$$
 (3.52)

In Secs. IV and V we show that these inequalities are satisfied by the model distributions obtained here, including the effects of the UV cutoff. This again illustrates the consistency of the scheme of approximations proposed here. The probabilistic character of the model p_T distributions expressed in the positivity condition and the inequalities also facilitates their matching with QCD quark and gluon distributions at the chiral symmetry–breaking scale; cf. the discussion in Sec. VII B.

E. Coordinate-space correlation function

The total $(p_T$ -integrated) parton densities in the chiral-quark soliton model can be represented as correlation functions of the massive quark fields of the model at light-like space-time separations [32]. Denoting the space—time separation four-vector by ξ , with $\xi^2 = 0$, one usually chooses a frame where $\xi^+ = 0$, $\xi_T = 0$, and $\xi^- \neq 0$ and performs the Fourier transform of the correlation function with respect to ξ^- . The equivalence of this representation of the parton density with the number density of quarks and antiquarks in the infinitemomentum frame was demonstrated in the chiral quarksoliton model in Ref. [33]. In a similar manner, the transverse momentum distributions in the model can now be represented in terms of correlation functions of the massive quark fields at a finite transverse separation $\xi_T \neq 0$, corresponding to a space-like separation of the fields, ξ^2 < 0 (see Fig. 3). It is straightforward to show that Eq. (3.31) can formally be represented as

$$\begin{cases}
f_1^{u+d}(x, p_T) \\
f_1^{\bar{u}+\bar{d}}(x, p_T)
\end{cases} = \int \frac{d^2 \xi_T}{(2\pi)^2} e^{i(\mathbf{p}_T \boldsymbol{\xi}_T)} \begin{cases}
\tilde{f}_1^{u+d}(x, \xi_T) \\
\tilde{f}_1^{\bar{u}+\bar{d}}(x, \xi_T),
\end{cases}$$
(3.53)

$$\left. \begin{cases} \tilde{f}_{1}^{u+d}(x,\xi_{T}) \\ \tilde{f}_{1}^{\bar{u}+\bar{d}}(x,\xi_{T}) \end{cases} \right\} \equiv \pm \frac{1}{8\pi} \int_{-\infty}^{\infty} d\xi^{-} e^{\pm ixP_{N}^{+}\xi^{-}/2} \\
\times \langle P_{N}|\bar{\psi}(0)\gamma^{+}\psi(\xi)|P_{N}\rangle_{\xi^{+}=0}.$$
(3.54)

Here P_N is the nucleon four-momentum, with P_N^+ arbitrary, $P_{N,T} = 0$, and $P_N^- = M_N^2/P_N^+$. The sum over quark flavors (u,d) is implied in Eq. (3.54). Conversely, the coordinate-space correlation function can be obtained as the two-dimensional Fourier transform of the

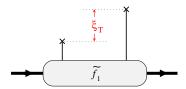


FIG. 3. (Color online) Coordinate–space correlation function $\tilde{f}_1^{u+d}(x,\xi_T)$ and $\tilde{f}_1^{\bar{u}+\bar{d}}(x,\xi_T)$, Eq. (3.54) representing the Fourier transform of the transverse momentum distributions in the chiral quark–soliton model.

 p_T distribution,

$$\tilde{f}_{1}^{u+d}(x,\xi_{T}) \equiv \int d^{2}p_{T} e^{-i\mathbf{p}_{T}\xi_{T}} f_{1}^{u+d}(x,p_{T})$$

$$= 2\pi \int_{0}^{\infty} dp_{T} p_{T} J_{0}(p_{T}\xi_{T}) f_{1}^{u+d}(x,p_{T}),$$
(3.55)

and similarly for the antiquark distribution. Here J_0 is the cylindrical Bessel function. In particular, the value at $\xi_T = 0$ corresponds to the total (p_T -integrated) parton density,

$$\tilde{f}^{u+d}(x, \xi_T = 0) = f^{u+d}(x),$$

 $\tilde{f}^{\bar{u}+\bar{d}}(x, \xi_T = 0) = f^{\bar{u}+\bar{d}}(x).$ (3.56)

Here as before in Sec. III A, it is assumed that the integral over transverse momenta in the model converge; the role of the UV cutoff in the coordinate–space correlation function will be discussed in Sec. V G.

We emphasize that we regard Eq. (3.54) strictly as a definition within the effective model and make no attempt to relate the bilinear quark operator in massive quark fields to any QCD operators with finite transverse separation. As discussed in Sec. I, the proper definition of such operators in QCD faces considerable challenges (gauge invariance and path dependence, rapidity divergences, renormalization properties) and is the subject of on–going research. In our dynamical model the operator with finite transverse separation of the fields is well–defined, and its nucleon matrix element can be calculated within the $1/N_c$ expansion.

Finally, the corresponding coordinate—space correlation functions for the flavor—nonsinglet polarized distribution are

$$\left. \begin{array}{l} \tilde{g}_{1}^{u+d}(x,\xi_{T}) \\ \\ \tilde{g}_{1}^{\bar{u}+\bar{d}}(x,\xi_{T}) \end{array} \right\} \equiv \frac{1}{8\pi} \int_{-\infty}^{\infty} d\xi^{-} e^{ixP_{N}^{+}\xi^{-}/2} \\ \\ \times \langle P_{N} | \bar{\psi}(0)\tau^{3}\gamma^{+}\gamma_{5}\psi(\xi) | P_{N} \rangle_{\xi^{+}=0}.$$
(3.57)

Their relation to the p_T distributions is analogous to the unpolarized case, cf. Eq. (3.53).

IV. VALENCE QUARK TRANSVERSE MOMENTUM

A. Transverse momentum distribution

Using the expressions derived in Sec. III B we now want to calculate the transverse momentum distributions of quarks and antiquarks in the chiral quark—soliton model and study their behavior. It will be convenient to discuss separately the "valence" (charge—nonsinglet, or quark minus antiquark) and the "sea" (antiquark) distributions, as the two receive contributions from different classes of configurations in the nucleon wave function and consequently show different behavior, especially at large values of p_T . In this section we study the valence quark transverse momentum distributions; the sea quark distributions will be considered in Sec. V.

The flavor-singlet unpolarized valence quark density

$$f_1^{u+d-\bar{u}-\bar{d}}(x) \equiv f_1^{u+d}(x) - f_1^{\bar{u}+\bar{d}}(x)$$
 (4.1)

in the chiral quark-soliton model is dominated by the contribution of the discrete bound-state level in the quark single-particle spectrum. The contribution of the Dirac continuum to the valence quark density was calculated in Ref. [32] and found to be $\lesssim 5\%$ of the total at non-exceptional values of x; its integral over x is zero, as the discrete level occupied by N_c quarks already accounts for the entire baryon number of the nucleon. The transverse momentum distribution of valence quarks is therefore also dominated by the bound-state level, and we can neglect the Dirac continuum contribution in our numerical study. The explicit form of the bound state wave function of the discrete level is given in Appendix B (see also Appendix B of Ref. [32]). Evaluating the discrete level term in the quark distribution given by Eq. (3.31), and the antiquark distribution given by Eq. (3.32), we obtain

$$\begin{cases}
f_{1,\text{lev}}^{u+d}(x, p_T) \\
f_{1,\text{lev}}^{\bar{u}+\bar{d}}(x, p_T)
\end{cases} = \pm \frac{N_c M_N}{4\pi p^2} \left[h^2(p) + j^2(p) - \frac{2p^3}{p} h(p) j(p) \right]$$
(4.2)

$$\[p^3 \equiv \pm x M_N - E_{\text{lev}}, \ p \equiv |\boldsymbol{p}| = \sqrt{\boldsymbol{p}_T^2 + (p^3)^2} \].$$

Here h(p) and j(p) are the radial wave functions of the bound–state level in momentum representation as defined in Eq. (B8). The valence quark p_T distribution in our approximation is then given by [cf. Eq. (4.1)]

$$f_1^{u+d-\bar{u}-\bar{d}}(x,p_T) = f_{1,\text{lev}}^{u+d}(x,p_T) - f_{1,\text{lev}}^{\bar{u}+\bar{d}}(x,p_T).$$
 (4.3)

We evaluate the p_T distributions with $M=0.35\,\mathrm{GeV}$, the self–consistent soliton profile described in Appendix A, Eqs. (A4)–(A7), $E_{\mathrm{lev}}=0.466\,M$ as obtained from

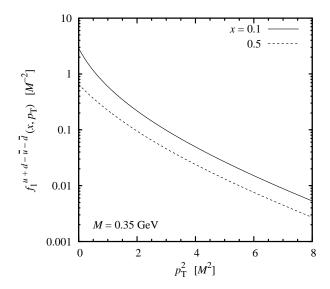


FIG. 4. Transverse momentum distribution of flavor–singlet valence quarks, $f_{1,\mathrm{val}}^{u+d}(x,p_T)$, Eq. (4.1), as a function of p_T^2 , at x=0.1 (solid line) and 0.5 (dotted line). A Gaussian distribution would correspond to a straight line in the coordinates of this plot. [Self–consistent soliton profile Eq. (A4) with $M=0.35\,\mathrm{GeV}$ and $M_N=3.26\,M.$]

Eq. (B3), and $M_N = 3.26 \, M$. As always, we put $N_c = 3$ when using large– N_c expressions such as Eq. (4.2) as a numerical approximation. The resulting p_T distributions are shown in Fig. 4 for two values of x. One sees that the valence distributions are concentrated at momenta of the order $p_T^2 \sim M^2$, which corresponds to the inverse spatial size of the mean field; cf. Appendix A and Fig. 20. The distributions are roughly of Gaussian shape. Such behavior is obtained in a variety of bound–state models with fixed particle number (see Ref. [60] for a recent discussion) and seems to be a generic consequence of the spatial localization of the bound–state wave function.

The transverse momentum integral of the valence quark distribution is UV-finite and does not require a cutoff. Because the p_T distribution is numerically concentrated at low values $p_T^2 \sim \text{few } M^2$ we do not consider the effect of possible UV regularizations on the valence quark p_T distribution. Indeed, there are physical reasons why the p_T -integrated valence quark density should not be regularized. Leaving it unregularized ensures that the baryon sum rule is satisfied in the model, as the baryon number resulting from the bound-state level contribution is unity and that from the Dirac continuum integrates to zero [32, 33]. It also ensures that the momentum sum rule is satisfied in the model [32, 56], i.e., that the valence and sea quark distributions together carry the entire light-cone momentum of the nucleon — a property of central importance for the interpretation of the model parton distributions and their matching with QCD (cf. the discussion in Sec. VIIB).

Using the fact that $|p^3| < p$ it is easily seen that the ex-

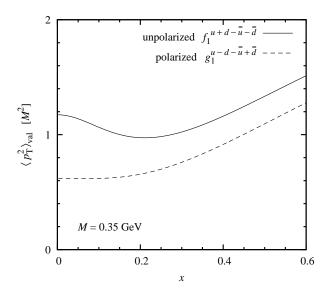


FIG. 5. Average transverse momentum squared of the valence quark distribution, $\langle p_T^2 \rangle_{\rm val}(x)$, Eq. (4.5), as a function of x. Solid line: Flavor–singlet unpolarized distribution $f_1^{u+d-\bar{u}-\bar{d}}$. Dashed line: Flavor–nonsinglet polarized distribution, $g_1^{u-d-\bar{u}+\bar{d}}$.

pression in brackets in Eq. (4.2) is positive, irrespectively of the sign of the radial wave functions. The discrete level contribution to the unpolarized quark and antiquark p_T distributions, Eq. (4.2), thus satisfies

$$f_{1,\text{lev}}^{u+d}(x, p_T) > 0, \qquad f_{1,\text{lev}}^{\bar{u}+\bar{d}}(x, p_T) < 0, \qquad (4.4)$$

for all x and p_T . For the quark distribution this in accordance with the positivity condition Eq. (3.48). The antiquark p_T distribution in the model includes the positive Dirac continuum contribution in addition to the discrete level contribution Eq. (4.2) and is also positive (see Sec. V). This also guarantees positivity of the total (p_T -integrated) antiquark density, as discussed in Ref. [32].

B. Average transverse momentum

Because the distribution of valence quarks decreases rapidly at large transverse momenta, one may consider the average of p_T^2 at fixed x as a measure of the overall width of the distribution,

$$\langle p_T^2 \rangle_{\text{val}}(x) \equiv \frac{\int d^2 p_T \, p_T^2 \, f_1^{u+d-\bar{u}-\bar{d}}(x, p_T)}{\int d^2 p_T \, f_1^{u+d-\bar{u}-\bar{d}}(x, p_T)}.$$
 (4.5)

Figure 5 (solid line) shows this quantity as a function of x, as obtained within our approximation. One sees that the typical transverse momenta in the valence quark distribution are of the order $p_T^2 \sim M^2$, corresponding to the inverse spatial size of the mean field [cf. Eqs. (A4)–(A7)],

and that the average varies only weakly with x over a wide range, as expected from phenomenological models [60]. The increase toward larger values of x indicates that the spatial size of configurations contributing to the parton density decreases at larger values of x, which is a general feature of a bound state with fixed particle number. Note, however, that the mean–field approximation employed here is justified only for non–exceptional momentum fractions $x \sim 1/N_c$ and cannot be used to study the large–x limit of parton densities.

C. Polarized distribution

In a similar manner, the flavor–nonsinglet polarized valence quark density

$$g_1^{u-d-\bar{u}+\bar{d}}(x) \equiv g_1^{u-d}(x) - g_1^{\bar{u}-\bar{d}}(x),$$
 (4.6)

in the chiral quark–soliton model is dominated by the contribution of the discrete bound state level. The level contributions to the p_T distribution of polarized quarks defined by Eq. (3.33), and to the antiquark distribution defined by Eq. (3.34), evaluate to [cf. Eq. (4.2)]

$$\left. \begin{cases}
g_{1,\text{lev}}^{u-d}(x, p_T) \\
g_{1,\text{lev}}^{\bar{u}-\bar{d}}(x, p_T)
\end{cases} = \frac{N_c M_N}{3(4\pi p^2)} \left\{ h^2(p) + \left[\frac{2(p^3)^2}{p^2} - 1 \right] j^2(p) - \frac{2p^3}{p} h(p) j(p) \right\}$$
(4.7)

$$\[p^3 \equiv \pm x M_N - E_{\text{lev}}, \ p \equiv |\boldsymbol{p}| = \sqrt{\boldsymbol{p}_T^2 + (p^3)^2} \].$$

The resulting distribution is positive and similar in shape to the unpolarized distribution (see Fig. 6, dashed line). The somewhat faster decrease of the polarized distribution at large p_T is due to the lower component of the bound–state level wave function [for $j(p) \equiv 0$ the shape would be the same as that of the unpolarized distribution] and attests to the relativistic nature of the mean–field picture of the nucleon at large N_c . The average $\langle p_T^2 \rangle$ of the polarized distribution, defined in analogy with Eq. (4.5), is shown in Fig. 5 (dashed line) as a function of x. One sees that it is systematically smaller than that of the flavor–singlet unpolarized distribution, which again is a relativistic effect [61]. Similar behavior is found in relativistic bound state models of the valence quark distributions with fixed particle number; see e.g. Refs. [49, 50].

It is interesting to note that the unpolarized and polarized quark distributions resulting from the bound-state level, Eqs. (4.2) and (4.7), satisfy the general large- N_c inequality for the transverse momentum distribution, Eq. (3.51). Because numerically $g_{1,\text{lev}}^{u-d}(x,p_T) > 0$, and also $f_{1,\text{lev}}^{u+d}(x,p_T) > 0$, we may replace the absolute values of the distributions by the distributions themselves when

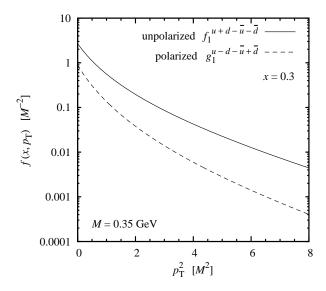


FIG. 6. The transverse momentum distribution of flavor–nonsinglet polarized valence quarks, $g_1^{u-d-\bar{u}+\bar{d}}(x,p_T)$, Eq. (4.6), as a function of p_T^2 , at x=0.3. Also shown for comparison is the flavor–singlet unpolarized valence quark distribution $f_1^{u+d-\bar{u}-\bar{d}}(x,p_T)$ at the same value of x, cf. Eq. (4.1) and Fig. 4.

testing the inequality. If we then form the difference between the left– and right–hand sides of Eq. (3.51) with the expressions Eqs. (4.2) and (4.7), we obtain

$$f_{1,\text{lev}}^{u+d}(x, p_T) - 3g_{1,\text{lev}}^{u-d}(x, p_T)$$

$$= \frac{2N_c M_N}{(4\pi p^2)} \left[1 - \frac{(p^3)^2}{p^2} \right] j^2(p), \tag{4.8}$$

which is manifestly positive because $|p^3| \leq p$. The inequality for the corresponding sea quark distributions, which are dominated by the contribution of the Dirac continuum of single–particle quark states, is discussed in Sec. V J.

V. SEA QUARK TRANSVERSE MOMENTUM

A. Gradient expansion

We now turn to the transverse momentum distributions of sea quarks in the chiral quark—soliton model. The sea quark distributions receive contributions from a broad range of quark single—particle states extending up to the cutoff scale. Our first concerns are to study how the distributions of sea quarks behave at large p_T , how they are affected by the UV cutoff, and how they can be regularized in a way that satisfies basic physical requirements (longitudinal momentum conservation, charge conservation, analyticity) and provides distributions with a clear physical interpretation. We can then compute the sea quark p_T distributions numerically and

compare them to those of the valence quarks. For simplicity we consider first the distribution of unpolarized flavor—singlet sea quarks; the flavor—nonsinglet polarized sea will be treated summarily in Sec. V J.

A powerful analytic method for evaluating the sea quark densities in the chiral quark–soliton model is the gradient expansion, in which one expands the quark Green function in powers of derivatives of the classical chiral field [32]. Here we adapt this method to study the p_T distributions. The leading–order gradient expansion contains the (exact) leading power behavior of the p_T distributions at large p_T , which reveals the role of dynamical chiral symmetry breaking and allows us to study the effect of the UV cutoff . The leading–order expression also provides us with an accurate "interpolating" approximation to the sea quark distributions at all values of p_T , which we use for a numerical estimate of the distributions in Sec. V H.

To derive the gradient expansion, we start from the expression of the quark and antiquark p_T distributions in terms of the Feynman Green function in the classical chiral field in the nucleon rest frame, Eq. (3.37). The Green function is defined as the solution of the inhomogeneous Dirac equation Eq. (2.10). Following Ref. [62], we can regard it as the matrix element of a formal operator between 4-dimensional "position eigenstates" $|x| \equiv |x^0, x|$,

$$G_F(x,y) = (x | [i\hat{\partial} - MU^{\gamma_5}]^{-1} | y),$$
 (5.1)

where $i\partial$ is the 4–dimensional "momentum operator" and $\hat{\partial} \equiv \gamma^{\alpha}\partial_{\alpha}$, cf. Eq. (2.2). Equivalently, the energy–momentum representation of the Green function Eq. (3.35) can be expressed as the matrix element of the same operator between conjugate momentum eigenstates $|p\rangle \equiv |p^0, p\rangle$, with $(x|p) = e^{-ipx}$,

$$2\pi\delta(p_1^0 - p_2^0)S_F(p_1^0; \mathbf{p}_1, \mathbf{p}_2)$$

= $(p_1|[i\hat{\partial} - MU^{\gamma_5}]^{-1}|p_2).$ (5.2)

The gradient expansion is now performed by formally expanding the inverse Dirac operator in gradients of the classical chiral field:

$$[i\hat{\partial} - MU^{\gamma_5}]^{-1}$$

$$= [D^{-1} - M(i\hat{\partial}U^{\gamma_5})]^{-1} (i\hat{\partial} + MU^{-\gamma_5})$$

$$= [D + MD(i\hat{\partial}U^{\gamma_5})D$$

$$+ M^2 D(i\hat{\partial}U^{\gamma_5})D(i\hat{\partial}U^{\gamma_5})D + \dots]$$

$$\times (i\hat{\partial} + MU^{-\gamma_5}), \qquad (5.3)$$

where

$$D \equiv (-\partial^2 - M^2 + i0)^{-1} \tag{5.4}$$

is the free massive scalar Feynman Green function. The leading-order contribution to the quark and antiquark p_T distributions Eq. (3.37) is contained in the terms of order M^2 collected after multiplying out the factors in Eq. (5.3). Their matrix elements between 4-dimensional

momentum eigenstates are calculated by inserting complete sets of momentum eigenstates between the operators. The basic matrix elements are

$$(k_2|U^{\pm\gamma_5}|k_1) = 2\pi\delta(k_1^0 - k_2^0) \widetilde{U}_{cl}^{\pm\gamma_5}(\mathbf{k}_2 - \mathbf{k}_1), \qquad (5.5)$$
$$\widetilde{U}_{cl}^{\pm\gamma_5}(\mathbf{k}) \equiv \frac{1}{2}(1 \pm \gamma_5)\widetilde{U}_{cl}(\mathbf{k})$$
$$+ \frac{1}{2}(1 \mp \gamma_5)\widetilde{U}_{cl}(-\mathbf{k})^{\dagger}, \qquad (5.6)$$

where

$$\widetilde{U}_{cl}(\boldsymbol{k}) \equiv \int d^3x \ e^{-i\boldsymbol{x}\boldsymbol{k}} \left[U_{cl}(\boldsymbol{x}) - 1 \right]$$
 (5.7)

is the Fourier transform of the static classical chiral field in the rest frame [the Fourier transform of $U^{\dagger}(\boldsymbol{x})$ is given by $\widetilde{U}(-\boldsymbol{k})^{\dagger}$], and

$$(p_2|D|p_1) = (2\pi)^4 \,\delta^{(4)}(p_2 - p_1) \,D(p_1), \qquad (5.8)$$

$$D(p) \equiv \frac{1}{p^2 - M^2 + i0}. (5.9)$$

The relevant part of the Green function thus becomes

$$S_{F}(p^{0}; \boldsymbol{p}, \boldsymbol{p})$$

$$= M^{2} \int \frac{d^{3}k}{(2\pi)^{3}} \left[D(p)D(p-k)\hat{k}\widetilde{U}_{cl}^{\gamma_{5}}(\boldsymbol{k})\widetilde{U}_{cl}^{-\gamma_{5}}(-\boldsymbol{k}) + D^{2}(p)D(p-k)\hat{k}\widetilde{U}_{cl}^{\gamma_{5}}(\boldsymbol{k})(-\hat{k})\widetilde{U}_{cl}^{\gamma_{5}}(-\boldsymbol{k})\hat{p} \right]$$

$$\left[p \equiv (p^{0}, \boldsymbol{p}), \ k \equiv (0, \boldsymbol{k}) \right],$$
(5.10)

where $\hat{k} \equiv k^{\alpha} \gamma_{\alpha}$ as in Eq. (2.2). Substituting this expression in Eq. (3.37), evaluating the trace over spinor indices, and using the symmetry of the bilinear forms under $k \to -k$, we finally obtain

$$\begin{cases}
f_{1,\text{grad}}^{u+d}(x, p_T) \\
f_{1,\text{grad}}^{\bar{u}+\bar{d}}(x, p_T)
\end{cases} \\
= \pm \frac{4N_c M_N M^2}{(2\pi)^3} \int \frac{d^3k}{(2\pi)^3} \operatorname{tr}_{\text{fl}} \left[\widetilde{U}_{\text{cl}}(\mathbf{k}) \widetilde{U}_{\text{cl}}(\mathbf{k})^{\dagger} \right] \\
\times \operatorname{Im} \int \frac{dp^0}{2\pi} \left[D(p-k) D(p) k^+ \\
- D(p-k) D^2(p) k^2 p^+ \right] \\
\left[p \equiv (p^0, \mathbf{p}_T, \pm x M_N - p^0) \right].
\end{cases} (5.11)$$

Because of the symmetry of the combined momentum integrals the expression on the right-hand side is actually the same in both cases, and one has

$$f_{1,\text{grad}}^{\bar{u}+\bar{d}}(x,p_T) = f_{1,\text{grad}}^{u+d}(x,p_T)$$
 (5.12)

in leading—order gradient expansion. In the following, for simplicity, we use the upper expression also for the antiquark distribution.

Equation (5.11) expresses the sea quark transverse momentum distribution in terms of the Fourier transform of

the classical chiral field in the rest frame and an explicitly calculable loop integral over the free massive quark propagators, and are our starting point for the discussion of their physical properties. When integrating over the transverse momentum p_T , Eq. (5.11) reproduces the gradient expansion for the parton densities of Refs. [32, 33]. The latter were shown to be equivalent to the gradient expansion of moments of local twist–2 operators in the effective chiral model.

The gradient expansion Eq. (5.11) contains the leading power–like asymptotic behavior of the transverse momentum distribution at large momenta $p_T^2 \gg M^2$, as shown in detail in Sec. VD below. This important property follows from chiral invariance, which dictates that coefficients with higher mass dimension in an expansion in $1/p_T^2$ necessarily involve higher derivatives of the classical chiral field [63]. The gradient expansion therefore represents an ideal tool to evaluate the p_T distributions at large p_T and study the role of the UV regularization.

In the context of the exact representation of the quark/antiquark distributions as sums over quark singleparticle levels, Eqs. (3.31) and (3.32), the gradient expansion approximates the contribution from the Dirac continuum, i.e., quark scattering states distorted by the classical chiral field. The contribution of the discrete bound-state level with its normalizable wave function is not contained in the expanded Green function. In the sea quark p_T distribution the Dirac continuum contribution is numerically dominant, especially at large momenta $p_T^2 \gg M^2$, and can reliably be computed using the gradient expansion. At lower momenta $p_T^2 \sim M^2$, as well as in the integral over p_T , the contribution of the discrete level becomes numerically relevant. An "interpolating" approximation which includes the contribution from the bound-state level will be discussed in Sec. VI. In the following studies of the large- p_T behavior of the distributions and the role of the UV cutoff we can safely neglect the level contribution and take the sea quark distribution as defined by the gradient expansion.

B. Representation in light-cone variables

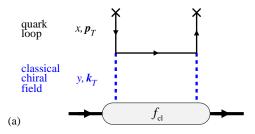
An interesting interpretation of the sea quark distribution is obtained by expressing the result of the leading–order gradient expansion Eq. (5.11) in terms of light–cone variables. The integral over the quark rest–frame energy p^0 in Eq. (5.11) can be rewritten as

$$\int \frac{dp^{0}}{2\pi} \left\{ \dots \right\}_{p=(p^{0}, p_{T}, xM_{N} - p^{0})}$$

$$= \int \frac{dp^{0}}{2\pi} \int \frac{dp^{3}}{2\pi} 2\pi \delta(p^{0} + p^{3} - xM_{N}) \left\{ \dots \right\}$$

$$= \frac{1}{2} \int \frac{dp^{+}}{2\pi} \int \frac{dp^{-}}{2\pi} 2\pi \delta(p^{+} - xM_{N}) \left\{ \dots \right\}$$

$$= \frac{1}{2} \int \frac{dp^{-}}{2\pi} \left\{ \dots \right\}_{p^{+} = xM_{N}}.$$
(5.13)



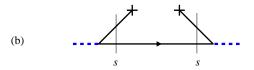


FIG. 7. (Color online) (a) Structure of the leading—order gradient expansion of the sea quark distribution Eq. (5.16). The classical chiral field carries light—cone momentum fraction y and transverse momentum k_T . It couples to a quark loop in which the antiquark carries light—cone momentum fraction x < y and transverse momentum p_T . (b) Time—ordered interpretation of the quark loop integral. The classical chiral field creates a quark—antiquark pair with invariant mass s, Eq. (5.33). The UV cutoff of the chiral model can be implemented in the form of a cutoff in s, Eq. (5.56).

We introduce the light–cone fraction y of the momentum of the static chiral field $(k^0 \equiv 0)$ as

$$y \equiv k^3/M_N. \tag{5.14}$$

The light–cone components of the chiral field's momentum in the rest frame are then given by

$$k^+ = -k^- = k^3 = yM_N.$$
 (5.15)

Equation (5.11) can then be expressed as an integral over light–cone momentum fractions as

$$f_{1,\text{grad}}^{\bar{u}+\bar{d}}(x,p_T) = \int \frac{dy}{y} \int d^2k_T f_{\text{cl}}(y, \boldsymbol{k}_T) \times f_{q\bar{q}}(x,y;\boldsymbol{p}_T,\boldsymbol{k}_T).$$
 (5.16)

Here $f_{\rm cl}$ denotes the light–cone momentum distribution of the classical chiral field of the soliton, defined as

$$f_{\rm cl}(y, \mathbf{k}_T) \equiv \frac{F_{\pi}^2 M_N^2 y}{(2\pi)^3} \operatorname{tr}_{\rm fl} \left[\widetilde{U}_{\rm cl}(\mathbf{k}) \widetilde{U}_{\rm cl}(\mathbf{k})^{\dagger} \right], \quad (5.17)$$
$$\left[\mathbf{k} = (\mathbf{k}_T, y M_N) \right].$$

The function $f_{q\bar{q}}$ describes the light-cone momentum distribution of a quark-antiquark pair,

$$f_{q\bar{q}}(x, y; \mathbf{p}_T, \mathbf{k}_T) \equiv \frac{2N_c M^2}{(2\pi)^3 F_{\pi}^2} \operatorname{Im} \int \frac{dp^-}{2\pi} D(p - k) \times \left[D(p)k^+ - D^2(p) k^2 p^+ \right]$$
 (5.18)
$$(p^+ = xM_N, k^+ = -k^- = yM_N).$$

Equation (5.16) permits a simple interpretation of the nucleon's sea quark distribution in gradient expansion (see Fig. 7a). The classical chiral with light–cone momentum fraction y and transverse momentum k_T "creates" a quark–antiquark pair, of which either the quark or the antiquark is observed with light–cone momentum fraction x and transverse momentum p_T . Explicit calculation below shows that $f_{q\bar{q}}$ is nonzero only if x < y, as required by light–front kinematics.

The gradient expansion Eq. (5.16) contains the leading asymptotic behavior of the transverse momentum distribution at large p_T . For our subsequent discussion we would like to exhibit this behavior in a simple form. It turns out that in the region $p_T^2 \gg M^2$ Eq. (5.16) and its ingredients permit further simplification. The components of the 3–momentum of the classical chiral field in the rest frame are of the order of the inverse radius of the chiral field,

$$|\mathbf{k}_T| \sim R^{-1},$$
 (5.19)

$$k^3 \equiv yM_N \sim R^{-1}.$$
 (5.20)

The typical radius, as determined by the minimum of the classical energy of the soliton, is of the order $R \sim M^{-1}$ [cf. Appendix A]. For transverse momenta in the region $p_T^2 \gg M^2$ we can therefore neglect the dependence of the quark loop integral in Eq. (5.16) on k_T and k^- . We suppose that the integral over y is dominated by non-exceptional values $y \gtrsim x$, which will be borne out by explicit calculation (see below). Furthermore, we can neglect the second term in Eq. (5.11), as it carries an extra factor of $-k^2 \sim R^{-2}$. With these simplifications Eq. (5.16) takes the form

$$f_{1,\text{grad}}^{\bar{u}+\bar{d}}(x,p_T) = \int_x^\infty \frac{dy}{y} f_{\text{cl}}(y) f_{q\bar{q}}(x/y,p_T), \quad (5.21)$$

where $f_{\rm cl}(y)$ is the light–cone momentum distribution of the classical chiral field integrated over transverse momenta,

$$f_{\rm cl}(y) \equiv \int d^2k_T \ f_{\rm cl}(y, \mathbf{k}_T)$$

$$= \frac{F_{\pi}^2 M_N^2 y}{(2\pi)^3} \int d^2k_T \ \text{tr}_{\rm fl} \left[\widetilde{U}_{\rm cl}(\mathbf{k}) \widetilde{U}_{\rm cl}(\mathbf{k})^{\dagger} \right] \quad (5.22)$$

$$(k^3 = y M_N).$$

The function $f_{q\bar{q}}(z, p_T)$ describes the light-cone and transverse momentum distribution of the quark-antiquark pair created by the classical chiral field in the collinear approximation, $\mathbf{k}_T = 0$ and $k^2 = 0$,

$$f_{q\bar{q}}(z, p_T) \equiv \frac{2N_c M^2}{(2\pi)^3 F_\pi^2} \operatorname{Im} \int \frac{dp^-}{2\pi} D(p - k) \times D(p) k^+$$

$$(p^+ = zk^+, k^- = 0, \mathbf{k}_T = 0).$$
(5.23)

Here z denotes the fraction of the chiral field's light–cone momentum carried by the quark in the pair,

$$z \equiv x/y; \tag{5.24}$$

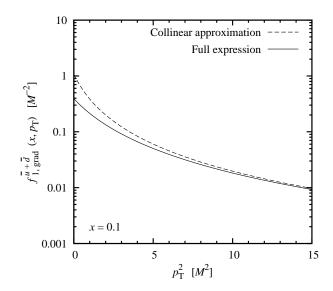


FIG. 8. Gradient expansion of the sea quark transverse momentum distribution at x=0.1. Solid line: Full expression, Eq. (5.16). Dashed line: Collinear approximation for $p_T^2 \gg M^2$, Eq. (5.23). [Self-consistent soliton profile Eq. (A4), $M=0.35 \,\text{GeV}, M_N=3.26 \,M.$]

the fraction carried by the antiquark is

$$\bar{z} \equiv 1 - z. \tag{5.25}$$

We retain the quark mass M in the free propagators Eq. (5.9) in Eq. (5.23). Thus, formally, the approximation Eq. (5.21) corresponds to the limit of large radius of the chiral field, $R\gg M^{-1}$, at fixed quark mass M. We refer to Eq. (5.21) as the collinear approximation. It has the same structure as the DGLAP evolution equations describing parton splitting in perturbative QCD in the collinear approximation. Note that the simplifications made here — integration over the chiral field's k_T independently of p_T , and neglect of k^2 — are parametrically justified in the domain $p_T^2\gg M^2$, and that Eq. (5.21) captures the exact leading behavior of the model p_T distribution in this region.

In Fig. 8 we compare the p_T distributions obtained from the full expression Eq. (5.16) and the collinear approximation Eq. (5.23) at a typical values x=0.1 (the distributions shown here were regularized with a Pauli–Villars cutoff, described in Sec. VF below). One sees that the collinear approximation accurately reproduces the full gradient expansion with better than 30% accuracy above $p_T^2 \sim 5 \, M^2$. In the following investigations of the structure of the distributions at large p_T and the role of the UV cutoff we can therefore use the simpler collinear expression Eq. (5.16); for numerical estimates at finite p_T we use shall use the full expression Eq. (5.16).

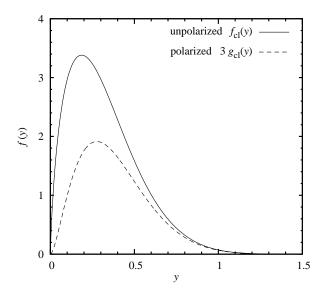


FIG. 9. Light–cone momentum distributions of the classical chiral field in the large– N_c nucleon. Solid line: Flavor–singlet unpolarized distribution $f_{\rm cl}(y)$, Eq. (5.22). as appears in the convolution integral Eq. (5.21). The distribution shown here corresponds to the self–consistent soliton profile Eq. (A4), with $M=0.35~{\rm GeV}$ and $M_N=3.26~M$. Dashed line: Flavor–nonsinglet polarized distribution $g_{\rm cl}(y)$, Eq. (5.71), as appears in Eq. (5.70). The plot shows $3~g_{\rm cl}(y)$, which is constrained by the positivity condition Eq. (5.78).

C. Momentum distribution of classical field

We first consider the light-cone momentum distribution of the classical chiral field, defined by Eq. (5.22). It can be evaluated using the explicit expression given in Eq. (C5) in Appendix C and the soliton profile parametrization Eqs. (A4)–(A7) in Appendix A. The numerical distribution is shown in Fig. 9 (solid line). One sees that the light-cone momentum distribution of the chiral field extends over a broad range of momentum fractions $y \sim 0.1 - 0.5$. It is not limited to values $y \ll 1$, as would be the case for single pions emitted by valence quarks, and in this sense reflects the complex interactions in the nucleon in the mean-field approximation (cf. our discussion of parton correlations in Sec. VIIB below). Note that in this classical approach based on large- N_c limit the chiral field's light-cone momentum fraction y is not limited to values y < 1; however, the distributions become exponentially small in the limit $y \to \infty$ [32]. Comparison of the results obtained with the selfconsistent soliton profile Eq. (A4) and the variational profile Eq. (A8) shows that the bulk distributions are not sensitive to the details of the profile and represent stable features of the model [64].

D. Structure of quark-antiquark pair

We now turn to the light–cone momentum distribution of the quark–antiquark pair in the gradient expansion of the sea quark distribution, defined by Eq. (5.18). We first study it without the UV cutoff; the implementation of the cutoff will be considered in the following subsection. The integral over p^- can be calculated straightforwardly by closing the integration contour in the complex plane. The poles in p^- are located at

$$p^{-} - k^{-} = \frac{(\mathbf{p}_{T} - \mathbf{k}_{T})^{2} + M^{2} - i0}{p^{+} - k^{+}}, \qquad (5.26)$$

$$p^{-} = \frac{p_T^2 + M^2 - i0}{p^{+}}. (5.27)$$

The integral is nonzero only if they lie on opposite sides of the real axis, which requires $k^+ > |p^+|$. In terms of the variable

$$z = p^+/k^+,$$
 (5.28)

which measures the fraction of the pair's light–cone momentum carried by the quark, cf. Eq. (5.24), this condition implies |z| < 1. Because x > 0 we can limit ourselves to z > 0, and thus 0 < z < 1. We close the contour around the pole Eq. (5.26) in the upper half plane. At the pole, the virtuality of the active quark is

$$p^{2} - M^{2} \equiv t - M^{2}$$

$$= -\frac{1}{\bar{z}} [(\mathbf{p}_{T} - z\mathbf{k}_{T})^{2} + M^{2} - z\bar{z}k^{2}], \quad (5.29)$$

where we have used that $k^+k^- = k^2 + k_T^2$. The integral in Eq. (5.18) then becomes

$$f_{q\bar{q}}(x, y; \mathbf{p}_T, \mathbf{k}_T) = \frac{2N_c M^2}{(2\pi)^3 F_\pi^2} \frac{\Theta(z)\Theta(\bar{z})}{\bar{z}} \times \left[\frac{1}{M^2 - t} + \frac{zk^2}{(M^2 - t)^2} \right]. \quad (5.30)$$

We can equivalently express the quark–antiquark momentum distribution in terms of the variables of light–front time–ordered perturbation theory (see Fig. 7b). In this approach light–front 3–momenta (i.e., the plus and transverse components of the 4–momentum) are conserved and intermediate particles are on mass shell, but the light–front energy (i.e., the minus component of the 4–momentum) of the intermediate state is generally different from that of the initial state, resulting in nonconservation of 4–momentum. With the $(+,-,\perp)$ components of the 4–momenta of the quark and antiquark given by

$$p_1 = \left(zk^+, \frac{p_T^2 + M^2}{zk^+}, p_T\right),$$
 (5.31)

$$p_2 = \left(\bar{z}k^+, \frac{(p_T - k_T)^2 + M^2}{\bar{z}k^+}, k_T - p_T\right), \quad (5.32)$$

the invariant mass of the quark-antiquark pair is

$$s \equiv (p_1 + p_2)^2$$

$$= \frac{(\mathbf{p}_T - z\mathbf{k}_T)^2 + M^2}{z\bar{z}}.$$
 (5.33)

This corresponds to the invariant mass of a pair with zero overall transverse momentum, subjected to a transverse boost by k_T . Thus, we find the following simple relation between the active quark virtuality in the invariant approach and the invariant mass difference in the time–ordered approach:

$$t - M^2 = -z(s - k^2). (5.34)$$

The quark–antiquark distribution Eq. (5.30) then takes the form

$$f_{q\bar{q}}(x,y;\boldsymbol{p}_{T},\boldsymbol{k}_{T}) = \frac{2N_{c}M^{2}}{(2\pi)^{3}F_{\pi}^{2}} \frac{\Theta(z)\Theta(\bar{z})}{z\bar{z}}$$

$$\times \left[\frac{1}{s-k^{2}} + \frac{k^{2}}{(s-k^{2})^{2}} \right]$$

$$= \frac{2N_{c}M^{2}}{(2\pi)^{3}F_{\pi}^{2}} \frac{\Theta(z)\Theta(\bar{z})}{z\bar{z}} \frac{s}{(s-k^{2})^{2}}. (5.35)$$

In the collinear approximation Eq. (5.23), if we neglect the overall transverse momentum k_T and the virtuality k^2 according to Eqs. (5.19)–(5.20), the quark–antiquark momentum distribution becomes

$$f_{q\bar{q}}(z, p_T) = \frac{2N_c M^2}{(2\pi)^3 F_{\pi}^2} \frac{\Theta(z)\Theta(\bar{z})}{p_T^2 + M^2}.$$
 (5.36)

This result has several interesting features. First, the transverse momentum distribution in the pair exhibits a power–like "tail" at large values,

$$f_{q\bar{q}}(z, p_T) \sim \frac{2N_c M^2}{(2\pi)^3 F_\pi^2} \frac{\Theta(z)\Theta(\bar{z})}{p_T^2} \qquad (p_T^2 \gg M^2).$$
 (5.37)

Through Eq. (5.21) it produces a similar tail in the nucleon's sea quark transverse momentum distribution; this feature will be discussed in detail in Sec. V E below. Second, the $\sim 1/p_T^2$ tail results in a would–be logarithmic divergence of the quark–antiquark density in the pair when integrated over p_T up to the cutoff scale. The coefficient of this logarithmic divergence is the same as that of the logarithmic divergence of F_π^2 in the effective theory,

$$F_{\pi}^{2} \sim \frac{N_{c}M^{2}}{(2\pi)^{2}} \log \frac{\Lambda^{2}}{M^{2}} \qquad (\Lambda^{2} \gg M^{2}). \quad (5.38)$$

As a consequence, in the limit $\Lambda \to \infty$ the quark–antiquark distribution in the pair is normalized such that

$$\int_{\Lambda^2} d^2 p_T \, f_{q\bar{q}}(z, p_T) = 1 \qquad (\Lambda^2 \to \infty). \quad (5.39)$$

We shall require that this condition be satisfied also for finite values of the cutoff when we introduce the UV regularization in Sec. V F.

We note that in Eq. (5.36) the quark-antiquark momentum distribution in the pair is actually independent of the momentum fraction z. This is because at this level of approximation there is no restriction on the constituent quarks' virtuality or invariant mass. A nontrivial z-dependence of the distribution will appear when a cutoff is introduced.

E. Power-like tail at large momenta

Through the convolution formula of Eq. (5.21) the $1/p_T^2$ tail in the momentum distribution of the quark—antiquark pair, Eq. (5.37), causes a similar behavior in the nucleon's sea quark transverse momentum distribution:

$$f_{1,\text{grad}}^{\bar{u}+\bar{d}}(x,p_T) \sim \frac{C_{f_1}^{\bar{u}+\bar{d}}(x)}{p_T^2} \qquad (p_T^2 \gg M^2), \quad (5.40)$$

$$C_{f_1}^{\bar{u}+\bar{d}}(x) = \frac{2N_c M^2}{(2\pi)^3 F_{\pi}^2} \int_x^{\infty} \frac{dy}{y} f_{\rm cl}(y).$$
 (5.41)

The p_T distribution of sea quarks thus has a power–like behavior at momenta $p_T^2 \gg M^2$. This fact is of central importance and implies that the distribution of sea quarks is qualitatively different from that of valence quarks (see Sec. IV). It is a direct consequence of dynamical chiral symmetry breaking and shows the imprint of the QCD vacuum on the nucleon's partonic structure. Note that the coefficient of the tail is determined by the effective chiral dynamics at the scale $\sim M$ and can be computed without explicit reference to the UV cutoff of the effective theory. In fact, the ratio M/F_{π} appearing in Eqs. (5.37) and (5.41) is just the coupling constant of the massive constituent quarks to the chiral field, as it follows from expanding the effective interaction Eq. (2.1), cf. Sec. II A. A corresponding interpretation of the tail as due to quark-antiquark pairs created by the classical chiral field will be developed in Sec. VI.

Parametrically, the power–like tail in the sea quark p_T distribution extends up to the UV cutoff scale Λ^2 . It is interesting to note that the coefficient of the tail related to the would–be logarithmic divergence of the p_T –integrated parton density and can be recovered as the derivative of the p_T –integrated parton density with respect to the upper limit of the p_T integral, in formal analogy to the relation for the unintegrated parton density in perturbative QCD, Eqs. (1.2) and (1.3). In fact, the coefficient Eq. (5.41) is nothing but the p_T integrated parton density in gradient expansion,

$$C_{f_1}^{\bar{u}+\bar{d}}(x) = f_{1,\text{grad}}^{\bar{u}+\bar{d}}(x).$$
 (5.42)

However, we caution that Eqs. (5.40)–(5.42) apply with logarithmic accuracy only, and that the numerical values of the p_T distribution for finite cutoff are strongly affected by the cutoff. In Sec. VF we formulate the physical conditions under which the UV regularization should

be implemented. and show that the high–momentum tail of the sea quark distribution — albeit in numerically modified form — is indeed a robust feature of the model.

F. Implementation of ultraviolet cutoff

To proceed further with our study of sea quark transverse momentum distributions we now have to discuss the implementation of the UV cutoff of the model and its effect on the distributions. This will allow us not only to evaluate the distributions quantitatively, but also to integrate them over p_T and relate them to the total parton densities. To study the effects of the UV cutoff we use the gradient expansion in the collinear approximation, Eq. (5.21), which captures the leading behavior of the unregularized distributions at large p_T and allows us to illustrate the essential points in analytic form.

As explained in Sec. I, the manner in which the cutoff is implemented *defines* the effective degrees of freedom of the model and must be based on physical considerations going beyond the intrinsic structure of the effective chiral theory. Here we *require* that the regularization procedure satisfy the following conditions:

I) The regularized distribution should preserve the symmetry of quarks and antiquarks in the pair:

$$f_{q\bar{q}}(z, p_T)_{\text{reg}} = f_{q\bar{q}}(\bar{z}, p_T)_{\text{reg}}.$$
 (5.43)

Exchange of quark and antiquark amounts to exchanging $z \to \bar{z} = 1 - z$ and $p_T \to -p_T$; because the unpolarized distribution is a function only of $p_T \equiv |p_T|$ the latter change is trivial.

II) The regularized distribution should be normalized such that the total number of quarks and antiquarks in the pair is unity, and that they carry the entire longitudinal momentum of the chiral field. This implies that the p_T -integrated distribution

$$f_{q\bar{q}}(z)_{\text{reg}} \equiv \int d^2p_T f_{q\bar{q}}(z, p_T)_{\text{reg}}$$
 (5.44)

satisfy

$$\int_{0}^{1} dz \ f_{q\bar{q}}(z)_{\text{reg}} = 1, \qquad (5.45)$$
$$\int_{0}^{1} dz \ z \ f_{q\bar{q}}(z)_{\text{reg}} = \frac{1}{2}. \qquad (5.46)$$

Because of the symmetry with respect to $z \rightarrow 1-z$ the two requirements are actually identical. Namely,

$$\int_{0}^{1} dz \ z \ f_{q\bar{q}}(z)_{\text{reg}} = \int_{0}^{1} dz \ \bar{z} \ f_{q\bar{q}}(z)_{\text{reg}}$$

$$= \frac{1}{2} \int_{0}^{1} dz \ (z + \bar{z}) \ f_{q\bar{q}}(z)_{\text{reg}}$$

$$= \frac{1}{2} \int_{0}^{1} dz \ f_{q\bar{q}}(z)_{\text{reg}}. \tag{5.47}$$

Physically, these conditions imply that the massive quarks and antiquarks are the only constituents of the nucleon's light–front wave function up to the cutoff scale, and that there is no momentum "hidden" in other degrees of freedom.

III) The regularization should not change the large-distance behavior of the quark field correlator in coordinate space. This requirement will be discussed in detail in Sec. V G, and implies that the cutoff should not modify the analytic properties of the p_T distribution in the vicinity of the leading singularity in p_T at complex values of the order M, which governs the fall-off at large distances. In the collinear approximation this is the pole at $p_T^2 = -M^2$ in Eq. (5.36).

The above represents a minimal set of physical requirements based on our present understanding; they may be amended by further conditions if more insights into the nature of the effective degrees of freedom were gained in the future. In the following we explore to what extent these minimal requirements determine the sea quark p_T distributions quantitatively. We first present two regularization schemes that meet these requirements.

 $Pauli-Villars\ subtraction.$ In the Pauli-Villars (PV) regularization scheme [32, 33] one subtracts from the original distribution of pointlike quarks with mass M a certain multiple of the analogous distribution of quarks with a regulator mass $M_{\rm PV} > M$,

$$f_{q\bar{q}}(z, p_T)_{PV} \equiv f_{q\bar{q}}(z, p_T | M)$$

- $\frac{M^2}{M_{PV}^2} f_{q\bar{q}}(z, p_T | M_{PV}).$ (5.48)

The coefficient is chosen such that the subtraction cancels the logarithmic divergence associated with the integral over p_T . Applying this subtraction to Eq. (5.36) we get

$$f_{q\bar{q}}(z, p_T)_{PV} = \frac{2N_c M^2}{(2\pi)^3 F_{\pi}^2} \Theta(z) \Theta(\bar{z}) \times \frac{M_{PV}^2 - M^2}{(p_T^2 + M^2)(p_T^2 + M_{PV}^2)}.$$
 (5.49)

The regularized distribution drops as $\sim 1/p_T^4$ at $p_T \to \infty$ and is integrable. At the same time, we replace F_π^2 in the normalization factor by the result obtained with PV regularization,

$$F_{\pi}^{2} = \frac{N_{c}M^{2}}{(2\pi)^{2}} \log \frac{M_{PV}^{2}}{M^{2}}.$$
 (5.50)

One can easily verify that with this normalization the conditions Eqs. (5.45) and (5.46) are satisfied, and that

$$f_{q\bar{q}}(z)_{\text{PV}} \equiv \int d^2p_T f_{q\bar{q}}(z, p_T)_{\text{PV}} = 1.$$
 (5.51)

Note also that the subtraction does not change the residue of the pole at $p_T^2=-M^2;$ i.e., Eq. (5.49) has

the same behavior near $p_T^2 \to -M^2$ as the unregularized expression Eq. (5.36). The numerical value of the regulator mass is fixed by requiring that Eq. (5.50) reproduce the physical value of the pion decay constant, $F_{\pi} = 93 \,\mathrm{MeV}$. One obtains

$$M_{\rm PV}^2/M^2 = 2.52$$
 $(M = 0.35 \,\text{GeV}).$ (5.52)

Invariant mass cutoff. Another way of implementing the cutoff is to limit the invariant mass of the quarkantiquark pair in the time-ordered approach, Eq. (5.33) (see Fig. 7b). In the collinear approximation the invariant mass Eq. (5.33) is given by

$$s = \frac{p_T^2 + M^2}{z\bar{z}} > 0. {(5.53)}$$

The cutoff is implemented by multiplying the vertices of the quark-antiquark pairs in the initial and final state with a form factor F(s) that suppresses invariant masses of the order $s \sim \Lambda^2$. We consider a monopole and an exponential form factor,

$$F(s)_{\text{mon}} = \frac{1}{1 + s/\Lambda^2},$$
 (5.54)

$$F(s)_{\text{exp}} = \exp(-s/\Lambda^2). \tag{5.55}$$

The form factor is normalized to unity at the unphysical point s=0, which corresponds to $p_T^2=-M^2$; the significance of this choice will be explained in Sec. VG. The regularized quark/antiquark distribution is then given by

$$f_{q\bar{q}}(z, p_T)_{\text{inv}} \equiv f_{q\bar{q}}(z, p_T) F^2(s)$$

$$= \frac{2N_c M^2}{(2\pi)^3 F_{\pi}^2} \frac{\Theta(z)\Theta(\bar{z}) F^2(s)}{p_T^2 + M^2}. (5.56)$$

The normalization condition now takes the form

$$\frac{2N_c M^2}{(2\pi)^3 F_\pi^2} \int_0^1 dz \int d^2 p_T \frac{F^2(s)}{p_T^2 + M^2} = 1.$$
 (5.57)

The value of Λ^2 is fixed such that Eq. (5.57) is satisfied with the physical value of F_{π}^2 . For $M=0.35\,\mathrm{GeV}$ this

$$\Lambda_{\text{mon}}^2 = 31.1 \, M^2 = 7.78 \times 4 M^2,$$
 $\Lambda_{\text{exp}}^2 = 44.8 \, M^2 = 11.2 \times 4 M^2.$
(5.59)

$$\Lambda_{\text{exp}}^2 = 44.8 \, M^2 = 11.2 \times 4M^2.$$
 (5.59)

The latter values are given as multiples of the minimum value of s in the physical region, $4M^2$. Figure 10a shows the effective z-distribution obtained with an invariant mass cutoff (exponential form factor) for several values of p_T ; for the sake of comparison all distributions were normalized to unit integral over z. One sees that the z-distribution is rather flat for $p_T = 0$ and becomes progressively more concentrated around z = 1/2 as p_T in-

The p_T -integrated distributions in the quark-antiquark pair, Eq. (5.44), obtained with the two regularization schemes, are shown in Fig. 10b. Several features are

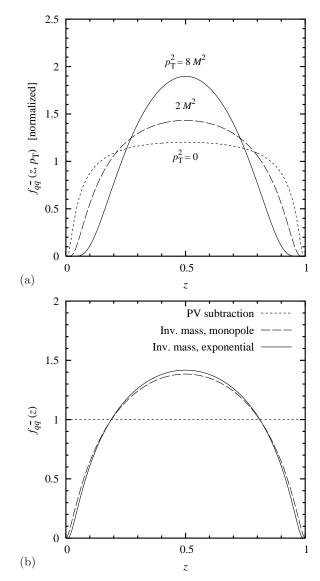


FIG. 10. (a) Quark-antiquark light-cone momentum distribution $f_{q\bar{q}}(z, p_T)$ as function of z for fixed p_T [exponential invariant mass cutoff, Eq. (5.55)]. The values of p_T^2 are indicated above/below the curves. For the sake of comparison the distributions at all values of p_T^2 were normalized to unit integral over z. (b) The p_T -integrated quark-antiquark lightcone momentum distribution $f_{q\bar{q}}(z)$, Eq. (5.44), with different UV cutoffs. Dotted line: PV subtraction. Dashed line: Invariant mass cutoff by monopole form factor, Eq. (5.54). Solid line: Invariant mass cutoff by exponential form factor, Eq. (5.55).

worth noting: (a) The light-cone momentum distribution obtained with the PV cutoff is independent of z and given by $f_{q\bar{q}}(z) = 1$. In the context of the convolution integral, Eq. (5.21), this turns out to be a reasonable approximation for x that are not parametrically small (see below). (b) The light-cone momentum distribution obtained with the invariant mass cutoff vanishes at the end points $z \to 0, 1$. In the convolution integral Eq. (5.21),

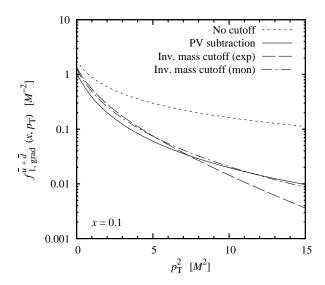


FIG. 11. Sea quark transverse momentum distribution $f_{1,\mathrm{grad}}^{\bar{u}+\bar{d}}(x,p_T)$ calculated using the gradient expansion in collinear approximation, Eq. (5.21), as a function of p_T^2 , at x=0.1. Shown are the distributions obtained with various UV cutoff schemes (see text). Both p_T and $f_{1,\mathrm{grad}}^{\bar{u}+\bar{d}}$ are given in units of the constituent quark mass M. Dotted line: Unregularized distribution (no UV cutoff). Solid line: PV subtraction. Dashed line: Invariant mass cutoff, exponential form. Dash-dotted line: Invariant mass cutoff, monopole form. [Self-consistent soliton profile Eq. (A4) with $M=0.35\,\mathrm{GeV}$ and $M_N=3.26\,M.$]

because $f_{\rm cl}(y)/y$ is finite in the limit $y \to 0$, the vanishing of $f_{q\bar q}(z)$ at $z \to 0$ ensures that $f(x,p_T) \to 0$ for $x \to 0$, i.e., the sea quark density in the nucleon vanishes at $x \to 0$. (c) With both cutoff schemes the convolution integral for the sea quark transverse momentum distribution Eq. (5.21) involves a broad distribution of quark momentum fractions centered around $z \sim 1/2$, at least for non–exceptional values of x.

With all the ingredients in place, we can now calculate the sea quark transverse momentum distributions for a finite cutoff and study their dependence on the UV regularization. We use the gradient expansion in the collinear approximation, Eq. (5.21), with the light-cone momentum distribution of the chiral field given by Eq. (5.22) and evaluated with the soliton profile of Eqs. (A4)–(A7) [cf. Fig. 9]. The p_T distribution in the quark–antiquark pair is now given by the regularized expressions Eq. (5.49) or Eq. (5.56). The numerical results for the p_T distributions at a representative value of x = 0.1 are summarized in Fig. 11. The p_T -distribution without cutoff (or, what is the same, in the limit of infinite cutoff), as obtained from the unregularized quark-antiquark distribution Eq. (5.36), is shown by the short-dashed line; this distribution is not integrable over p_T and shown for comparison only. The distributions obtained with the PV cutoff and the invariant mass cutoff (exponential and monopole form factor) are shown by the solid, longdashed, and dash–dotted lines. The results show several notable features. First, the distributions with any UV cutoff differ from the one without cutoff already at low values $p_T^2 \sim \text{few } M^2$. It shows that the cutoff plays an essential role in the numerical value of the p_T distribution already at low p_T . This fact is not obvious from parametric considerations based on the hierarchy $\Lambda \gg M$, as the distributions at fixed p_T are UV finite and thus do not "require" regularization.

Second, the distributions obtained with PV subtraction and the invariant mass cutoff (exponential and monopole) are very close up to values $p_T^2 \approx 10\,M^2$. In this region of p_T they are determined by generic features of the cutoff as are fixed by our general conditions. This finding is very important, as it means that the p_T distributions in this range are robust predictions of the model and can be discussed at the same level as other lowenergy characteristics of the nucleon.

Third, at $p_T^2 \gtrsim 10\,M^2$ the distributions obtained with the different cutoffs show large differences, as expected. One important implication of this is that the averages $\langle p_T^2 \rangle$ differ substantially and do not serve as reliable measures of the width of the bulk of the p_T distribution. These averages assign disproportionate weight to the high– p_T region where the distributions are not constrained by our requirements on the cutoff.

G. Quark field correlator in coordinate space

Further insight into the role of the UV cutoff in the sea quark transverse momentum distributions can be gained by studying the corresponding coordinate—space correlation functions (cf. Sec. III E). The essential points can again be illustrated using the gradient expansion in the collinear approximation, Eq. (5.21). In this approximation the coordinate—space correlation function of sea quarks, Eq. (3.54), is given by the transverse Fourier transform of the convolution formula, Eq. (5.21),

$$\tilde{f}_1^{\bar{u}+\bar{d}}(x,\xi_T) = \int_x^\infty \frac{dy}{y} f_{cl}(y) \, \tilde{f}_{q\bar{q}}(x/y,\xi_T),$$
 (5.60)

where $f_{q\bar{q}}(z, \xi_T)$ ($z \equiv x/y$) is the transverse Fourier transform of the p_T distribution in the quark–antiquark pair,

$$\tilde{f}_{q\bar{q}}(z,\xi_T) \equiv \int d^2 p_T \ e^{-i\mathbf{p}_T \xi_T} \ \tilde{f}_{q\bar{q}}(z,\xi_T)
= 2\pi \int_0^\infty dp_T \ p_T \ J_0(p_T \xi_T) \ \tilde{f}_{q\bar{q}}(z,p_T).$$
(5.61)

This function describes the spatial structure of the quark—antiquark pairs created by the chiral field. It is interesting to see how it behaves at small and large distances, and how its behavior is modified by the UV cutoff of the model. In particular, the behavior at large distances sheds new light on the regularization conditions put forward in Sec. V F.

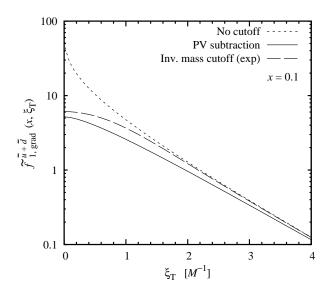


FIG. 12. Coordinate—space correlator $\tilde{f}_{1,\mathrm{grad}}^{\bar{u}+\bar{d}}(x,\xi_T)$, corresponding to the gradient expansion of the sea quark distribution in collinear approximation, Eq. (5.60), as a function of ξ_T , at x=0.1. Dotted line: No cutoff. Dashed line: PV subtraction. Solid line: Invariant mass cutoff (exponential). [Self–consistent soliton profile Eq. (A4) with $M_\pi=0$, $M=0.35\,\mathrm{GeV}, M_N=3.26\,M.$]

Without a cutoff, i.e., with the distribution Eq. (5.36), the Fourier transform of the p_T distribution in the $q\bar{q}$ pair is given by

$$\tilde{f}_{q\bar{q}}(z,\xi_T) = 2\pi K_0(M\xi_T).$$
 (5.62)

At $\xi_T \to 0$ this function diverges logarithmically,

$$\tilde{f}_{q\bar{q}}(z,\xi_T) \sim 2\pi \log \frac{1}{M\xi_T}$$
 $(\xi_T \to 0)$, (5.63)

which reflects the logarithmic divergence of the total (p_T integrated) parton density in the model without cutoff.
With a cutoff this divergence is regularized. For example,
with the PV subtraction the distribution becomes

$$\tilde{f}_{q\bar{q}}(z,\xi_T)_{PV} = 2\pi \left[K_0(M\xi_T) - K_0(M_{PV}\xi_T) \right]$$

$$\sim 2\pi \log \frac{M_{PV}}{M} \qquad (\xi_T \to 0). \tag{5.64}$$

A similar result is obtained with the invariant mass cutoff. Thus we see that at small distances the behavior of the correlation function is qualitatively changed by the cutoff, in accordance with the fact that the function at $\xi_T=0$ coincides with the total parton density

At large distances the ξ_T correlation in the $q\bar{q}$ pair decays exponentially,

$$\tilde{f}_{q\bar{q}}(z,\xi_T) \sim 2\pi \ [\pi/(2M\xi_T)]^{1/2} \times \exp(-M\xi_T) \quad (\xi_T \to \infty),$$
 (5.65)

with a range determined by the constituent quark mass M. This appears natural, as the constituent quark mass

represents the "mass gap" of the effective chiral model and controls the long-distance behavior of quark correlations. Since it reflects a low-energy property of our model we should require that the UV cutoff do not modify this behavior. The exponential fall-off at large distances is related to the singularity of the unregularized p_T distribution at $p_T^2 = -M^2$, corresponding to complex values of p_T . Our requirement therefore implies that the cutoff should not modify this free-field singularity. It is easy to see that the schemes discussed in Sec. VF satisfy this requirement. PV subtraction leaves the residue of the pole at $p_T^2 = -M^2$ unchanged, cf. Eq. (5.49). Likewise, with the invariant mass cutoff the residue remains unchanged because the invariant mass vanishes at the pole, $s \to 0$, and the form factors are normalized such that F(s = 0) = 1, cf. Eq. (5.56). This explains the physical basis of regularization condition III presented in Sec. VF.

The quark field correlator $\tilde{f}_1^{\bar{u}+\bar{d}}(x,\xi_T)$ in the nucleon obtained from Eq. (5.60) is presented in Fig. 12. The plot shows the ξ_T dependence of the correlation function at a representative value of x = 0.1. The following features are worth noting: (a) The regularized distributions rapidly approach exponential behavior at $\xi_T \sim \text{few } M^{-1}$, as implied by Eq. (5.65). (b) The distributions obtained with the PV and invariant mass cutoffs are overall rather close at all distances. This explains the approximate cutoff-independence of the p_T -distributions at low p_T observed in Sec. VF (see Fig. 11). We note that the results would be even closer if we required that the different regularizations reproduce the same total parton density, e.g. by adjusting the cutoff values, or by performing a second PV subtraction. (c) The curvature of the ξ_T distributions at $\xi_T = 0$, which is proportional to $\langle p_T^2 \rangle$, is not effectively constrained and can thus vary considerably between different regularization schemes. This reaffirms our earlier conclusion regarding the model dependence of $\langle p_T^2 \rangle$.

In sum, we find that the combined requirements of matching the parton density at $\xi_T=0$ and decaying exponentially at $\xi_T\to\infty$ effectively constrain the correlator at all distances. The Fourier transform of these correlators results in stable, cutoff–independent p_T –distribution at low p_T as seen in Fig. 11. The study of the coordinate–space correlation function of sea quarks thus reaffirms our conclusion that the physical regularization conditions presented in Sec. VF result in robust transverse momentum distributions at low p_T .

Our aim in this section was to investigate the influence of the UV cutoff on the coordinate—space distribution, which could be done in a simple way with the gradient expansion in collinear approximation, Eq. (5.21). In this approximation the information about the finite spatial size of the classical chiral field is lost, and the exponential decay of the correlator at large ξ_T is due entirely to the intrinsic size of the quark—antiquark pair. To study the "true" large—distance behavior of the sea quark correlator in the nucleon one should use the full gradient

expansion result, Eq. (5.16), in which the finite size of the chiral field is encoded in the k_T dependence. Numerical studies show that also in the full correlation function the large- ξ_T behavior is independent of the UV cutoff; i.e., our conclusions are general and do not depend on the additional simplifications made in Eq. (5.21).

H. Numerical evaluation

Having established the behavior of the sea quark transverse momentum distribution at large momenta $p_T^2 \gg M^2$ and the role of the UV cutoff, we now want to make a numerical estimate of the distributions also at lower momenta $p_T^2 \sim \text{few } M^2$. This will allow us to compare the sea quark transverse momentum distribution with those of the valence quarks at a quantitative level (see Sec. VI).

In its representation as a sum over occupied quark single-particle levels, Eq. (3.32), the sea quark distribution receives contributions both from the negative-energy Dirac continuum and the discrete bound-state level. The gradient expansion approximates the contribution from the Dirac continuum, i.e., quark scattering states distorted by the classical chiral field, which dominates at momenta $p_T^2 \gg M^2$. The contribution from the discrete bound-state level with its normalizable wave function is not contained in the expanded Green function. At lower momenta $p_T^2 \sim \text{few } M^2$, as well as in the integral over p_T , the contribution of the discrete level becomes numerically relevant. A more accurate approximation in this region for numerical purposes is obtained by adding to the leading-order gradient expansion Eq. (5.21) the contribution from the discrete bound-state level given by Eq. (4.2),

$$f_1^{\bar{u}+\bar{d}}(x,p_T) \approx f_{1,\mathrm{grad}}^{\bar{u}+\bar{d}}(x,p_T) + f_{1,\mathrm{lev}}^{\bar{u}+\bar{d}}(x,p_T).$$
 (5.66)

This approximation is known as the "interpolation formula," as it becomes exact both in the limit of large soliton size, where the gradient expansion is parametrically justified and the discrete level energy becomes negative, and in the limit of small soliton size, where the level contribution dominates [32]. Numerical studies show that Eq. (5.66) reproduces the exact numerical result for the p_T -integrated sea quark distribution [56] with an accuracy of far better than 20% for x=0.1-0.5 when evaluated with the self-consistent soliton profile Eqs. (A4)–(A7). We therefore expect it to provide a reasonable approximation also for the p_T distributions at $p_T^2 \sim \text{few } M^2$.

Figure 13 shows the different contributions to the sea quark distribution in Eq. (5.66) at a representative value of x=0.1 (note that the level contribution is negative and shown with opposite sign in the figure). One sees that the gradient expansion contribution approximating the Dirac continuum clearly dominates at large p_T ; the level contribution to the total $f_1^{\bar{u}+\bar{d}}$ is <20%

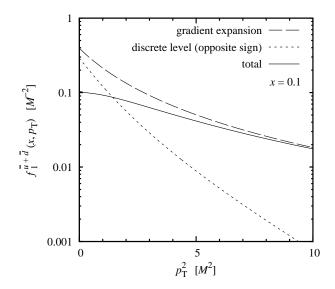


FIG. 13. Numerical approximation for the sea quark transverse momentum distribution $f_1^{\bar{u}+\bar{d}}(x,p_T)$, Eq. (5.66) ("interpolation formula"). Dashed line: Gradient expansion $f_{1,\mathrm{grad}}^{\bar{u}+\bar{d}}(x,p_T)$, Eq. (5.21), approximating the Dirac continuum contribution in Eq. (3.32) (PV regularization). Dotted line: Contribution from the discrete bound–state level, $f_{1,\mathrm{lev}}^{\bar{u}+\bar{d}}(x,p_T)$ Eq. (4.2), shown with opposite sign. Solid line: Total distribution according to Eq. (5.66). [Self–consistent soliton profile Eq. (A4) with $M=0.35~\mathrm{GeV}, M_N=3.26~M.$]

above $p_T^2 = 5 M^2$ and decreases rapidly at larger p_T . This justifies our earlier use of the gradient expansion to study the large- p_T behavior. At low p_T there are very significant cancellations between the gradient expansion and the discrete level contribution, causing the sum to be 3-4 times smaller than the individual terms. Since the gradient expansion provides only a rough approximation to the Dirac continuum at low p_T (cf. Fig. 8, which compares different variants), and is subject to some uncertainty resulting from the UV cutoff, we cannot use Eq. (5.66) to predict the total $f_1^{\bar{u}+\bar{d}}$ with any meaningful relative accuracy at low p_T , but can conclude only that it is substantially smaller than the gradient expansion result alone. More quantitatively, if we require that the level contribution be < 50% of the gradient expansion we conclude that we can safely use Eq. (5.66) for a numerical estimate at $p_T^2 > 2 M^2$. At lower values of p_T one should use methods based on exact summation over levels to calculate the sea quark transverse momentum distribution [40]. Note, however, that the contribution of this region to the p_T -integral determining the total sea quark density is rather small (see below), so that the question of the exact behavior of the sea quark p_T distribution in this region is somewhat academic.

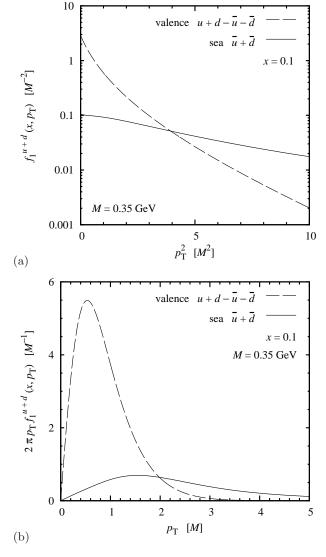


FIG. 14. Transverse momentum distributions of flavor–singlet unpolarized valence and sea quarks at x=0.1. Panel (a) shows $f_1^{u+d-\bar{u}-\bar{d}}$ and $f_1^{\bar{u}+\bar{d}}$ as functions of p_T^2 on a logarithmic scale; panel (b) shows the radial distribution $2\pi p_T f_1^{u+d-\bar{u}-\bar{d}}$ and $2\pi p_T f_1^{\bar{u}+\bar{d}}$ on a linear scale, such that the area under the curves corresponds to the integral over p_T . Dashed lines: Valence quark distribution $f_1^{u+d-\bar{u}-\bar{d}}$ (see Fig. 6). Solid lines: Sea quark distribution $f_1^{\bar{u}+\bar{d}}$ (PV regularization). [Selfconsistent soliton profile Eq. (A4) with $M=0.35\,\mathrm{GeV}, M_N=3.26\,M.$]

I. Sea vs. valence quark distribution

Using the numerical approximation of Sec. V H we now want to compare our results for the sea quark transverse momentum distribution with those of the valence quarks calculated in Sec. IV. Figure 14 summarizes the numerical results for the valence distribution $f_1^{u+d-\bar{u}-\bar{d}}(x,p_T)$ and the sea quark distribution $f_1^{\bar{u}+\bar{d}}(x,p_T)$ at a representative value of x=0.1. Panel (a) shows the distributions

themselves on a logarithmic scale; panel (b) the radial distributions on a linear scale, such that the area under the curves corresponds directly to their integral over p_T . Similar results are obtained at other values of x: the shape of the individual p_T distribution changes little with x (cf. Fig. 4 for the valence distribution); only their normalization changes in proportion to the total valence and sea quark density.

The numerical estimates clearly show very different shapes of the valence and sea quark transverse momentum distributions, especially at large values of p_T , as first observed in the calculation of Ref. [40]. Based on our theoretical analysis we can now explain this striking behavior as the effect of dynamical chiral symmetry breaking in the QCD vacuum on the intrinsic transverse momentum distribution of the sea quarks. Even with the strong modification of the would-be $1/p_T^2$ tail by the UV cutoff, the sea quark transverse momentum distribution in the chiral quark-soliton model is qualitatively different from that of the valence quarks. While the precise numerical values depend on the model implementation (see e.g. Fig. 11), the fact as such is rooted in the basic structure of the effective dynamics chiral and should be model-independent.

When interpreting the results of Figure 14 one should keep in mind that the accuracy of the approximation Eq. (5.66) used in our numerical estimate of $f_1^{\bar{u}+\bar{d}}(x,p_T)$ is not sufficient to predict the values at $p_T^2\lesssim 2\,M^2$ with meaningful relative accuracy (cf. the discussion in Sec. V H). In this sense the plot of the radial distribution, in which the low- p_T region is suppressed, conveys a more realistic picture. This uncertainty, however, in no way influences our conclusions regarding the qualitatively different behavior of valence and sea quark distributions at large p_T .

The qualitative difference between the p_T distribution of valence and sea quarks is the most important practical result of our study. Its numerous implications for deep—inelastic processes are explored in Sec. VIII.

J. Polarized sea quark distribution

To complete our study of the sea quark transverse momentum distribution we want to investigate also the flavor–nonsinglet polarized sea quark distribution. The gradient expansion of this distribution can be carried out in complete analogy to the flavor–singlet unpolarized case starting from Eq. (3.38), cf. Secs. V A and V B; we do not present the intermediate steps here. The result can again be represented as a convolution integral over the momentum of the classical chiral field, analogous to Eq. (5.16),

$$g_{1,\text{grad}}^{\bar{u}-\bar{d}}(x,p_T) = \int \frac{dy}{y} \int d^2k_T \ g_{\text{cl}}(y,\mathbf{k}_T)$$
$$\times g_{q\bar{q}}(x,y;\mathbf{p}_T,\mathbf{k}_T). \tag{5.67}$$

The relevant momentum distribution of the classical field is now

$$g_{\rm cl}(y, \mathbf{k}_T) \equiv \frac{F_{\pi}^2 M_N^2 y}{3(2\pi)^3} \operatorname{tr}_{\rm fl} \left[\tau^3 \widetilde{U}_{\rm cl}(\mathbf{k}) \widetilde{U}_{\rm cl}(\mathbf{k})^{\dagger} \right] \qquad (5.68)$$
$$\left[\mathbf{k} = (\mathbf{k}_T, y M_N) \right].$$

The momentum distribution resulting from the quark loop integral turns out to be the same as in the flavor singlet unpolarized case

$$g_{q\bar{q}}(x, y; \boldsymbol{p}_T, \boldsymbol{k}_T) = f_{q\bar{q}}(x, y; \boldsymbol{p}_T, \boldsymbol{k}_T)$$
 (5.69)

(for the p_T -integrated distributions this was already noted in Ref. [32]). This remarkable fact can be understood as an instance of "restoration of chiral symmetry." When expanding in gradients of the chiral fields the numerator of the quark loop integral becomes independent of the dynamical quark mass M, and the same coefficient is obtained for the axial vector—type operator in the polarized distribution (Dirac matrix $\gamma^+\gamma_5$) as for the vector—type operator in the unpolarized distribution (γ^+). A more microscopic interpretation of this result in terms of pair correlations in the nucleon wave function will be discussed below. Equation (5.69) has important consequences for the behavior of the flavor—nonsinglet polarized p_T distribution at large transverse momenta.

At transverse momenta $p_T^2 \gg M^2$ the convolution integral Eq. (5.68) can again be simplified by using the collinear approximation, Eqs. (5.19) and (5.20), and becomes

$$g_{1,\text{grad}}^{\bar{u}-\bar{d}}(x,p_T) = \int_x^\infty \frac{dy}{y} g_{\text{cl}}(y) g_{q\bar{q}}(x/y,p_T).$$
 (5.70)

Here $g_{cl}(y)$ is the corresponding k_T -integrated light-cone momentum distribution of the classical chiral field, cf. Eq. (5.22),

$$g_{\rm cl}(y) \equiv \int d^2k_T \ g_{\rm cl}(y, \boldsymbol{k}_T)$$

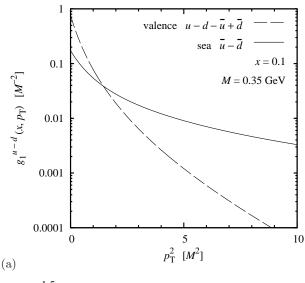
$$= \frac{F_\pi^2 M_N^2 y}{3(2\pi)} \int \frac{d^2k_T}{(2\pi)^2} \operatorname{tr}_{\rm fl}[\tau^3 \widetilde{U}_{\rm cl}(\boldsymbol{k}) \, \widetilde{U}_{\rm cl}(\boldsymbol{k})^{\dagger}] \quad (5.71)$$

$$(k^3 = y M_N),$$

which can be evaluated using Eq. (C6) in Appendix C. The numerical distribution is shown in Fig. 9. One sees that at $y \to 0$ the "polarized" distribution is suppressed relative to the "unpolarized" one, as expected, and that at large values of $y \sim 1$ the distributions approximately satisfy $3g_{\rm cl}(y) \approx f_{\rm cl}(y)$, corresponding to saturation of the large– N_c inequality for the transverse momentum densities (see below). The momentum distribution of the quark–antiquark pair appearing in Eq. (5.70) is the same as in the unpolarized case, cf. Eq. (5.69),

$$g_{q\bar{q}}(z, p_T) = f_{q\bar{q}}(z, p_T),$$
 (5.72)

where $z \equiv x/y$ and $f_{q\bar{q}}(z, p_T)$ is defined in Eq. (5.23) and explicitly given by Eq. (5.36), up to modifications by the



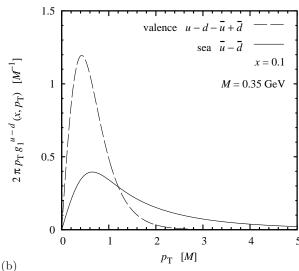


FIG. 15. Transverse momentum distributions of flavornonsinglet polarized valence and sea quarks at x=0.1. Panel (a) shows $g_1^{u-d-\bar{u}+\bar{d}}$ and $g_1^{\bar{u}-\bar{d}}$ as functions of p_T^2 on a logarithmic scale; panel (b) shows the radial distribution $2\pi p_T g_1^{u-d-\bar{u}+\bar{d}}$ and $2\pi p_T g_1^{\bar{u}-\bar{d}}$ on a linear scale, such that the area under the curves corresponds to the integral over p_T . Dashed lines: Valence quark distribution $g_1^{u-d-\bar{u}+\bar{d}}$ (see Fig. 6). Solid lines: Sea quark distribution $g_1^{\bar{u}-\bar{d}}$ (PV regularization). [Self-consistent soliton profile Eq. (A4) with $M=0.35\,\mathrm{GeV}, M_N=3.26\,M.$]

UV cutoff. As a result, the flavor–nonsinglet polarized distribution exhibits a would–be power–like tail at large transverse momenta similar to the unpolarized distribution,

$$g_1^{\bar{u}-\bar{d}}(x, p_T) \sim \frac{C_{g_1}^{\bar{u}-\bar{d}}(x)}{p_T^2} \qquad (p_T^2 \gg M^2).$$
 (5.73)

Moreover, the coefficient of this tail is related to the UV divergence of the p_T -integrated distribution in the

same way as in the unpolarized case, and is given by [cf. Eq. (5.42)]

$$C_{q_1}^{\bar{u}-\bar{d}}(x) = g_{1,\text{grad}}^{\bar{u}-\bar{d}}(x).$$
 (5.74)

Thus, our earlier discussion of the UV regularization and its effect on the transverse momentum distributions can be carried over directly to the polarized case.

For a numerical estimate of the flavor–nonsinglet polarized sea quark distribution at all values of p_T (including $p_T \sim M$) we use the analogue of the "interpolation formula" Eq. (5.66), in which one adds the contribution from the discrete bound–state level, Eq. (4.7), to the gradient expansion approximating the Dirac continuum contribution, Eq. (5.67),

$$g_1^{\bar{u}-\bar{d}}(x,p_T) \approx g_{1,\mathrm{grad}}^{\bar{u}-\bar{d}}(x,p_T) + g_{1,\mathrm{lev}}^{\bar{u}-\bar{d}}(x,p_T).$$
 (5.75)

The resulting polarized sea quark distribution is shown in Fig. 15 and compared to the valence quark distribution $g_1^{u-d-\bar{u}+\bar{d}}$ calculated in Sec. IV C. One sees that, as in the flavor–singlet unpolarized case, the would–be power–like tail strongly influences the numerical behavior of the flavor–nonsinglet polarized sea quark distribution at $p_T^2 > \text{few } M^2$ and causes it to be qualitatively different from that of the valence quarks. This again represents a direct effect of dynamical chiral symmetry breaking on the nucleon's partonic structure. Note that here the effect occurs in a nonsinglet channel, in which the distributions are likely to be much less affected by perturbative QCD evolution than in the singlet case, making this nonperturbative effect even more striking (cf. discussion in Sec. VII).

A more microscopic explanation for the similarity of the flavor-singlet unpolarized and flavor-nonsinglet polarized distributions at $p_T^2 \gg M^2$ is provided in Sec. VI, where we show that the tails in the sea quark distributions are due to correlated quark-antiquark pairs in the nucleon's light-cone wave function. The correlated pairs appear in scalar–isoscalar (Σ) and pseudoscalar–isovector (Π) quantum numbers. The flavor-singlet unpolarized sea results from the overlap of like pairs $(\Sigma\Sigma, \Pi\Pi)$, while the flavor-nonsinglet polarized one is due to the interference of different types of pairs $(\Sigma\Pi, \Pi\Sigma)$ in the initial and final state. At $p_T^2 \gg M^2$ the wave functions of the Σ and Π pairs become the same due to the restoration of chiral symmetry, Eq. (6.27), leading naturally to a relation between the two sea quark distributions. We note that this derivation of the flavor-nonsinglet polarized sea quark distribution gives a precise meaning to the notion of " $\Pi\Sigma$ interference," which was discussed in connection with the meson cloud model of flavor asymmetries in Ref. [65].

To conclude our discussion of the polarized sea quark distribution, we would like to see how the general large– N_c inequality for sea quark distributions, Eq. (3.52), is realized in our model. At $p_T^2 \gg M^2$ the distributions are given by the gradient expansion, in the simplified form of Eqs. (5.21) and (5.70), and we want to verify that

$$f_1^{\bar{u}+\bar{d}}(x,p_T) \pm 3 g_1^{\bar{u}-\bar{d}}(x,p_T) > 0$$
 (5.76)

in this approximation. Because of Eq. (5.72) the differences on the left–hand side of Eq. (5.76) can be written in the form

$$f_1^{\bar{u}+\bar{d}}(x,p_T) \pm 3 g_1^{\bar{u}-\bar{d}}(x,p_T)$$

$$= \int_x^\infty \frac{dy}{y} \left[f_{\text{cl}}(y) \pm 3 g_{\text{cl}}(y) \right] f_{q\bar{q}}(x/y,p_T), \quad (5.77)$$

where $f_{\bar{q}q}$ is explicitly positive; cf. the discussions in Secs. V D and V F and the representation of this function as light-cone wave function overlap derived in Sec. VI C, Eq.(6.35). The difference of the momentum distributions of the classical field in Eq. (5.77), in turn, is given by

$$f_{\rm cl}(y) \pm 3 g_{\rm cl}(y) = \frac{F_{\pi}^{2} M_{N}^{2} y}{(2\pi)} \int \frac{d^{2} k_{T}}{(2\pi)^{2}} \times \operatorname{tr}_{\rm fl}[(1 \pm \tau^{3}) \widetilde{U}_{\rm cl}(\mathbf{k}) \widetilde{U}_{\rm cl}(\mathbf{k})^{\dagger}] \quad (5.78)$$
$$(k^{3} = y M_{N}),$$

which is explicitly positive, cf. Eq. (C7) in Appendix C. Thus we see that the "restoration of chiral symmetry" expressed in Eq. (5.69) naturally guarantees that the large— N_c inequalities for the sea quark distributions are satisfied at $p_T^2 \gg M^2$ in our scheme of approximations.

The results of the interpolation formulas Eq. (5.66) and (5.75) for the distributions at $p_T^2 \sim M^2$, taken literally, would violate the inequality Eq. (5.76) at $p_T^2 \lesssim 2 M^2$. However, we noted in Sec. VH that in this region the unpolarized sea quark distribution cannot be estimated with any meaningful relative accuracy using this approximation. We therefore cannot conclusively study the inequality at low p_T using this approximation.

VI. SHORT-RANGE CORRELATIONS OF PARTONS

A. Nucleon wave function at large momenta

So far we studied the properties of valence and sea quarks in the nucleon by investigating their one-body momentum densities, Eqs. (3.2) and (3.3). A more microscopic understanding of our results can be obtained by considering the nucleon's partonic (or light-front) wave function in the chiral quark-soliton model. Specifically, we want to show that in this model sea quarks partly exist in correlated pairs of a size of the order of the cutoff scale $\Lambda^{-1} \ll R$, and that the "tail" in their transverse momentum density can directly be attributed to these configurations. That is, the two-scale picture of the effective dynamics resulting from chiral symmetry breaking implies the existence of short-range quark-antiquark correlations in the partonic wave function. This observation has far-reaching implications for our understanding of the partonic structure of the nucleon not only in the

chiral quark—soliton model but in QCD in general. It suggests an interesting analogy with short—range nucleon—nucleon correlations in nuclei, which give rise to high—momentum components of the nuclear spectral function governing single—particle knockout reactions and can be probed directly in multiparticle correlation experiments [44–46]. A detailed treatment of parton short—range correlations due to dynamical chiral symmetry breaking and their implications will be the subject of a subsequent publication. Here we want to discuss only the aspects relevant to understanding the behavior of the intrinsic transverse momentum distributions.

The light–front wave function of the nucleon in the chiral quark–soliton model was derived and discussed in a general context in Refs. [41, 42]. In this approach the many–body wave function of the fast–moving nucleon is constructed by applying the creation operators of N_c valence quarks and a coherent superposition of quark–antiquark pairs to the vacuum state of the effective chiral theory, i.e., the Dirac vacuum with baryon number zero. The construction can be carried out explicitly in the sense of a Fock state expansion, using the bound–state level occupied by N_c quarks as a seed [43]. Here we are interested in the sea quark component of the nucleon wave function at large transverse momenta,

$$p_T^2 \gg M^2. \tag{6.1}$$

This component of the wave function can be calculated directly in a simple approximation, assuming the existence of a stable mean field. It will be seen that this approximation is equivalent to the gradient expansion for the one—body momentum densities of sea quarks described in Sec. V.

The appearance of sea quarks in the light—cone wave function of the nucleon in the chiral quark—soliton model can be viewed as the creation of quark—antiquark pairs by the chiral field produced by the other constituents. In general this is a complicated process, which affects the state of motion of the source particles by changing their longitudinal and transverse momenta. Also, the produced pair can re-interact with the chiral field and experience distortion of its wave function. The limit of large transverse momenta, Eq. (6.1), permits several important simplifications, which make it possible to describe this process in practice and calculate the sea quark component of the wave function in a controlled approximation.

First, the invariant mass difference in the pair creation process is dominated by the invariant mass of the pair, while the contribution from the change of the state of motion of the source system can be neglected. Consider the creation of a pair with overall plus momentum fraction y and transverse momentum k_T by a "source" with mass $\sim M_N$ (the precise coefficient does not matter) and initial transverse momentum zero. Let z and \bar{z} be the relative plus momentum fractions of the quark and antiquark in the pair, and p_T the transverse momentum of the quark (cf. Sec. VB). The change of invariant mass

of the total system (source and quark–antiquark pair) in the process is

$$\Delta s_{\text{tot}} = \frac{M^2 + \mathbf{p}_T^2}{yz} + \frac{M^2 + (\mathbf{k}_T - \mathbf{p}_T)^2}{y\bar{z}} + \frac{M_N^2 + \mathbf{k}_T^2}{\bar{y}} - M_N^2$$

$$= \frac{1}{y} \left[\frac{M^2 + \mathbf{p}_T^2}{z} + \frac{M^2 + (\mathbf{k}_T - \mathbf{p}_T)^2}{\bar{z}} + \frac{y^2 M_N^2 + y \mathbf{k}_T^2}{\bar{y}} \right].$$
(6.2)

The longitudinal and transverse momentum transfer by the source is of the order

$$|\mathbf{k}_T| \sim M,$$
 (6.3)

$$yM_N \sim M.$$
 (6.4)

In the limit $p_T^2 \gg M^2$ we can neglect the last term in the parenthesis in Eq. (6.2) and drop k_T and M in the other terms. The total invariant mass difference is thus determined by the intrinsic invariant mass of the quarkantiquark pair, s, cf. Eq. (5.33), and given by

$$\Delta s_{\rm tot} \approx \frac{p_T^2}{yz\bar{z}} = \frac{s}{y}.$$
 (6.5)

Second, in the region $p_T^2 \gg M^2$ the interaction of the quark–antiquark pair with the source is effectively given by the leading–order Born approximation in the nontrivial part of chiral field,

$$M[U^{\gamma_5}(x) - 1],$$
 (6.6)

describing the deviation from the vacuum. Higher–order interactions come with higher powers of the constituent quark mass (as well as gradients of the chiral fields) and are suppressed by inverse powers of p_T . This means that at $p_T^2 \gg M^2$ the distortion of the internal wave function of the quark–antiquark pair can be neglected, and that it can be regarded as being in a plane–wave state after its creation.

Altogether, we see that a very simple picture of the sea quark component of the nucleon's partonic wave function emerges at $p_T^2 \gg M^2$. The fast–moving nucleon creates color–singlet quark–antiquark pairs through the interaction Hamiltonian

$$H_{\text{int}}(t) = \int d^3x \, \bar{\psi}(t, \boldsymbol{x}) \, M[U^{\gamma_5}(t, \boldsymbol{x}) - 1]_{\text{ret}} \, \psi(t, \boldsymbol{x}),$$

$$(6.7)$$

where $[U^{\gamma_5}-1]_{\rm ret}$ is the nontrivial chiral field produced by the other constituents, in the sense of a retarded potential. The interaction is to be treated in first order, and the pair is produced in a plane–wave state. In this approximation the rest of the nucleon producing the pair acts as a classical source (henceforth called "classical nucleon"); it transfers longitudinal and transverse momentum as well as spin/isospin quantum numbers to the pair but otherwise remains inert.

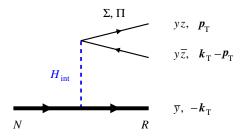


FIG. 16. (Color online) Approximation to the nucleon's lightcone wave function at $p_T^2\gg M^2$. The nucleon acts as a classical source, which produces a color–singlet quark–antiquark pair through the retarded potential Eq. (6.7). The longitudinal momentum fractions and transverse momenta in the final state are indicated on the right ($\bar{y}\equiv 1-y$ etc.). The outgoing classical nucleon can be in a rotational state with N or Δ quantum numbers. The quark–antiquark pair can have scalar–isoscalar (Σ) or pseudoscalar–isovector (Π) quantum numbers.

One may ask whether the approximations proposed here respect chiral invariance. As it stands, first—order Born approximation with the Hamiltonian Eq. (6.7) does not result in chirally invariant amplitudes. However, below we shall see that chiral invariance is effectively restored in the momentum density of quarks and antiquarks at high p_T , as it should be.

With the above approximations it is straightforward to calculate the high- p_T component of the nucleon's partonic wave function (see Fig. 16). Using ordinary time-ordered perturbation theory, we calculate the amplitude for a fast-moving nucleon at $t=-\infty$ to produce a quark-antiquark pair at time t=0 via the interaction Eq. (6.7), assuming that the interaction is adiabatically switched on starting from $t=-\infty$. We obtain

$$\langle q(\boldsymbol{p}_{1}, \sigma_{1}, f_{1}, c_{1}) \, \bar{q}(\boldsymbol{p}_{2}, \sigma_{2}, f_{2}, c_{2}), \, R(\boldsymbol{P}_{R}, I_{R}) \, |$$

$$\left[(-i) \int_{-\infty}^{0} dt \, H_{\text{int}}(t) \right] \, | \, N(\boldsymbol{P}_{N}, I_{N}) \, \rangle$$

$$= (2\pi)^{3} \, \delta^{(3)}(\boldsymbol{p}_{1} + \boldsymbol{p}_{2} + \boldsymbol{P}_{R} - \boldsymbol{P}_{N}) \, \delta_{c_{1}c_{2}}$$

$$\times \, \frac{\bar{u}(\boldsymbol{p}_{1}, \sigma_{1}, f_{1}) \, \Gamma \, v(\boldsymbol{p}_{2}, \sigma_{2}, f_{2})}{E_{1} + E_{2} + E_{R} - E_{N}}. \tag{6.8}$$

Here the momentum and energy of the nucleon in the initial state are

$$\mathbf{P}_N = (\mathbf{0}, P), \tag{6.9}$$

$$E_N = \sqrt{P^2 + M_N^2},\tag{6.10}$$

and the momenta and energies of the quark and antiquark are

$$\boldsymbol{p}_1 = (\boldsymbol{p}_T, \ yzP), \tag{6.11}$$

$$\boldsymbol{p}_2 = (\boldsymbol{k}_T - \boldsymbol{p}_T, \ y\bar{z}P), \tag{6.12}$$

$$E_{1,2} = \sqrt{|\boldsymbol{p}_{1,2}|^2 + M^2},$$
 (6.13)

such that the total momentum of the pair is

$$k \equiv p_1 + p_2 = (k_T, yP).$$
 (6.14)

The momentum of the recoiling classical nucleon state R is fixed by the momentum–conserving delta function, and its energy is

$$E_R = \sqrt{|\boldsymbol{P} - \boldsymbol{p}_1 - \boldsymbol{p}_2|^2 + M_N^2}.$$
 (6.15)

The nucleon and quark momentum states are normalized according to the relativistic convention,

$$\langle N(\mathbf{P}')|N(\mathbf{P})\rangle = 2E_N (2\pi)^3 \delta^{(3)}(\mathbf{P}'-\mathbf{P}), \text{ etc. } (6.16)$$

Eq. (6.8) and all subsequent expressions are to be considered in the limit $P \to \infty$, where the matrix element represents the nucleon wave function in the infinite—momentum frame, in the approximation specified above.

In Eq. (6.8), Γ denotes the transition matrix element of the retarded potential between classical nucleon states,

$$\Gamma \equiv \langle R(\mathbf{P}_R, I_R) | [U^{\gamma_5}(0) - 1]_{\text{ret}} | N(\mathbf{P}_N, I_N) \rangle$$

= $F_{\pi}^{-1} (\Sigma + i\gamma_5 \tau^a \Pi^a),$ (6.17)

where Σ and Π^a are the effective scalar and pseudoscalar field of the transition. The spin-isospin quantum numbers of the states are summarily denoted by $I_N \equiv$ $(S_N, T_N, T_{N3}, S_{N3})$, where $S_N = T_N$ is the spin/isospin and T_{N3} and S_{N3}) their projections, and similarly for I_R . Note that the recoiling classical nucleon can be in a different rotational state from the initial one; in the case of a transition induced by the quark-antiquark operator considered here it can have N or Δ quantum numbers (we explicitly evaluate the matrix element below). Furthermore, in Eq. (6.8) $\sigma_{1,2}$ and $f_{1,2}$ are the spin and flavor quantum numbers of the quark and antiquark states, and u and v their plane—wave Dirac spinor and isospinor wave functions, normalized as $\bar{u}u = -\bar{v}v = 2M$. The color quantum numbers are denoted by $c_{1,2}$, and the pair is in a color-singlet state.

To evaluate Eq. (6.8) further, we note that the energy denominator in the limit $P \to \infty$ is proportional to the invariant mass difference between the initial and final state, Eq. (6.2),

$$E_1 + E_2 + E_R - E_N \sim \frac{\Delta s_{\text{tot}}}{2P} = \frac{s}{2yP},$$
 (6.18)

where we have used the approximation Eq. (6.5) in the last step. We see that we can write the right-hand side of Eq. (6.8) as

$$\frac{\bar{u}(\boldsymbol{p}_{1}, \sigma_{1}, f_{1}) \Gamma v(\boldsymbol{p}_{2}, \sigma_{2}, f_{2})}{E_{1} + E_{2} + E_{R} - E_{N}}$$

$$= 2yP \left[\Sigma \psi_{\Sigma}(z, \boldsymbol{p}_{T}; \sigma_{1}, f_{1}; \sigma_{2}, f_{2}) + \Pi^{a} \psi_{\Pi}^{a}(z, \boldsymbol{p}_{T}; \sigma_{1}, f_{1}; \sigma_{2}, f_{2}) \right]. \quad (6.19)$$

Here ψ_{Σ} and ψ_{Π}^a are the infinite–momentum–frame wave functions of a quark–antiquark pair with scalar–isoscalar

and pseudoscalar–isovector quantum numbers in the effective chiral model,

$$\psi_{\Sigma} = \frac{M}{F_{\pi}} \frac{\bar{u}(\boldsymbol{p}_1, \sigma_1) v(\boldsymbol{p}_2, \sigma_2)}{s} \, \delta_{f_1 f_2}, \tag{6.20}$$

$$\psi_{\Pi}^{a} = \frac{M}{F_{\pi}} \frac{\bar{u}(\mathbf{p}_{1}, \sigma_{1}) i \gamma_{5} v(\mathbf{p}_{2}, \sigma_{2})}{s} (\tau^{a})_{f_{1} f_{2}}. \quad (6.21)$$

They are independent of the overall longitudinal momentum and depend only on the quark momentum fraction z and the transverse momentum p_T (we neglect the transverse momentum of the pair as a whole, k_T , relative to the intrinsic transverse momentum p_T), as well as on the spin and flavor quantum numbers.

B. Spin structure of pair correlations

The explicit expressions for the plane—wave Dirac spinors of the quark and antiquark, with the spin projections σ_1 and σ_2 defined relative to the (fixed) 3–axis, are

$$u(\mathbf{p}_1, \sigma_1) = \begin{pmatrix} \sqrt{E_1 + M} \ w(\sigma_1) \\ \sqrt{E_1 - M} \ \frac{\mathbf{p}_1 \hat{\boldsymbol{\sigma}}}{|\mathbf{p}_1|} \ w(\sigma_1) \end{pmatrix}, \tag{6.22}$$

$$v(\mathbf{p}_2, \sigma_2) = \begin{pmatrix} -\sqrt{E_2 - M} \frac{\mathbf{p}_1 \hat{\boldsymbol{\sigma}}}{|\mathbf{p}_1|} \hat{\sigma}^2 w(\sigma_2) \\ -\sqrt{E_2 + M} \hat{\sigma}^2 w(\sigma_2) \end{pmatrix}, \quad (6.23)$$

where $\hat{\sigma}^i (i=1,2,3)$ are the Pauli spin matrices (to avoid confusion with the spin quantum numbers we distinguish them by the hat) and $w(\sigma_{1,2})$ is a two–spinor with

$$w(\sigma_{1,2} = 1/2) = \begin{pmatrix} 1 \\ 0 \end{pmatrix}, \ w(\sigma_{1,2} = -1/2) = \begin{pmatrix} 0 \\ 1 \end{pmatrix}.$$
(6.24)

Substituting these expressions and evaluating the bilinear forms in the limit $P \to \infty$, we obtain the spin structure of the pair wave functions, Eqs. (6.20) and (6.21), as

$$\psi_{\Sigma} = \frac{M}{F_{\pi}\sqrt{z\bar{z}} s} \, \delta_{f_1 f_2}$$

$$\times \left[(\hat{\boldsymbol{\sigma}} \boldsymbol{p}_T) \hat{\sigma}^2 + (2z - 1) M \hat{\sigma}^3 \hat{\sigma}^2 \right]_{\sigma_1 \sigma_2}, \quad (6.25)$$

$$\psi_{\Pi}^a = \frac{M}{F_{\pi}\sqrt{z\bar{z}} s} \, (\tau^a)_{f_1 f_2}$$

$$\times i \left[-(\hat{\boldsymbol{\sigma}} \boldsymbol{p}_T) \hat{\sigma}^3 \hat{\sigma}^2 + M \hat{\sigma}^2 \right]_{\sigma_1 \sigma_2}. \quad (6.26)$$

In the terms proportional to p_T the spin projections of the quark and antiquark are parallel (the matrix is diagonal); they correspond to configurations with orbital angular momentum L=1. The presence of these configurations is a direct consequence of the chirally-odd structure of the coupling of the quark-antiquark pair to the chiral field $(1, \gamma_5)$. Note that these terms have the same coefficient in both pairs, up to a phase factor. In

the terms proportional to M in Eqs. (6.25) and (6.26) the spin projections of the quark and antiquark are antiparallel (the matrix is off–diagonal); in the case of ψ_{Π}^{a} this term would correspond to the spin–flavor wave function of the pion in the nonrelativistic quark model.

C. Restoration of chiral symmetry

An interesting simplification happens with the pair wave functions of Eqs. (6.25) and (6.26) in the region $|\mathbf{p}_T| \gg M$, where we want to use them to in our approximation to the nucleon wave function. In this region the first term in the spin wave function of Eqs. (6.25) and (6.26) dominates, and one finds

$$\sum_{\sigma_{1},\sigma_{2}} \sum_{f_{1},f_{2}} |\psi_{\Sigma}|^{2} \approx \sum_{\sigma_{1},\sigma_{2}} \sum_{f_{1},f_{2}} |\psi_{\Pi}^{a}|^{2}$$

$$\approx \frac{4M^{2} p_{T}^{2}}{F_{\pi}^{2} z \bar{z} s^{2}} \equiv |\psi_{\text{pair}}|^{2} \quad (6.27)$$

(here a=1,2,3 is fixed; no summation over a). Thus, chiral symmetry is effectively "restored" in the quark–antiquark pair wave function at high momenta. This finding is important in ensuring the chiral invariance of the one–body density of sea quarks, as shown below. It also explains the close connection between the flavor–singlet unpolarized and the flavor–nonsinglet polarized sea quark distributions observed in Sec. V J.

Equation (6.27) also shows that the high- p_T behavior of the sea quark density is entirely governed by the L=1 component of the pair wave function induced by chiral symmetry breaking. This fact has implications for our general understanding of chiral symmetry breaking in a light-front wave function description of the nucleon.

D. Momentum distribution from pairs

Let us now calculate the one-body momentum density of sea quarks from the first-order "wave function" of Eq. (6.8). Generalizing Eqs. (3.2) and (3.3), the flavor-singlet unpolarized antiquark density is obtained as

$$\frac{P}{(2\pi)^3} \langle N(\mathbf{P}', I_N) |
\times \sum_{f=u,d} \sum_{\sigma} b_{f\sigma}^{\dagger}(\mathbf{p}) b_{f\sigma}(\mathbf{p}) | N(\mathbf{P}, I_N) \rangle
= 2E_N(2\pi)^3 \delta^{(3)}(\mathbf{P}' - \mathbf{P}) f_1^{\bar{u}+\bar{d}}(x, \mathbf{p}_T)$$
(6.28)

$$[\mathbf{p} = (\mathbf{p}_T, xP)].$$

The delta function on the right-hand side appears because, in difference from Eqs. (3.2) and (3.3), the center-of-mass motion of the nucleon is now quantized and the states normalized according to Eq. (6.16). Substituting for the nucleon states the first-order quark-antiquark

component of Eq. (6.8), and resolving the constraints resulting from momentum conservation, we get

$$f_1^{\bar{u}+\bar{d}}(x, \mathbf{p}_T) = \frac{P}{(2\pi)^3} \int \frac{d^3k}{(2\pi)^3} \frac{(2yP)^2 N_c A}{2E_1 2E_2 2E_R 2E_N}$$
(6.29)
=
$$\int dy \int d^2k_T \frac{N_c A}{(2\pi)^6 4y^2 z\bar{z}},$$
(6.30)

where

$$A \equiv \sum_{I_R} \sum_{f_1, f_2} \sum_{\sigma_1, \sigma_2} \times (\Sigma^* \psi_{\Sigma}^* + \Pi^{a*} \psi_{\Pi}^{a*})_{\sigma_1 f_1, \sigma_2 f_2} \times (\Sigma \psi_{\Sigma} + \Pi^b \psi_{\Pi}^b)_{\sigma_1 f_1, \sigma_2 f_2}.$$
(6.31)

In Eq. (6.29) we have chosen the pair momentum k as integration variable, cf. Eq. (6.14), so that $y=k^3/P$ and z=x/y under the integral; in Eq. (6.30) we have changed the integration variable from k^3 to y and replaced the energies by their values in the $P\to\infty$ limit, with $E_R=(1-y)P\approx P$ in our approximation. The factor N_c results from the summation over the quarkantiquark colors. The sum over spins and flavors in Eq. (6.31) is readily evaluated. Because of the different symmetry of the Π and Σ pair wave functions the cross terms vanish, and we have

$$A = \sum_{I_R} \sum_{\sigma_1, \sigma_2} \sum_{f_1, f_2} \left(\Sigma^* \Sigma \ \psi_{\Sigma}^* \psi_{\Sigma} + \Pi^{a*} \Pi^b \ \psi_{\Pi}^{a*} \psi_{\Pi}^b \right)$$

$$\approx \sum_{I_R} \left(\Sigma^* \Sigma + \Pi^{a*} \Pi^a \right) |\psi_{I}| \cdot |^2 \quad (n^2 \gg M^2) \quad (6.5)$$

$$\approx \sum_{I_R} (\Sigma^* \Sigma + \Pi^{a*} \Pi^a) |\psi_{\text{pair}}|^2 \quad (p_T^2 \gg M^2).$$
 (6.32)

In the last step we have taken into account that in the region $p_T^2 \gg M^2$ the pair wave functions become alike due to the "restoration of chiral symmetry," cf. Eq. (6.27). As a result, the transition Π and Σ fields effectively appear in a chirally invariant combination, rendering our result chirally invariant.

Combining everything, we can represent Eq. (6.30) in the form of a convolution integral of momentum densities, as obtained earlier from the gradient expansion, cf. Eq. (5.21),

$$f_1^{\bar{u}+\bar{d}}(x,p_T) = \int_x^\infty \frac{dy}{y} f_{\rm cl}(y) f_{q\bar{q}}(x/y,p_T),$$
 (6.33)

where now

$$f_{\rm cl}(y) = \frac{y}{2(2\pi)^3} \int d^2k_T \sum_{I_R} (\Sigma^* \Sigma + \Pi^{a*} \Pi^a),$$
(6.34)

$$f_{q\bar{q}}(z, p_T) = \frac{N_c |\psi_{\text{pair}}|^2}{(2\pi)^3 2z\bar{z}}$$
 $(z = x/y).$ (6.35)

These formulas establish the desired connection with the gradient expansion of the one—body densities in Sec. V. The light—cone momentum density of the chiral field Eq. (5.22) appears as the square of the effective scalar and

pseudoscalar fields associated with the transition between the classical nucleon states in which the quark–antiquark pair was produced. The momentum distribution of the quark–antiquark pair, Eq. (5.23), in turn, is given by the squared light–cone wave function of the pair, according to the standard overlap formula (the particular factor $1/[(2\pi)^32z\bar{z}]$ is a consequence of our definition of the wave function).

The UV cutoff of the effective dynamics can be introduced into our treatment of pair correlated pairs in the nucleon's light—cone wave function in the same manner as discussed in Sec. VF. The invariant mass cutoff Eq. (5.56) can naturally implemented at the wave function level by multiplying the pair wave functions with the cutoff function,

$$\psi_{\Sigma} \to \psi_{\Sigma} F(s),$$
 (6.36)

$$\psi_{\Pi}^a \to \psi_{\Pi}^a F(s). \tag{6.37}$$

In fact, the physical significance of this regularization scheme emerges here at the wave function level. Note that the restoration of chiral symmetry at $p_T^2 \gg M^2$ is preserved if the Σ – and Π –type pairs are suppressed at large s in the same manner.

It remains to show that the light-cone momentum density defined by Eq. (6.34) coincides with the expression Eq. (5.22) obtained from the gradient expansion of the one-body density. Here we can use the fact that the transition matrix element defined by Eq. (6.17) is invariant under longitudinal boosts and behaves like a lightcone wave function. The classical fields are (pseudo-) scalars, and the only effect of a longitudinal boost is on their space-time dependence, while the transition matrix element depends only on the four-momentum transfer between the initial and final classical nucleon state, $k \equiv P_N - P_R$. More explicitly, the boost invariance of Eq. (6.34) can be demonstrated by considering the case of small fields that are generated perturbatively from a pointlike classical source via a Lorentz-invariant retarded Green function.

We can therefore evaluate Eq. (6.34) in the rest frame, where the initial and final baryon 3-momenta are

$$P_N = 0, (6.38)$$

$$\boldsymbol{P}_{R} = (-\boldsymbol{k}_{T}, -yM_{N}), \tag{6.39}$$

and the 3-momentum transfer to the nucleon is

$$k = P_N - P_R = (k_T, yM_N).$$
 (6.40)

In the sense of the $1/N_c$ expansion its components are of the order

$$yM_N, |\mathbf{k}_T| = O(N_c^0),$$
 (6.41)

and the energy difference between the initial and final classical nucleon states is

$$E_R - M_N = \sqrt{|\mathbf{k}|^2 + M_N^2} - M_N \tag{6.42}$$

$$\approx \frac{|\mathbf{k}|^2}{2M_N} = O(N_c^{-1}).$$
 (6.43)

In this frame the classical nucleon effectively behaves as a nonrelativistic system. In particular, as a consequence of Eq. (6.43), the "plus" momentum transfer between the states is in leading order of $1/N_c$ expansion completely given by the 3–momentum transfer, and we obtain

$$k^{+} = P^{+} - R^{+} = M_{N} - E_{R} - R^{3}$$

$$= yM_{N} + O(N_{c}^{-1})$$

$$= yP^{+} + O(N_{c}^{-1}), \qquad (6.44)$$

as it should be, cf. the discussion in Sec. III C. In this frame the space—time dependent chiral field is given by

$$U^{\gamma_5}(t, \boldsymbol{x})_{\text{ret}} = U_{\text{cl}}^{\gamma_5}(\boldsymbol{x} - \boldsymbol{X}), \tag{6.45}$$

where X is the center-of-mass coordinate of the classical nucleon, and the matrix element between momentum eigenstates of the classical nucleon is calculated as [30]

$$\langle \mathbf{P}_{R} | [U^{\gamma_{5}}(0) - 1]_{\text{ret}} | \mathbf{P}_{N} \rangle$$

$$= 2M_{N} \int d^{3}X \ e^{i(\mathbf{P}_{R} - \mathbf{P}_{N})\mathbf{X}} \ [U_{\text{cl}}^{\gamma_{5}}(\mathbf{x} - \mathbf{X}) - 1]$$

$$= 2M_{N} U_{\text{cl}}^{\gamma_{5}}(\mathbf{k}) \mathbf{k}_{\mathbf{k} = (yM_{N}, \mathbf{k}_{T})}$$

$$= 2M_{N} \left[\frac{1 + \gamma_{5}}{2} U_{\text{cl}}(\mathbf{k}) + \frac{1 - \gamma_{5}}{2} U_{\text{cl}}(-\mathbf{k})^{\dagger} \right], \quad (6.46)$$

cf. Eq. (5.6); the factor $2M_N$ results from the relativistic normalization of states, Eq. (6.16). Finally, the matrix element between rotational states of the classical nucleon is obtained by subjecting the classical field to an (iso–) spin rotation

$$U_{cl} \rightarrow RU_{cl}R^{\dagger}$$
 (6.47)

and calculating the transition matrix elements between the initial and recoiling rotational states, using

$$\langle I_R | \dots | I_N \rangle = \int dR \, \phi_{I_R}(R)^* \dots \phi_{I_N}(R), \quad (6.48)$$

where the integration is over the group measure the rotational wave functions are given in terms of the the Wigner D-functions [30]. In the case at hand we actually do not need to calculate the integral Eq. (6.48) for a given I_R , as the sum over rotational quantum numbers in Eq. (6.34) produces a delta function that rigidly couples the rotations in the matrix element and its complex conjugate,

$$\sum_{I_R} \phi_{I_R}(R') \ \phi_{I_R}(R)^* = \delta(R - R'). \tag{6.49}$$

The rotational average thus reduces to a single integral as in the expectation value of the one–body density. Combining everything, we finally obtain

$$\sum_{I_R} (\Sigma^* \Sigma + \Pi^{a*} \Pi^a)$$

$$= \frac{F_\pi^2}{8} \sum_{I_R} \operatorname{tr} [\Gamma^{\dagger} \Gamma]$$

$$= 2M_N^2 F_\pi^2 \operatorname{tr}_{\mathrm{fl}} [U_{\mathrm{cl}}(\boldsymbol{k}) U_{\mathrm{cl}}(\boldsymbol{k})^{\dagger}]. \tag{6.50}$$

Inserting this result into Eq. (6.34) we obtain precisely Eq. (5.22). This completes the proof that the first–order nucleon wave function Eq. (6.8) reproduces the gradient expansion result for the one–body momentum density of sea quarks discussed in Sec. V.

The calculation of the sea quark density from correlated pairs in the nucleon's light-cone wave function presented here can easily be extended to the flavornonsinglet polarized distribution. One finds that this distribution originates from the interference of Σ - and Π -type pairs in the wave function of the initial and final state; this structure was already discussed in connection with the meson cloud model in Ref. [65]. The restoration of chiral symmetry in the light-cone wave function of the pairs [cf. Eq. (6.27) for the probabilities] naturally leads to the result that the $\Sigma\Pi$ and $\Pi\Sigma$ wave function overlap at $p_T^2 \gg M^2$ is of the same form as the $\Sigma\Sigma$ and $\Pi\Pi$ ones producing the flavor–singlet unpolarized density. In the conventions of Sec. V J this implies that $g_{q\bar{q}}(z, p_T) \equiv f_{q\bar{q}}(z, p_T)$, Eq. (5.72), which was obtained independently from the gradient expansion of the respective densities. Furthermore, the pertinent transition fields Σ and Π^a , now defined as matrix elements in which the initial/final nucleon state has a definite spin projection 1/2 and isospin projection 1/2, combine to produce the polarized momentum distribution Eq. (5.68). Thus, the existence of Σ and Π pair correlations and the restoration of chiral symmetry at $p_T^2 \gg M^2$ naturally explain the close connection between the flavor-singlet unpolarized and the flavor-nonsinglet polarized sea in the chiral quark-soliton model.

VII. SUMMARY AND DISCUSSION

A. Summary of model results

In this article we have studied the effect of dynamical chiral symmetry breaking on the intrinsic transverse momentum distributions of partons, using the chiral quark—soliton model as an approximate description of the effective dynamics below the chiral symmetry—breaking scale. To conclude our investigation, we would like to summarize the findings from our model calculations, revisit the question of the embedding in QCD, and outline possible applications of our results to deep—inelastic processes.

The results of our study of transverse momentum distributions in the chiral quark—soliton model can be summarized as follows:

• The constituent quark picture of the effective chiral dynamics implies a natural definition of the intrinsic transverse momentum distributions of partons, extending the established description of p_T —integrated parton densities in this approach. The model describes the p_T —distributions of constituent quarks and antiquarks, which are to be matched with QCD quarks, antiquarks and gluons at the chiral symmetry—breaking scale.

- The distribution of valence quarks (quarks minus antiquarks) is dominated by momenta of the order of the inverse nucleon size, $p_T \sim M \sim R^{-1}$ and shows an approximate Gaussian shape. The systematic differences between the unpolarized and polarized valence quark p_T distributions attest to the relativistic character of the nucleon bound state.
- The distribution of sea quarks is qualitatively different and shows a would—be power—like tail $\sim 1/p_T^2$ extending up to the UV cutoff. Its coefficient is determined by low—energy chiral dynamics and quasi model—independent. Such behavior is found in both the flavor—singlet unpolarized and the flavor—nonsinglet polarized distribution.
- The UV cutoff of the model influences the shape of the sea quark transverse momentum distribution at momenta $p_T^2 \sim \text{few } M^2$. Imposing rather general physical conditions on the regularization scheme (analyticity, charge conservation, large-distance behavior) stable numerical results for the sea quark distributions are obtained up to $p_T^2 \sim 10\,M^2$. The sea quark p_T distribution thus obtained is qualitatively different from that of the valence quarks and extends up to much larger values of p_T .
- The power–like tail in the sea quark distribution can be explained microscopically as the result of short–range correlations in the nucleon's light–cone wave function. The relevant configurations are quark–antiquark pairs with transverse momenta $p_T^2\gg M^2$ created by the classical chiral field. These pairs can have scalar–isoscalar (Σ) and pseudoscalar–isovector (Π) quantum numbers, whose wave functions become identical at $p_T^2\gg M^2$, corresponding to an effective "restoration of chiral symmetry" at the cutoff scale.
- The coordinate—space correlation function obtained as the Fourier—Bessel transform of the sea quark p_T distribution is unambiguously defined in the model. At large transverse distances it decays exponentially with a characteristic range determined by the constituent quark mass and the spatial size of the mean field. At zero transverse distances it coincides with the p_T —integrated parton density. It is thus tightly constrained and largely independent of the regularization scheme.
- The flavor–singlet unpolarized and the flavor nonsinglet polarized sea quark p_T distributions at $p_T^2 \gg M^2$ satisfy the large– N_c inequalities for transverse momentum distributions, as a result of the invariance properties of the classical chiral field and the "restoration of chiral symmetry" in quark–antiquark pairs with $p_T^2 \gg M^2$.

When interpreting the results of our study or using them for phenomenology, one should keep in mind that the specific numerical results for the valence and sea quark transverse momentum distributions (see Figs. 14 and 15) are model-dependent and should not be taken too literally. The numerical values of the sea quark transverse momentum distributions are strongly affected by the UV cutoff, and while it is very encouraging that the physically motivated regularization schemes described here produce stable distributions, we cannot exclude that further refinement of the UV regularization would change the numerical values. Furthermore, as explained in Sec. I and discussed further in the following subsections, the distributions refer to effective degrees of freedom defined by the model, and we presently cannot express them objectively as matrix elements of a priori defined QCD operators in the nucleon. Our main result is the qualitative difference between the valence and sea quark transverse momentum distributions. We expect it to be modelindependent because it is rooted in the basic structure of the effective dynamics resulting from chiral symmetry breaking and can at least qualitatively be explained in QCD proper (see Sec. VIIC). Any applications of our results should therefore focus on this qualitative difference rather than the specific numerical values of the distributions (see Sec. VIII).

The study of the p_T distributions in the chiral quark soliton model presented here could be extended in various directions. One obviously should calculate also the p_T distribution of the $1/N_c$ -suppressed combinations of the parton densities, namely the flavor–nonsinglet unpolarized densities, f_1^{u-d} and $f_1^{\bar{u}-\bar{d}}$ and the flavor–singlet polarized ones, g_1^{u+d} and $g_1^{\bar{u}+\bar{d}}$. These distributions are proportional to the angular velocity of the isorotational motion of the soliton, $\Omega \sim 1/N_c$ and the corresponding expressions can be derived in analogy to those of the leading distributions in Sec. IIIB, using the techniques described in Refs. [32, 66]. An interesting question is whether the $1/N_c$ -suppressed sea quark distributions also exhibit a power–like tail at $p_T^2 \gg M^2$, and to what extent this behavior would differ from that of the $1/N_c$ -leading distributions. It is known that the UV cutoff dependence of the flavor-nonsinglet unpolarized distribution in the model is qualitatively different from that of the singlet distribution at parametrically small values $x \sim M/(\Lambda N_c)$ [66], suggesting a qualitatively different behavior also of the p_T distributions.

Equally interesting is the p_T dependence of the quark transversity distributions h_1^q and $h_1^{\bar{q}}$. Earlier studies [67, 68] revealed that the sea quark transversity distributions in the chiral quark–soliton model are finite in the limit of large UV cutoff and numerically small, which would indicate that there is no $\sim 1/p_T^2$ tail in the p_T distribution. It would be especially interesting to explain the different behavior of the transversity distributions at the wave function level, using the method developed in Sec. VI.

Another direction is the study of short–range parton

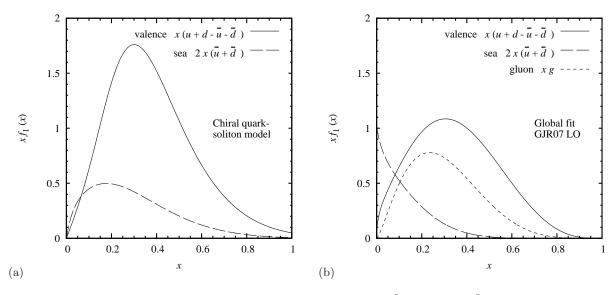


FIG. 17. Unpolarized flavor–singlet parton momentum densities $xf_1^{u+d-\bar{u}-\bar{d}}(x)$ and $xf_1^{\bar{u}-\bar{d}}(x)$. The sea quark momentum densities are plotted multiplied by a factor 2, with which they appear in the momentum sum rule. (a) Chiral quark–soliton model. Shown are the results obtained with the numerical approximations Eqs. (4.3) and (5.66) [self–consistent soliton profile Eq. (A4), $M=0.35~{\rm GeV}, M_N=3.26~M$; sea quark distribution with PV regularization]. The constituent quarks and antiquarks carry the entire light–cone momentum of the nucleon in the model. (b) QCD parton densities from the global fit of Ref. [34] (GJV07 LO, scale $\mu_{\rm LO}^2=0.3~{\rm GeV}^2$). Gluons carry $\sim 30\%$ of the nucleon's light–cone momentum.

correlations at the wave function level. In Sec. VI we calculate the nucleon wave function at $p_T^2 \gg M^2$ in the simplest possible approximation, which violates chiral invariance (although it is effectively restored at high p_T). It would be worth developing a manifestly chirally invariant expansion scheme, which takes into account the distortion of the pair wave function by the classical field. This could be done using the induced vector field representation of the effective chiral dynamics, in which the original matrix field U^{γ_5} is absorbed by a chiral rotation of the massive fermion fields. Furthermore, one should further explore the connection of our approximation with the Fock space expansion of the large– N_c baryon wave function of [41–43].

B. Matching with QCD

The approach to partonic structure presented here is based on the idea of an effective description of QCD below the chiral symmetry—breaking scale. The chiral quark—soliton model of the nucleon describes the transverse momentum distribution and correlations of constituent quarks and antiquarks — effective degrees of freedom, which are to be matched with QCD quarks, antiquarks and gluons at the chiral symmetry—breaking scale. As explained in Sec. I, this matching cannot be performed entirely on the basis of intrinsic properties of the effective chiral dynamics but requires additional information about its embedding in QCD, either in the form of a microscopic derivation of the effective model or of phenomenological input. A detailed treatment of this

problem is beyond the scope of the present study. Still we would like to comment on several aspects and draw some conclusions based on the structure of the results obtained within the effective model.

To discuss the matching quantitatively it is instructive to compare the p_T -integrated parton densities in the chiral quark-soliton model, which were studied in several earlier works [32, 33, 56], with empirical parametrizations of the parton densities obtained from global fits (see Fig. 17). Fig. 17a shows the unpolarized flavorsinglet momentum densities of valence and sea quarks in the model, $xf_1^{u+d-\bar{u}-\bar{d}}(x)$ and $xf_1^{\bar{u}+\bar{d}}(x)$. For consistency we show here the results obtained with the numerical approximations employed in the present study of p_T distributions, Eqs. (4.3) and (5.66); these approximations reproduce the exact numerical results for the p_T -integrated valence and sea quark densities [56] with a relative accuracy far better than 10% and 20%, respectively, in the region x < 0.5. Note that the momentum sum rule is satisfied within the model in leading order of the $1/N_c$ expansion [32], which is another testimony to the consistency of the relativistic mean-field approximation. The sum rule is preserved by the PV regularization used here; see Ref. [56] for a detailed discussion. The distributions of constituent quarks and antiquarks obtained in the model thus satisfy

$$\int dx \, x \, [f_1^{u+d-\bar{u}-\bar{d}}(x) \, + \, 2f_1^{\bar{u}+\bar{d}}(x)]_{\text{model}} \ = \ 1. \ \ (7.1)$$

In Fig. 17a the sea quark distribution is plotted including the factor 2 with which it appears in Eq. (7.1). Figure 17b shows the empirical parametrizations of the QCD parton

momentum densities obtained in a recent global fit of DIS and other data [34]. For clarity we show here the leading–order (LO) distributions, which are independent of the renormalization scheme and can readily be compared with the model distributions. The scale of these distributions is $\mu_{\rm LO}^2 = 0.5 \, {\rm GeV^2}$, corresponding approximately to the chiral–symmetry breaking scale $\rho^{-2} \approx 0.4 \, {\rm GeV^2}$ identified in the nonperturbative QCD approaches discussed in Sec. I. In the QCD parton densities the momentum is shared between quarks, antiquarks and gluons, and the momentum sum rule reads

$$\int dx \, x \, [f_1^{u+d-\bar{u}-\bar{d}}(x) + 2f_1^{\bar{u}+\bar{d}}(x) + g(x)]_{\text{QCD}} = 1.$$
(7.2)

According to the fit of Ref. [34] $\sim 30\%$ of the nucleon's momentum at the low scale is carried by gluons. Comparing the model and the QCD parton distributions in Fig. 17a and b two features stand out. First, the total momentum carried by sea quarks is roughly the same; however, the constituent sea quark distributions are noticeably harder (stronger at larger x) than those of the QCD antiquarks. This shows that the matching of the model sea quark distribution with QCD partons is generally nontrivial and may produce and evolution-like effect. Note that the model distributions should not be considered as genuine predictions in the parametrically small region $x \sim M^2/(\Lambda^2 N_c)$, where they are sensitive to the details of the UV cutoff (see Sec. V).] Second, the momentum carried by the valence quarks is smaller in the case of the QCD distributions. This suggests that most of the QCD gluons should be "generated" from the model valence quark distributions in the matching process.

In the simplest approximation one can identify the constituent quarks and antiquarks of the effective model with QCD quarks and antiquarks at the chiral symmetry—breaking scale and set the gluon distribution in the model to zero. For the p_T -integrated parton densities this approximation can be formally justified in the instanton model of the QCD vacuum, where it appears as the leading—order approximation in the expansion of the instanton packing fraction. Fig. 17 and the above discussion show that this approximation is reasonable (at non-exceptional values of x) but of limited accuracy. The limitations of this approximation should be kept in mind when interpreting our results for the p_T distributions.

An important lesson from the fit shown in Fig. 17b is that the empirical gluon density at the low scale shows substantial strength at large values of x>0.2 and has a shape comparable to the valence quark distribution. Such behavior is difficult to explain as the result of a composite structure of *individual* constituent quarks and antiquarks, which, like DGLAP evolution, would produce gluons primarily at values of x much smaller than that of the quarks. It suggests that this component of the gluon density originates rather from *correlations* between constituent quarks, which can leverage the sum of the x-values of the two correlated quarks for the produced gluons. This fact has not been appreciated in most

attempts to explain the empirical gluon density made so far. Whether the relevant correlations are between quark—antiquark pairs in the sea, as found in the present model based on effective chiral dynamics, or diquark—like correlations between valence quarks, is an important question which deserves further study.

C. Toward parton correlations in QCD

The chiral quark-soliton model predicts short-range correlations between constituent quarks and antiquarks as a consequence of a basic property of the effective chiral dynamics: $\Lambda^2 \gg M^2$, or the parametric smallness of the dynamical quark mass compared to the UV cutoff representing the chiral symmetry-breaking scale. An important question is whether and how such parton correlations could be rigorously defined in QCD. The challenge lies in the fact that the relevant dynamical scale arises from chiral symmetry breaking in the QCD vacuum, which is not readily associated with partonic structure in a model-independent manner. Gribov's concept of the partonic wave function of a fast-moving hadron [69] maintains the connection between partons and vacuum structure and should in principle be appropriate for discussing parton correlations as proposed here; however, the concept was developed based on scalar field theory, and the extension to QCD presents many technical challenges (gauge invariance, UV divergences, renormalization). A more rigorous formulation of parton short-range correlations in QCD may be possible with the new concept of multiparton distributions, which were introduced in the description of multiple hard scattering processes in high-energy pp collisions; their operator definition and renormalization properties have been studied in several recent works [70, 71].

Short of a rigorous formulation, we can still develop a qualitative picture of how parton short-range correlations emerge from dynamical chiral symmetry breaking in QCD. In the usual equal-time formulation of relativistic dynamics the QCD vacuum is not empty, but populated by localized nonperturbative gluon fields. These fields create quark-antiquark pairs with a characteristic size $\rho \sim 0.3 \, \text{fm}$ [cf. Eq. (1.4) and following discussion, which form the chiral condensate (see Fig. 18a). Quarks propagating through this medium interact with the vacuum fields and effectively acquire a dynamical mass, which determines much of hadronic structure. This phenomenon has been investigated extensively in slow-moving hadronic states $(P \lesssim \rho^{-1})$, whose properties can be studied using Euclidean (imaginary-time) correlation functions. A partonic description appears when considering hadrons which move with a momentum much larger than the scale of the vacuum fluctuations, $P \gg \rho^{-1}$. Following Gribov [69], in this limit one can separate the quanta carrying a finite fraction of the hadron momentum from those "left behind" in the vacuum, and the hadron becomes a closed system in the

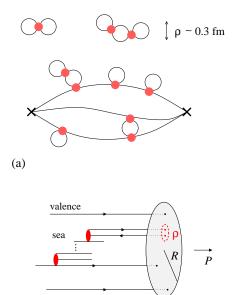


FIG. 18. (Color online) Qualitative picture of the emergence of nonperturbative parton short—range correlations in QCD (details see text). (a) Slow—moving nucleon. (b) Fast—moving nucleon (parton picture).

(b)

quantum-mechanical sense, amenable to a wave function description. When we imagine approaching the regime of large momentum $P \gg \rho^{-1}$ gradually, it is clear that some of the quark-antiquark pairs in the vacuum will be "dragged along" and become the sea quarks in the nucleon's partonic wave function (see Fig. 18b). These pairs of course inherit the typical size ρ with which they exist in the vacuum and thus induce nonperturbative short-range correlations in the nucleon's partonic wave function. In this argument we implicitly assume that the nonperturbative wave function is defined "at a scale of the order ρ^{-2} ," and that configurations with transverse momenta $p_T^2\gtrsim \rho^{-2}$ will be built up by perturbative QCD radiation. While leaving aside many important questions (UV divergences, renormalization) this simple picture qualitatively explains how parton short-range correlations emerge from chiral symmetry breaking in QCD [72].

The picture described here implies that the small–size $q\bar{q}$ pairs in the nucleon wave function are generally accompanied by strong gauge fields with transverse momenta of the order ρ^{-1} . These gauge fields need not necessarily project onto physical gluon states in the limit $P \to \infty$ (e.g., they can correspond to unphysical polarization states), but can exert forces on the quark and antiquark corresponding to higher–twist effects. A transverse momentum–dependent hard scattering process involving sea quarks with $p_T \sim \rho^{-1}$ thus generally takes place in the presence of a strong gluon field. One should therefore expect sizable corrections to the impulse approximation, in which one takes into account the $p_T \sim \rho^{-1}$ of the initial quark/antiquark but not the equally strong final–state interaction with the small–size gluon field. For this

reason we cannot use our calculated p_T distributions directly to make numerical predictions for the transverse momentum distributions in hard processes. Our conclusions regarding semi-inclusive DIS presented below assume only on the existence of the short-distance scale and do not rely on the impulse approximation.

Modeling the effect of the nonperturbative gluon fields at the chiral symmetry—breaking scale in hard scattering processes will be essential for putting the proposed picture of short—range correlations in QCD on a more quantitative footing. The instanton vacuum model has proved to be a valuable tool for estimating the effect of such fields in inclusive DIS, where one can apply the local operator product expansion to identify the scaling (leading—twist) and power—suppressed (higher—twist) parts of the cross section [73–75]. Whether the instanton vacuum model could be adapted to estimate also final—state interactions in semi—inclusive processes is an interesting question for further study.

Another interesting question concerns the color structure of parton short-range correlations in QCD. In the effective model used in the present study the chiral symmetry-breaking color fields are integrated out, and the resulting dynamics generates short-range quarkantiquark correlations only in color–singlet states (Σ, Π) . The parameter N_c in the model really plays the role of a degeneracy or weight factor and no longer refers to actual color interactions. In a more microscopic approach such as the instanton vacuum, short-range correlations could in principle appear also between quark-antiquark pairs in color-octet states, if the color is compensated by physical gluon fields. Such pair correlations would have different properties as initial conditions for QCD radiation starting from the scale ρ^{-2} , and would influence the final state in semi-inclusive processes in a different way, compared to color-singlet correlations. Investigating the possibility of such color-octet correlations in the instanton vacuum model would be an interesting problem for further study.

In sum, our arguments suggest that the short–distance scale associated with dynamical chiral symmetry breaking in the QCD vacuum leaves a characteristic imprint on the nucleon's partonic structure. It implies a definite pattern of intrinsic transverse momentum distributions, in which the distribution of valence quarks is concentrated at p_T^2 of the order of the inverse hadronic size R^{-2} , while that of sea quarks extends up to the chiral symmetry–breaking scale $\rho^{-2}\gg R^{-2}$. At the level of the partonic wave function, the sea quarks show short–range pair correlations that reflect their creation by nonperturbative gluon fields of transverse size ρ . These conclusions are generic and rely only on the existence of the nonperturbative short–distance scale in the QCD vacuum; they do not depend on the particular implementation of this scenario in the effective dynamical model employed here.

VIII. APPLICATIONS TO DEEP-INELASTIC PROCESSES

Our findings about the intrinsic transverse momentum distributions of partons have many implications for DIS experiments with identified particles in the final state. A quantitative description of the transverse momentum spectra in particle production requires further assumptions about perturbative QCD radiation and final—state interactions and detailed modeling of the fragmentation process, and is beyond the scope of the present article. In the following we only want to point out several obvious consequences and applications of our results that can be stated model—independently and merit further detailed study.

A. Perturbative QCD radiation

When applying our results to deep-inelastic processes with identified particles it is important to take into account the effects of perturbative QCD radiation. The picture of intrinsic transverse momentum distributions and parton short-range correlations in the nucleon wave function described in Sec. VII applies at the chiral symmetrybreaking scale ρ^{-2} . Generally, in a hard process perturbative QCD radiation builds up configurations with invariant masses (or virtualities) of the order of the hard scale, Q^2 . In inclusive DIS this radiation is described by DGLAP evolution and well understood. In processes where one measures the transverse momenta of particles in the final state the relevant radiation processes are generally much more complex; for semi-inclusive DIS this problem was recently studied in Ref. [14]. A key question is whether the nonperturbative short-distance scale implied by chiral symmetry breaking, $\rho^{-1} \approx 0.6 \,\mathrm{GeV}$, acts as an infrared cutoff for perturbative radiation in such processes, or whether such radiation (possibly with Sudakov suppression) is still relevant at lower scales. Experimental evidence on this point is ambiguous. Data on jet structure in e^+e^- annihilation can be explained by allowing perturbative radiation to substantially lower scales. At the same time, there are hints from exclusive processes that low-virtuality radiation is suppressed, e.g. in the surprisingly similar magnitude and energy dependence of transverse and longitudinal cross sections in ρ^0 meson production [76]. What these observations imply for semi-inclusive particle production is an interesting question which merits further study.

B. Semi-inclusive measurements

Semi-inclusive DIS with single identified hadrons in the current fragmentation region, $\gamma^* + N \rightarrow h + X$, is a standard tool for separating the different charge and flavor components of the nucleon's parton densities, using the fact that the fragmentation process is sensitive to the

charge and flavor of the struck quark. In these measurements one integrates over the transverse momentum $P_{T,h}$ of the identified hadron h and aims to extract the cross section as a function of the fraction z_h of the virtual photon energy in the target rest frame carried away by the hadron. Generally, the observed transverse momentum $P_{T,h}$ is compounded from the intrinsic transverse momentum of the struck parton, QCD final-state interactions and perturbative radiation, and the transverse momentum incurred during the soft fragmentation process. Our findings about the intrinsic transverse momentum distributions imply that hadrons produced in scattering from antiquarks generally have a much broader $P_{T,h}$ distribution than those produced from quarks, if the transverse momenta incurred from final-state interactions and fragmentation are comparable in both cases. One example is the production of K^+ (valence quark content $u\bar{s}$) and $K^{-}(\bar{u}s)$, where our picture predicts a broader $P_{T,h}$ distribution for the latter, assuming the production is dominated by scattering from u and \bar{u} quarks in the proton. In experiments with incomplete coverage in P_{TK+} this can result in a modification of the observed numbers of K^+ and K^- that is not related to the u and \bar{u} number densities in the target and must be corrected in the charge/flavor separation.

Another instance where this effect plays a role are measurements where relations between fragmentation functions are used to isolate certain combinations of parton densities [77, 78]. For example, the cross sections for semi–inclusive π^+ and π^- production, integrated over the pion transverse momentum $P_{T,\pi}$, is up to an overall kinematic factor given by

$$\sigma^{\pi^{\pm}} \propto e_u^2 \left[f_1^u(x) D_1^{u/\pi^{\pm}}(z_{\pi}) + f_1^{\bar{u}}(x) D_1^{\bar{u}/\pi^{\pm}}(z_{\pi}) \right] + e_d^2 \left[f_1^d(x) D_1^{d/\pi^{\pm}}(z_{\pi}) + f_1^{\bar{d}}(x) D_1^{\bar{d}/\pi^{\pm}}(z_{\pi}) \right], \quad (8.1)$$

where $e_{u,d}$ are the quark charges and $D_1^{u/\pi^+}(z_{\pi})$, etc., the fragmentation functions describing the inclusive probability of a quark/antiquark to produce a π^{\pm} carrying fraction z_{π} of its longitudinal momentum, integrated over the soft transverse momenta. Taking the difference of π^+ and π^- cross sections, and using the relations between the fragmentation functions following from charge conjugation invariance,

$$D_1^{u/\pi^{\pm}}(z_{\pi}) = D_1^{\bar{u}/\pi^{\mp}}(z_{\pi}),$$

$$D_1^{d/\pi^{\pm}}(z_{\pi}) = D_1^{\bar{d}/\pi^{\mp}}(z_{\pi}),$$
(8.2)

and from isospin symmetry,

$$D_1^{u/\pi^{\pm}}(z_{\pi}) = D_1^{d/\pi^{\mp}}(z_{\pi}),$$

$$D_1^{\bar{u}/\pi^{\pm}}(z_{\pi}) = D_1^{\bar{d}/\pi^{\mp}}(z_{\pi}),$$
(8.3)

one obtains

$$\sigma^{\pi^{+}} - \sigma^{\pi^{-}} \propto (e_{u}^{2} - e_{d}^{2})[f_{1}^{u}(x) - f_{1}^{\bar{u}}(x) - f_{1}^{d}(x) + f_{1}^{\bar{d}}(x)] \times [D_{1}^{u/\pi^{+}}(z_{\pi}) - D_{1}^{u/\pi^{-}}(z_{\pi})]. \tag{8.4}$$

A measurement of this cross section difference thus provides direct access to the valence quark densities in the target; the sea quark densities drop out because of the relations between the fragmentation functions. However, this reasoning requires modification if the effects of transverse momenta are taken into account and the experiment covers only part of the relevant $P_{T,\pi}$ -distribution. To illustrate the point, we may use the simple parton model with intrinsic transverse momenta in the parton density and the fragmentation function, where it is assumed that all transverse momentum integrals converge because of some intrinsic soft scale (our conclusion is model-independent and holds also in the presence of QCD radiation and final-state interactions). model the transverse momentum distribution of the identified hadron is given by the convolution of the intrinsic transverse momentum distribution of quarks in the target and that incurred in the fragmentation process,

$$\sigma^{\pi^{\pm}}(P_{T,\pi}) \propto \int d^2 p_T \int d^2 K_T \, \delta^{(2)}(\mathbf{P}_{T,\pi} - z_{\pi} \mathbf{p}_T - \mathbf{K}_T)$$
$$\times \left[e_u^2 \, f_1^u(x, p_T) \, D_1^{u/\pi^{\pm}}(z_{\pi}, K_T) + \ldots \right], (8.5)$$

where the ellipsis denotes the corresponding other terms appearing in Eq. (8.1). Here $D_1^{u/\pi^+}(z_{\pi}, K_T)$ etc. denote the transverse momentum dependent fragmentation function, which satisfy

$$\int d^2 K_T \ D_1^{u/\pi^+}(z_{\pi}, K_T) = D_1^{u/\pi^+}(z_{\pi}), \quad \text{etc. (8.6)}$$

The K_T -dependent fragmentation functions obviously obey the same charge conjugation and isospin symmetry relations as the K_T -integrated ones, Eqs. (8.2) and (8.3). As a result, one obtains a formula analogous to Eq. (8.5) for the difference of cross sections measured at the same $P_{T,\pi}$:

$$[\sigma^{\pi^{+}} - \sigma^{\pi^{-}}](P_{T,\pi})$$

$$\propto \int d^{2}p_{T} \int d^{2}K_{T} \, \delta^{(2)}(\mathbf{P}_{T,\pi} - z_{\pi}\mathbf{p}_{T} - \mathbf{K}_{T})$$

$$\times (e_{u}^{2} - e_{d}^{2}) \left[f_{1}^{u}(x, p_{T}) - f_{1}^{\bar{u}}(x, p_{T}) - f_{1}^{d}(x, p_{T}) \right]$$

$$\times [D_{1}^{u/\pi^{+}}(z_{\pi}, K_{T}) - D_{1}^{u/\pi^{-}}(z_{\pi}, K_{T})]$$
(8.7)

The cross section difference is proportional to the difference of p_T -dependent quark and antiquark distributions. If one integrated over the pion transverse momentum $P_{T,\pi}$ without restriction, the delta function in Eq. (8.7) would disappear, and the unrestricted integrals over p_T and K_T would reduce the transverse momentum-dependent parton distribution and fragmentation functions to the integrated functions of Eq. (8.5). However, one can no longer extract the p_T -integrated valence quark density from Eq. (8.7) from measurements with incomplete $P_{T,\pi}$ coverage if quarks and antiquarks have dif-

ferent intrinsic p_T distributions, as implied by our arguments based on the QCD vacuum structure. To see this, let us write the p_T -dependent quark and antiquark distributions in the simple parton model in the form

$$f_1^u(x, p_T) = f_1^u(x) F_1^u(x, p_T),$$
 (8.8)

$$f_1^{\bar{u}}(x, p_T) = f_1^{\bar{u}}(x) F_1^{\bar{u}}(x, p_T),$$
 (8.9)

and similarly for the d quarks and antiquarks. Here the functions F_1^a describe the normalized p_T profile of the quarks and antiquarks at a given x,

$$\int d^2 p_T F_1^a(x, p_T) = 1, \qquad (a = u, \bar{u}, d, \bar{d}). \quad (8.10)$$

We can then write the differences of p_T -dependent distributions appearing in Eq. (8.7) in the form

$$f_1^u(x, p_T) - f_1^{\bar{u}}(x, p_T)$$

$$= [f_1^u(x) - f_1^{\bar{u}}(x)] F_1^u(x, p_T)$$

$$+ f_1^{\bar{u}}(x) [F_1^u(x, p_T) - F_1^{\bar{u}}(x, p_T)], \text{ etc. } (8.11)$$

If one integrated over p_T without restriction, as would correspond to integration of Eq. (8.7) over all $P_{T,\pi}$, the difference of profile functions on the last line would integrate to zero because of the normalization conditions Eq. (8.10), and the measured cross section difference would be proportional to the integrated valence quark density alone. However, without integration over all p_T the cross section difference contains an admixture of the antiquark distribution because generally $F_1^{\bar{u}}(x, p_T) \neq$ $F_1^u(x, p_T)$. Consequently, one cannot extract the p_T integrated valence quark density from measurements of Eq. (8.7) over an incomplete range of $P_{T,\pi}$ without additional assumptions about the intrinsic transverse momentum dependence. This conclusion is general and not limited to the simple parton model used to illustrate the point. It also affects the use of the pion charge asymmetry (either as an absolute cross section difference or as a ratio of cross sections) in the flavor separation of polarized parton densities with proton and nuclear targets. In practice, there might still be considerable experimental advantages in using observables such as Eq. (8.7) for the study of p_T -integrated parton densities; however, this requires detailed study based on the measured or modeled transverse momentum distributions.

Generally, our findings underscore the importance of accurate measurements of the basic transverse momentum distributions of hadrons (π, K) in unpolarized seminclusive DIS, up to $P_{T,h} \sim 1 \,\mathrm{GeV}$, and differentially in x,z and Q^2 . Simple comparisons between the P_T distribution of different particles (such as K^+ and K^-) can serve as model–independent tests of the predicted pattern of intrinsic transverse momentum distributions. Measurements with a deuteron target would be particularly useful, as they directly access the flavor–singlet (isoscalar) combination of the parton distributions and would allow one to search for signals of a difference between the transverse momentum distributions f_1^{u+d}

and $f_1^{\bar{u}+\bar{d}}$ without the complications of flavor separation. Such measurements provide essential information about the mechanism of particle production in semi–inclusive DIS and should be done before one studies more subtle observables such as spin asymmetries.

C. Correlation measurements

Much more information can be obtained from semiinclusive experiments that measure particle production in the central and target fragmentation regions in correlation with an identified hadron in the current fragmentation region (see Fig. 19). Such measurements can answer the question of what "balances" the $P_{T,h}$ of hadrons observed in the current fragmentation region, which is the key for unraveling the production mechanism in semiinclusive DIS. As emphasized earlier, the $P_{T,h}$ of a hadron observed in the current fragmentation region can come from the parton intrinsic transverse momentum in the target, final-state interactions and QCD radiation in the hard process, or the soft fragmentation process. Singleinclusive measurements alone cannot discriminate between these different sources. Correlation measurements offer additional observables that can test at least the relative importance of the various mechanisms. A fully quantitative theory of such measurements is a complex problem and beyond the scope of the present article. Here we only wish to outline in what kinematic region such experiments could be performed such that they have a simple interpretation in terms of nonperturbative nucleon struc-

In DIS experiments with measurements of multiparticle final states it is convenient to describe the produced particles in terms of their rapidity

$$y_h \equiv \frac{1}{2} \ln \frac{E_h + P_{\parallel,h}}{E_h - P_{\parallel h}},$$
 (8.12)

where $E_h = (P_{\parallel,h}^2 + P_{T,h}^2 + m_h^2)^{1/2}$ is the hadron energy and $P_{\parallel,h}$ the longitudinal momentum, defined as the component in the direction of the virtual photon momentum. The rapidity changes by a constant under Lorentz boosts along the longitudinal direction, so that rapidity differences are frame—independent. The Lorentz—invariant rapidity interval over which particles with a given transverse momentum are distributed is

$$Y \equiv y_{h,\text{max}} - y_{h,\text{min}} \approx \ln[W^2/(P_{T,h}^2 + m_h^2)], (8.13)$$

where W is the γ^*N center–of–mass (CM) energy and it is assumed that $W^2 \gg P_{T,h}^2 + m_h^2$. Studies of hadronic final states in DIS at $W \sim$ few GeV show that the target and current fragmentation regions occupy at least one unit of rapidity. To cleanly separate the two regions, rapidity intervals of $Y \sim 4$ are needed. Our picture based on QCD vacuum structure suggests that one look for correlations between pions with $P_{T,\pi}^2 \sim 0.5 \, \mathrm{GeV}^2$ in

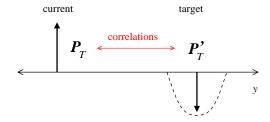


FIG. 19. (Color online) Measurements of particle production in the central and target fragmentation regions in correlation with an identified hadron in the current fragmentation region. y denotes the rapidity.

the current fragmentation region and hadrons with similar transverse momenta in the target fragmentation region. From Eq. (8.13) we see that this requires squared CM energies around $W^2 \approx 30\,\mathrm{GeV}^2$. At these energies sea quarks with $x=0.05\,(0.1)$ could be probed at scales $Q^2 \approx xW^2 = 1.5\,(3.0)\,\mathrm{GeV}^2$, where perturbative QCD radiation still plays a minor role in inclusive particle production. The kinematic region described here thus represents a "window" where one can expect to see nonperturbative correlations between sea quarks reflected in the hadronic final state.

By choosing a leading hadron in the current fragmentation region with $z \gtrsim 0.5$ (z is the fraction of the virtual photon's laboratory energy carried by the produced hadron) one can minimize also the effect of transverse momentum broadening through fragmentation and approximately infer the intrinsic p_T of the struck (anti)quark in the target. By measuring particle production in the central and target fragmentation regions one can then establish how this transverse momentum is balanced in the final state. If the observed $P_{T,h}$ of the forward hadron indeed originated from the nonperturbative intrinsic transverse momentum of quarks in the nucleon, the picture of pair correlations described in Sec. VI implies that the $P_{T,h}$ should be balanced by the other (anti)quark in the pair, which materializes in the target fragmentation region, leading to long-range correlations in rapidity between the current and target fragmentation regions [79]. If, however, the main source of the observed $P_{T,h}$ were the fragmentation process, one expects shortrange correlations within the current fragmentation re-

If Q^2 is increased from the values of \sim few ${\rm GeV}^2$ discussed above, QCD radiation should play an increasing role. In inclusive particle production this is described by DGLAP evolution and well understood theoretically and experimentally. In correlation measurements of the kind described here, these emissions should diminish the correlations expected from soft interactions by providing additional possibilities for the balancing of the observed $P_{T,h}$ in the current fragmentation region.

Correlations between the current and target fragmentation region could be studied by measuring either mesons or baryons, or a collection of hadrons, in the target fragmentation region. The role of baryons in balancing the $P_{T,h}$ of the current jet is likely more important in processes where a valence quark in the target is removed, potentially providing a handle to separate the intrinsic transverse momenta of valence and sea quarks.

Correlation measurements of the kind described here would be feasible in the kinematic region covered by the CERN COMPASS experiment (squared lepton–nucleon CM energy $s \approx 300~{\rm GeV}^2$) [80] or with a medium–energy Electron–Ion Collider [81], if suitable detection capabilities for forward particles are provided. The merit of such correlation measurements in a smaller rapidity interval with the Jefferson Lab 12 GeV Upgrade ($s \approx 20~{\rm GeV}^2$), especially with the CLAS12 detector, deserves further study [82].

D. Multiparton processes

More direct tests of the idea of parton short-range correlations may become possible with the concept of multiparton distributions, whose proper formulation in QCD is a subject of present work [70, 71]. Such distributions are required in the description of pp collisions with multiple hard processes, where correlations manifest themselves as an enhancement of the multiple process rate compared to the uncorrelated expectation. The data on three-jet plus photon production in $\bar{p}p$ collisions from the Tevatron CDF [83] and D0 [84] experiments show a significant enhancement compared to the uncorrelated expectation [85], suggesting the presence of substantial correlations in the partonic wave function. Whether these correlations are due to perturbative QCD radiation or the nonperturbative vacuum structure discussed here is a challenging question which requires further study.

E. Exclusive meson production

The nonperturbative short-range correlations in the nucleon's partonic wave function discussed here (see Fig. 18) have potential implications beyond semi-inclusive processes, for example for hard exclusive meson production $\gamma^*N \to M+N$. In π^+ production at $Q^2 \sim \text{few GeV}^2$ and $x \gtrsim 0.1$, a substantial longitudinal cross section should result from the "knockout" of a correlated $q\bar{q}$ pair in the nucleon with appropriate quantum numbers, which then forms a π^+ by way of soft nonperturbative interactions. This mechanism is theoretically subleading compared to the hard scattering mechanism in the limit $Q^2 \to \infty$ (in which the equivalent correlations are generated by perturbative gluon exchange) but may be practically dominant at all realistic values of Q^2 . It may also play a role in exclusive ρ^0 production in the region $W \sim 2-4$ GeV [86], which shows an energy dependence consistent with the t-channel exchange of a $q\bar{q}$ pair with scalar quantum numbers [87]. The theoretical formulation of such knockout processes in exclusive production is the subject of on-going work. Generally, exclusive processes offer many possibilities for probing correlations in the partonic wave function due to QCD vacuum structure, including their x-distribution and quantum numbers.

ACKNOWLEDGMENTS

In this study we greatly benefited from numerous discussions with D. Diakonov, V. Petrov, P. Pobylitsa, and M. Polyakov during earlier joint work on the chiral quark–soliton model. We are grateful also to C. Lorcé for enlightening discussions of the properties of the nucleon light–cone wave function.

M. S. acknowledges the hospitality of Jefferson Lab during the work on this study. This work is supported by the U.S. DOE under Grant No. DE-FGO2-93ER40771. Notice: Authored by Jefferson Science Associates, LLC under U.S. DOE Contract No. DE-AC05-06OR23177. The U.S. Government retains a non-exclusive, paid-up, irrevocable, world-wide license to publish or reproduce this manuscript for U.S. Government purposes.

Appendix A: Parametrization of soliton profile

The profile function P(r) of the classical chiral field, Eq. (2.6) is determined by minimizing the classical energy of the soliton, Eq. (2.8). Numerical minimization was performed with various types of cutoff of the Dirac sea contribution and result in very similar values of the classical energy; see Ref. [31] for a review. For a Pauli–Villars (PV) cutoff, described in detail in Sec. V, the self–consistent profile was determined in Ref. [56]. The result obtained with a dynamical quark mass $M=0.35\,\mathrm{GeV}$, a PV cutoff with $M_{\mathrm{PV}}^2/M^2=2.52$, cf. Eq. (5.52), and the chiral limit $M_\pi=0$, is shown in Fig. 20. The figure shows the mesh points in the variable r at which the profile was determined by numerical minimization; at larger distances the profile effectively exhibits an asymptotic behavior as

$$P(r) \sim -A/r^2$$
. (A1)

With these parameters the classical energy of the soliton, i.e., the nucleon mass in leading order of the $1/N_c$ expansion, Eq. (2.9), was obtained as [56]

$$M_N \approx 3.26 M.$$
 (A2)

The nucleon's isovector axial coupling, obtained by calculating the matrix element of the axial current operator as a sum over quark single–particle levels, is $g_A = 1.03$ with these parameters [88]. In the chiral limit the isovector axial coupling is proportional to the coefficient of the leading r^{-2} asymptotic behavior of the soliton profile at large distances, Eq. (A1),

$$g_A = \frac{8\pi}{3} F_{\pi}^2 A,$$
 (A3)

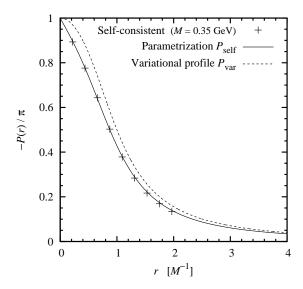


FIG. 20. Soliton profile P(r) as function of the radius r. Points: Self-consistent profile obtained by minimizing the classical energy (PV regularization, $M=0.35\,\mathrm{GeV}, M_\pi=0$) [56]. Solid line: Parametrization P_self , Eqs. (A4)–(A7). Dashed line: Variational profile P_var , Eq. (A8), for $M_\pi=0$.

and can alternatively be determined in this way. The equivalence of the two ways of calculating g_A for the self-consistent profile of Ref. [56] was verified in Ref. [88].

For the purposes of our study we need an analytic parametrization of the soliton profile which has the correct limiting behavior at small and large distances and reproduces the numerical self–consistent profile with reasonable accuracy. It can be constructed in the form

$$P_{\text{self}}(r) = -2 \arctan T(r),$$
 (A4)

where the function T(r) satisfies the following two conditions: (a) $T(r) \propto r^{-1}$ at $r \to 0$, to ensure linear behavior of the profile near the center; (b) $r^2T(r) = A + O(r^{-4})$ for $r \to \infty$, to guarantee the correct r^{-2} asymptotic behavior of the profile and the absence of subleading r^{-4} terms, which was noted in Ref. [30] in the context of a long-distance expansion of the equations of motion. A simple choice which fulfills these conditions is

$$T(r) = \frac{r_0^2}{r^2} \tanh(Br). \tag{A5}$$

The parameter $r_0^2 = A/2$ determines the large-distance behavior of the profile; we fix it by requiring that the parametrization reproduce the "exact" numerical value of $g_A = 1.03$ [88] via Eq. (A3), which gives

$$r_0^2 = 0.87 \, M^{-2}.$$
 (A6)

The parameter B is then fixed by fitting the behavior of the profile at small distances, which results in

$$B = 1.6 M. \tag{A7}$$

The simple parametrization Eqs. (A4)–(A7) provides an excellent fit to the numerical self–consistent profile over all distances (see Fig. 20).

Also shown in the figure is the variational profile of Ref. [30],

$$P_{\text{var}}(r) = -2 \arctan \frac{r_0^2}{r^2},\tag{A8}$$

$$r_0^2 = 1.0 \, M^{-2}, \tag{A9}$$

which was used extensively in earlier calculations of partonic structure [32, 33]. This profile corresponds to the limit $B \to \infty$ of our more general parametrization, Eqs. (A4) and (A5), and has an unphysical quadratic behavior near the center, which, however, is unimportant for the quantities studied here (cf. the discussion in Sec. V C). With the replacement

$$\frac{r_0^2}{r^2} \rightarrow \frac{r_0^2}{r^2} (1 + M_\pi r) \exp(-M_\pi r)$$
 (A10)

Eq. (A8) also allows one to study the effect of a finite pion mass.

Appendix B: Bound-state level wave function

In this appendix we give the explicit form of the bound–state level wave function and its Fourier transform, as used in the calculation of the level contribution to the transverse momentum distributions of quarks and antiquarks in Sec. IV. Most of the relevant expressions were given in Appendix B of Ref. [32], and we include them here for reference only (see also Footnote [55] regarding the convention for gamma matrices).

In the standard representation of the gamma matrices, the bound–state solution of the Dirac equation in the nucleon rest frame, where the classical chiral field is given by Eq. (2.6), can be written in the form

$$\Phi_{\text{lev}}(\boldsymbol{x}) = \frac{1}{\sqrt{4\pi}} \begin{pmatrix} h(r) \\ -i\frac{(\boldsymbol{x}\boldsymbol{\sigma})}{r}j(r) \end{pmatrix} |0\rangle, \quad (B1)$$

where $r \equiv |\mathbf{x}|$ and $|0\rangle$ is the spin–isospin wave function where spin and isospin are coupled to zero total,

$$(\sigma_i + \tau_i)|0\rangle = 0, \qquad \langle 0|0\rangle = 1.$$
 (B2)

The functions h and j are solutions of the radial equation

$$\begin{pmatrix} M\cos P(r) & -\frac{\partial}{\partial r} - \frac{2}{r} - M\sin P(r) \\ \frac{\partial}{\partial r} - M\sin P(r) & -M\cos P(r) \end{pmatrix} \times \begin{pmatrix} h(r) \\ j(r) \end{pmatrix} = E_{\text{lev}} \begin{pmatrix} h(r) \\ j(r) \end{pmatrix}.$$
(B3)

The level wave function Eq.(B1) is normalized to

$$\int d^3x \; \Phi_{\text{lev}}^{\dagger}(\boldsymbol{x})\Phi_{\text{lev}}(\boldsymbol{x}) = 1, \tag{B4}$$

corresponding to

$$\int_{0}^{\infty} dr \, r^{2} \left[h^{2}(r) + j^{2}(r) \right] = 1.$$
 (B5)

The wave function in momentum representation, defined according to Eq.(3.29),

$$\Phi_{\text{lev}}(\boldsymbol{p}) = \int d^3x \ e^{-i\boldsymbol{p}\boldsymbol{x}} \ \Phi_{\text{lev}}(\boldsymbol{x}), \tag{B6}$$

can be written in the form

$$\Phi_{\text{lev}}(\boldsymbol{p}) = \frac{\sqrt{2}\pi}{p} \begin{pmatrix} h(p) \\ -\frac{(\boldsymbol{p}\boldsymbol{\sigma})}{p} j(p) \end{pmatrix} |0\rangle, \quad (B7)$$

where $p \equiv |\mathbf{p}|$. The radial functions in the momentum representation here are given by

$$h(p) = \int_{0}^{\infty} dr \, r^{2} \, h(r) R_{p0}(r),$$

$$j(p) = \int_{0}^{\infty} dr \, r^{2} \, j(r) R_{p1}(r),$$
 (B8)

where R_{pl} are the free radial wave functions of the continuous spectrum, defined as

$$R_{pl}(r) = \sqrt{\frac{2}{\pi}} p \, j_l(pr) = \sqrt{\frac{2}{\pi}} \left(-\frac{1}{p} \frac{d}{dr} \right)^l \frac{\sin pr}{r}, \quad (B9)$$

where $j_l(l=0,1,...)$ denote the spherical Bessel functions, and normalized according to

$$\int_{0}^{\infty} dr \, r^{2} \, R_{pl}(r) R_{p'l}(r) = \delta(p - p'). \tag{B10}$$

The normalization condition for the momentum representation of the bound-state wave function, Eq.(B7), is

$$\int \frac{d^3 p}{(2\pi)^3} \, \Phi_{\text{lev}}(\boldsymbol{p})^{\dagger} \Phi_{\text{lev}}(\boldsymbol{p}) = 1, \quad (B11)$$

corresponding to

$$\int_0^\infty dp \left[h^2(p) + j^2(p) \right] = 1.$$
 (B12)

When computing matrix elements between bound–state level wave functions, one can take advantage of the properties of the spin–isospin singlet state. Specifically,

$$\dots \tau^i |0\rangle = \dots (-\sigma^i)|0\rangle, \tag{B13}$$

$$\langle 0|\tau^i \dots = \langle 0|(-\sigma^i) \dots, \tag{B14}$$

$$\langle 0|\sigma^i|0\rangle = \langle 0|\tau^i|0\rangle = 0.$$
 (B15)

Using these identities one can convert matrix elements of products of σ and τ matrices into equivalent expressions involving only one kind of matrix, which can then be evaluated using standard techniques.

Appendix C: Fourier transform of soliton field

When evaluating the sea quark distribution using the gradient expansion we need explicit expressions of the 3-dimensional Fourier transform of the static classical chiral field in the nucleon rest frame. In coordinate space the field is given by Eq. (2.6) and can be expanded as

$$U_{\rm cl}(\boldsymbol{x}) = \cos P(r) + \frac{i(\boldsymbol{x}\boldsymbol{\tau})}{r}\sin P(r),$$
 (C1)

where $r \equiv |\mathbf{x}|$. The Fourier transform Eq. (5.7) is of the form

$$\tilde{U}_{cl}(\mathbf{k}) \equiv \int d^3x \ e^{-i\mathbf{k}\mathbf{x}} \left[U_{cl}(\mathbf{x}) - 1 \right]
= 4\pi \left[s(k) + \frac{(\mathbf{k}\boldsymbol{\tau})}{k} p(k) \right],$$
(C2)

where $k \equiv |\mathbf{k}|$. The scalar functions s(k) and p(k) are determined as

$$s(k) = \int_0^\infty dr \, r^2 \, j_0(kr) \, \left[\cos P(r) - 1\right],$$
 (C3)

$$p(k) = \int_0^\infty dr \, r^2 \, j_1(kr) \, \sin P(r),$$
 (C4)

where j_0 and j_1 are the spherical Bessel functions, cf. Eq. (B9). The traces in Eq. (5.22) and Eq. (5.71) are then obtained as

$$\operatorname{tr}_{\mathrm{fl}}[\widetilde{U}_{\mathrm{cl}}(\mathbf{k})\widetilde{U}_{\mathrm{cl}}(\mathbf{k})^{\dagger}] = 32\pi^{2}[s^{2}(k) + p^{2}(k)], \quad (C5)$$

$$\operatorname{tr}_{\mathrm{fl}}[\tau^{3}\widetilde{U}_{\mathrm{cl}}(\boldsymbol{k})\widetilde{U}_{\mathrm{cl}}(\boldsymbol{k})^{\dagger}] = 64\pi^{2} s(k) p(k) \frac{k^{3}}{k}.$$
 (C6)

In proving the large– N_c inequalities for the sea quark distributions, cf. Eq. (5.77), it is important to note that the sum and difference of the forms in Eqs. (C5) and (C6) is non–negative. Namely,

$$\operatorname{tr}_{\mathrm{fl}}[(1 \pm \tau^{3})\widetilde{U}_{\mathrm{cl}}(\mathbf{k})\widetilde{U}_{\mathrm{cl}}(\mathbf{k})^{\dagger}] \\
= 32\pi^{2} \left[s^{2}(k) + p^{2}(k) \pm 2s(k) p(k) \frac{k^{3}}{k} \right] \\
\geq 32\pi^{2} \left[|s(k)|^{2} + |p(k)|^{2} - 2|s(k)| |p(k)| \frac{|k^{3}|}{k} \right] \\
\geq 32\pi^{2} (|s(k)| - |p(k)|)^{2},$$
(C7)

where the last inequality follows from $|k^3| \leq k$.

- **0702**, 093 (2007).
- [2] R. K. Ellis, W. Furmanski, R. Petronzio, Nucl. Phys. B207, 1 (1982); B212, 29 (1983).
- [3] J. C. Collins, D. E. Soper, Nucl. Phys. **B194**, 445 (1982).
- [4] B. Badelek, J. Kwiecinski, A. Stasto, Z. Phys. C74, 297 (1997).
- [5] Y. L. Dokshitzer, D. Diakonov and S. I. Troian, Phys. Rept. 58, 269 (1980).
- [6] M. A. Kimber, A. D. Martin, M. G. Ryskin, Eur. Phys.
 J. C12, 655-661 (2000). M. A. Kimber, A. D. Martin,
 M. G. Ryskin, Phys. Rev. D63, 114027 (2001).
- [7] The practical usefulness of such twist—4 operators for nucleon structure studies is limited by the fact that they mix very strongly with twist—2 operators under renormalization, with quadratically divergent coefficient functions, rendering nonperturbative calculations of their matrix elements extremely challenging. For a discussion of this problem, see: G. Martinelli, C. T. Sachrajda, Nucl. Phys. **B478**, 660 (1996).
- [8] J.-W. Qiu, G. F. Sterman, Phys. Rev. Lett. 67, 2264 (1991).
- [9] J. C. Collins and D. E. Soper, Nucl. Phys. B 193, 381 (1981) [Erratum-ibid. B 213, 545 (1983)].
- [10] X. D. Ji, J. P. Ma and F. Yuan, Phys. Rev. D 71, 034005 (2005); Phys. Lett. B 597, 299 (2004).
- [11] J. C. Collins and A. Metz, Phys. Rev. Lett. 93, 252001 (2004).
- [12] J. C. Collins, D. E. Soper and G. Sterman, Nucl. Phys. B 250, 199 (1985).
- [13] I. O. Cherednikov, N. G. Stefanis, Phys. Rev. D77, 094001 (2008); Nucl. Phys. B802, 146 (2008).
 I. O. Cherednikov, A. I. Karanikas, N. G. Stefanis, Nucl. Phys. B840, 379 (2010).
- [14] S. M. Aybat and T. C. Rogers, Phys. Rev. D 83, 114042 (2011).
- [15] A. Bacchetta, D. Boer, M. Diehl et al., JHEP 0808, 023 (2008).
- [16] G. P. Lepage, S. J. Brodsky, Phys. Rev. **D22**, 2157 (1980).
- [17] S. J. Brodsky, H.-C. Pauli and S. S. Pinsky, Phys. Rept. 301, 299 (1998).
- [18] The quantity m_0^2 is conventionally defined as the ratio $m_0^2 = \langle \bar{\psi} \sigma^{\alpha\beta} F_{\alpha\beta} \psi \rangle / \langle \bar{\psi} \psi \rangle$. The dimension–5 operator in the numerator is equivalent to $2\bar{\psi} \nabla^2 \psi$ by virtue of the Heisenberg equations of motion.
- [19] M. Kremer and G. Schierholz, Phys. Lett. B 194, 283 (1987).
- [20] T. W. Chiu and T. H. Hsieh, Nucl. Phys. B 673, 217 (2003) [Nucl. Phys. Proc. Suppl. 129, 492 (2004)].
- [21] T. Doi, N. Ishii, M. Oka and H. Suganuma, Phys. Rev. D 67, 054504 (2003).
- [22] M. C. Chu, J. M. Grandy, S. Huang and J. W. Negele, Phys. Rev. D 49, 6039 (1994).
- [23] J. W. Negele, Nucl. Phys. Proc. Suppl. 73, 92 (1999).
- [24] D. Diakonov, Prog. Part. Nucl. Phys. **51**, 173 (2003);
- [25] E. V. Shuryak, Nucl. Phys. B 203, 93 (1982); Nucl. Phys. B 203, 116 (1982).
- [26] D. Diakonov, V. Yu. Petrov, Nucl. Phys. B272, 457 (1986).
- [27] T. Schafer and E. V. Shuryak, Rev. Mod. Phys. 70, 323 (1998).
- [28] M. V. Polyakov, C. Weiss, Phys. Lett. B387, 841-847 (1996).
- [29] D. Diakonov, M. I. Eides, JETP Lett. 38, 433-436 (1983).

- [30] D. Diakonov, V. Yu. Petrov and P. V. Pobylitsa, Nucl. Phys. B 306, 809 (1988).
- [31] For a review, see: C. V. Christov, A. Blotz, H.-C. Kim et al., Prog. Part. Nucl. Phys. 37, 91 (1996).
- [32] D. Diakonov, V. Petrov, P. Pobylitsa, M. V. Polyakov and C. Weiss, Nucl. Phys. B 480 (1996) 341.
- [33] D. Diakonov, V. Petrov, P. Pobylitsa, M. Polyakov and C. Weiss, Phys. Rev. D 56, 4069 (1997).
- [34] M. Gluck, P. Jimenez-Delgado and E. Reya, Eur. Phys. J. C 53, 355 (2008).
- [35] P. Amaudruz et al. [New Muon Collaboration], Phys. Rev. Lett. 66, 2712 (1991). M. Arneodo et al. [New Muon Collaboration], Phys. Rev. D 50, 1 (1994).
- [36] A. Baldit et al. [NA51 Collaboration], Phys. Lett. B 332, 244 (1994). E. A. Hawker et al. [FNAL E866/NuSea Collaboration], Phys. Rev. Lett. 80, 3715 (1998). R. S. Towell et al. [FNAL E866/NuSea Collaboration], Phys. Rev. D 64, 052002 (2001).
- [37] D. de Florian, R. Sassot, M. Stratmann, W. Vogelsang, Phys. Rev. Lett. 101, 072001 (2008); Phys. Rev. D80, 034030 (2009).
- [38] B. Dressler, K. Goeke, M. V. Polyakov, P. Schweitzer, M. Strikman, C. Weiss, Eur. Phys. J. C18, 719 (2001).
- [39] First results were recently reported in: M. M. Aggarwal et al. [STAR Collaboration], Phys. Rev. Lett. 106, 062002 (2011). A. Adare et al. [PHENIX Collaboration], Phys. Rev. Lett. 106, 062001 (2011).
- [40] M. Wakamatsu, Phys. Rev. D79, 094028 (2009).
- [41] V. Yu. Petrov and M. V. Polyakov, hep-ph/0307077.
- [42] D. Diakonov and V. Petrov, Annalen Phys. 13, 637 (2004).
- [43] C. Lorce, Phys. Rev. D 78, 034001 (2008).
- [44] L. L. Frankfurt and M. I. Strikman, Phys. Rept. 76, 215 (1981).
- [45] L. Frankfurt, M. Sargsian and M. Strikman, Int. J. Mod. Phys. A 23, 2991 (2008).
- [46] J. Arrington, D. W. Higinbotham, G. Rosner and M. Sargsian, Prog. Part. Nucl. Phys. 67, 898 (2012).
- [47] R. Jakob, P. J. Mulders, J. Rodrigues, Nucl. Phys. A626, 937 (1997). L. P. Gamberg, G. R. Goldstein, K. A. Oganessyan, Phys. Rev. D67, 071504 (2003).
 L. P. Gamberg, G. R. Goldstein, M. Schlegel, Phys. Rev. D77, 094016 (2008). A. Bacchetta, F. Conti, M. Radici, Phys. Rev. D78, 074010 (2008). J. She, J. Zhu and B.-Q. Ma, Phys. Rev. D 79, 054008 (2009).
- [48] H. Avakian, A. V. Efremov, P. Schweitzer and F. Yuan, Phys. Rev. D 78, 114024 (2008).
- [49] H. Avakian, A. V. Efremov, P. Schweitzer and F. Yuan, Phys. Rev. D81, 074035 (2010).
- [50] B. Pasquini, S. Cazzaniga, S. Boffi, Phys. Rev. D78, 034025 (2008). S. Boffi, A. V. Efremov, B. Pasquini and P. Schweitzer, Phys. Rev. D 79, 094012 (2009).
 B. Pasquini, F. Yuan, Phys. Rev. D81, 114013 (2010).
 B. Pasquini and P. Schweitzer, Phys. Rev. D 83, 114044 (2011) C. Lorce, B. Pasquini and M. Vanderhaeghen, JHEP 1105, 041 (2011).
- [51] A. V. Efremov, P. Schweitzer, O. V. Teryaev, P. Zavada, Phys. Rev. **D80**, 014021 (2009); Phys. Rev. D **83**, 054025 (2011).
- [52] This approach is fundamentally different from models in which a "pion cloud" is generated by leading—order perturbation theory in the pion—quark or pion—nucleon coupling without any parametric basis. The only instance where a perturbative treatment of the pion coupling in

- such models is justified is in a space–time formulation at large distances (impact parameter representation), where the pions have wavelenghts $\sim 1/M_{\pi}$ and the approach becomes equivalent to chiral perturbation theory; see: M. Strikman, C. Weiss, Phys. Rev. **D80**, 114029 (2009).
- [53] D. I. Diakonov and V. Yu. Petrov, Report LENINGRAD-86-1153, published (in Russian) in: Hadron Matter under Extreme Conditions, Eds. G. M. Zinovev and V. P. Shelest, Naukova Dumka, Kiev (1986), p. 192.
- [54] D. Diakonov, M. V. Polyakov and C. Weiss, Nucl. Phys. B 461, 539 (1996).
- [55] The sign of the profile function depends on the convention for the Dirac matrix γ_5 . In the Landau–Lifshitz convention used in Ref. [30], $\gamma_5 \equiv -i\gamma^0\gamma^1\gamma^2\gamma^3$, one has $P(0) = +\pi$ for a soliton with baryon number +1. Following Refs. [32, 33] and the recent literature on the chiral quark–soliton model we use here the Bjorken–Drell convention, where γ_5 is defined with opposite sign from the Landau–Lifshitz convention and $P(0) = -\pi$.
- [56] C. Weiss, K. Goeke, hep-ph/9712447.
- [57] S. Kahana, G. Ripka, Nucl. Phys. A429, 462 (1984).
- [58] A. Bacchetta, M. Boglione, A. Henneman and P. J. Mulders, Phys. Rev. Lett. 85, 712 (2000).
- [59] P. V. Pobylitsa and M. V. Polyakov, Phys. Rev. D 62, 097502 (2000).
- [60] P. Schweitzer, T. Teckentrup, A. Metz, Phys. Rev. D81, 094019 (2010).
- [61] A smaller value of the polarized $\langle p_T^2 \rangle$ compared to the unpolarized one is also obtained in phenomenological models based on Gaussian distributions. For a Gaussian distribution $\langle p_T^2 \rangle$ is proportional to the width, and a larger width for the polarized distribution would lead to a violation of positivity at large p_T . While certainly not rigorous, this argument makes plausible why for near-Gaussian shapes the polarized $\langle p_T^2 \rangle$ should be smaller than the unpolarized one.
- [62] J. Schwinger, Phys. Rev. 82 (1951) 664.
- [63] This property was used in a different context in Ref. [33], where the gradient expansion was employed to obtain analytic expressions for the leading asymptotic behavior of the p_T-integrated parton densities as functions of the UV cutoff of the model.
- [64] The behavior of the momentum distribution of the classical chiral field in the limit $y \to 0$ depends on the pion mass. For $M_{\pi} = 0$ the function $f_{\rm cl}(y)/y^2$ diverges in the limit $y \to 0$, for $M_{\pi} > 0$ it converges. This detail is not important for our study of sea quark distributions in the bulk-dominated region $x \sim 0.1$, and we can safely set the pion mass to zero in our calculations [the soliton profile Eq. (A4) corresponds to $M_{\pi} = 0$]. However, the pion mass becomes important when studying the growth of the transverse spatial size of the chiral component to the nucleon's sea quark and gluon distributions at small x; see: M. Strikman, C. Weiss, Phys. Rev. **D69**, 054012 (2004), and the article cited in Ref. [52].
- [65] B. Dressler, K. Goeke, M. V. Polyakov, C. Weiss, Eur. Phys. J. C14, 147 (2000).

- [66] P. V. Pobylitsa, M. V. Polyakov, K. Goeke, T. Watabe and C. Weiss, Phys. Rev. D 59, 034024 (1999).
- [67] P. V. Pobylitsa and M. V. Polyakov, Phys. Lett. B 389, 350 (1996).
- [68] P. Schweitzer, D. Urbano, M. V. Polyakov, C. Weiss, P. V. Pobylitsa and K. Goeke, Phys. Rev. D 64, 034013 (2001).
- [69] V. N. Gribov, arXiv:hep-ph/0006158.
- [70] B. Blok, Yu. Dokshitzer, L. Frankfurt and M. Strikman, Phys. Rev. D 83, 071501 (2011).
- [71] M. Diehl, D. Ostermeier and A. Schafer, JHEP 1203, 089 (2012); JHEP 1203, 089 (2012).
- [72] A similar picture of the role of QCD instantons in partonic structure was discussed in: A. E. Dorokhov and N. I. Kochelev, Phys. Lett. B 304, 167 (1993).
- [73] J. Balla, M. V. Polyakov and C. Weiss, Nucl. Phys. B 510, 327 (1998).
- [74] B. Dressler, M. Maul and C. Weiss, Nucl. Phys. B 578, 293 (2000).
- [75] C. Weiss, J. Phys. G 29, 1981 (2003).
- [76] F. D. Aaron *et al.* [H1 Collaboration], JHEP **1005**, 032 (2010).
 S. Chekanov *et al.* [ZEUS Collaboration], PMC Phys. **A1**, 6 (2007).
- [77] L. L. Frankfurt, M. I. Strikman, L. Mankiewicz, A. Schafer, E. Rondio, A. Sandacz, V. Papavassiliou, Phys. Lett. B230, 141 (1989).
- [78] E. Christova, E. Leader, Nucl. Phys. B607, 369 (2001).
- [79] How the nonperturbative $q\bar{q}$ correlations in the nucleon wave function manifest themselves in the hadronic final state may be affected by the possibility that the nonperturbative gluon field inducing the correlation could materialize in the final state. As discussed above, fits to DIS data show that at the chiral symmetry–breaking scale about $\sim 30\%$ of the nucleon's momentum is carried by gluons. This suggests that at least part of the nonperturbative gluon fields in the fast–moving nucleon project on physical gluon states that can carry longitudinal momentum away into the final state.
- [80] For information about the CERN COMPASS experiment, see http://www.compass.cern.ch/
- [81] A. Accardi, V. Guzey, A. Prokudin and C. Weiss, Eur. Phys. J. A 48, 92 (2012).
- [82] For information about the Jefferson Lab 12 GeV Upgrade, see https://www.jlab.org/
- [83] F. Abe et al. [CDF Collaboration], Phys. Rev. Lett. 79, 584 (1997); Phys. Rev. D 56, 3811 (1997).
- [84] V. M. Abazov et al. [D0 Collaboration], Phys. Rev. D 81, 052012 (2010).
- [85] L. Frankfurt, M. Strikman and C. Weiss, Phys. Rev. D 69, 114010 (2004). See also: L. Frankfurt, M. Strikman, D. Treleani and C. Weiss, Phys. Rev. Lett. 101, 202003 (2008).
- [86] S. A. Morrow et al. [CLAS Collaboration], Eur. Phys. J. A 39, 5 (2009).
- [87] M. Guidal and S. Morrow, arXiv:0711.3743 [hep-ph].
- [88] P. Schweitzer, Doctoral dissertation, Bochum University, unpublished (2001).